Compositional Effects on Local Structure in Glassy Binary Lennard-Jones Nanoparticles

A Thesis Submitted to the
College of Graduate and Postdoctoral Studies
in Partial Fulfillment of the Requirements
for the degree of Master of Science
in the Department of Department of Chemistry
University of Saskatchewan
Saskatoon

By
Zhongquan Chen

Permission to Use

In presenting this thesis in partial fulfilment of the requirements for a Postgraduate degree from the University of Saskatchewan, I agree that the Libraries of this University may make it freely available for inspection. I further agree that permission for copying of this thesis in any manner, in whole or in part, for scholarly purposes may be granted by the professor or professors who supervised my thesis work or, in their absence, by the Head of the Department or the Dean of the College in which my thesis work was done. It is understood that any copying or publication or use of this thesis or parts thereof for financial gain shall not be allowed without my written permission. It is also understood that due recognition shall be given to me and to the University of Saskatchewan in any scholarly use which may be made of any material in my thesis.

Requests for permission to copy or to make other use of material in this thesis in whole or part should be addressed to:

Head of the Department of Chemistry
155 Thorvaldson Building
110 Science Place
University of Saskatchewan
Saskatoon, Saskatchewan
Canada
S7N 5C9

Abstract

When a liquid is cooled quickly so that it avoids crystallization, the motion of the atoms or molecules slow until they eventually become kinetically trapped in an amorphous solid state at the glass transition temperature. There is no thermodynamic signature associated with the glass transition and the glass structure remains similar to that of the supercooled liquid. This raises questions about the fundamental nature of the glass phenomena. One approach to understanding the glass transition suggests that the formation of locally favoured structures, consisting of low energy clusters of atoms that are unable to tile space, compete with the formation of crystal nuclei and prevent the formation of the crystal.

The work described in this thesis uses computer simulation to explore the role of locally favoured structures in the glass forming ability of binary Lennard-Jones clusters formed from large A type atoms and small B type atoms with Kobb-Andersen interaction parameters. The phase diagram for the clusters with a size $N = 600$ is mapped out as a function of composition to identify the glass forming region over the range of B atom mole fractions $x_B = 0 - 0.5$. Caloric curves, measuring the potential energy per atom as a function of temperature, exhibit large discontinuities suggesting freezing for compositions $x_B < 0.1$ and $x_B > 0.35$. At intermediate compositions, the potential energy varies continuously, but rapidly changes slope at a low temperature, which is indicative of a glass transition. The glass transition temperature of these clusters increases with increasing x_B. The amorphous nature of the clusters in the $x_B = 0.1 - 0.3$ composition range is confirmed on the basis of measurements of the radial distribution function. The radial distribution function for the $x_B = 0.4$ shows that the cluster freezes to a CsCl type crystal. Furthermore, measurements of the density profile and composition distribution as a function of radius from the centre of mass of the clusters show that the B atoms exhibit a significant enrichment at the core for all compositions which may influence the overall phase behaviour of the system relative to the bulk.

The local structure around an atom was studied using the local, average and disorder orientational bond order parameters which are based on the Steinhardt bond order parameters. The order parameters decrease as a function of decreasing temperature in the liquid phase, then increase at the freezing temperature for those compositions that crystallize. In the glass phase, the order parameters plateau at the glass transition temperature. The exception is the $x_B = 0.1$ composition. These clusters exhibit a small amount of ordering at the glass transition. Additional analysis shows that this is caused by the partial ordering of the A atoms at the cluster surface, while the core remains amorphous. The disorder parameter effectively captures the same phenomena but in reverse and also shows that, at low temperatures, the $x_B = 0.3$ clusters are the most disordered.

Finally, a Voronoi analysis, quantified in terms of the Voronoi index, is used to describe the geometric nature of the cage formed by neighbouring atoms around the B type atoms in the core of the glass forming clusters. The number of different types of polyhedra increases with increasing x_B, but the ten most abundant polyhedra remain the same and consist of 9-11 sided structures. It is notable that icosahedral structures are

not observed. Instead, the $(0, 2, 8, 0)$ polyhedron, which is consistent with a bicapped antiprism, is the most abundant structure for all compositions and exhibits the largest increase as a function of temperature, essentially doubling in concentration as the liquid approaches the glass transition temperature. However, the overall fraction of B atoms involved in $(0, 2, 8, 0)$ polyhedra in the glass decreases from 0.35 to 0.15 as x_B increases from 0.1 to 0.3, The probability distribution for all polyhedra also becomes more uniform. This is consistent with the clusters becoming more disordered as measured by the orientational bond order parameters.

To conclude, this thesis maps out the glass forming compositions for binary Lennard-Jones clusters and shows that composition has a significant effect on the types and distribution of local structure observed in the glass forming systems.

Acknowledgements

I would like to thank my thesis supervisor Dr R.K.Bowles of the Department of Chemistry at University of Saskatchewan. Dr. Bowles is very knowledgeable in Computation Chemistry, and he consistently gave me guidance whenever I have difficulty in my research. He is so generous in his time in helping students that he always made himself available at his office. I would also like to thank Weikai who was a researcher involved in the molecular simulation for this research project. I appreciate that Weikai gave me guidance in my academic life and he always gave me good ideas in computational methods.

Finally, I must express my very profound gratitude to my parents for providing me with unfailing support and continuous encouragement throughout my years of study and through the process of researching and writing this thesis. This accomplishment would not have been possible without them. Thank you.

This dissertation is dedicated to my supervisor Dr. Bowles, whose passion for teaching and supervising students set a new standard for anyone involved in education, training, development and other endeavor in which one human supports the growth of another. He is very knowledgeable in the courses he teaches so that he can explain a very abstract concept in an easy-to-understand way. Also, he has a good understanding of the problems students have and always patiently guide them to the solution.

I also dedicate this research work and give special thanks to my parents and sisters . You are always there supporting my master program study. And Both of you have been my best cheerleaders. Without the support from all of you, my study could not have been possible.

And I also want to thank Weikai who have supported me to develop the research process. And my cousin Weiguo who gave me guidance in my life. I will always appreciate all you have done for helping me.

Contents

Permission to Use i

Abstract ii

Acknowledgements iv

Contents vi

List of Figures viii

List of Abbreviations xi

1 Introduction 1
- 1.1 Overview . . . 1
- 1.2 Phenomenology of the glass transition . . . 2
  - 1.2.1 Supercooled liquids: Nucleation and Slow Dynamics . . . 2
  - 1.2.2 Kinetic Aspects of Glass . . . 3
  - 1.2.3 Thermodynamic Aspects of Glass . . . 5
- 1.3 Theories of glass transition . . . 6
  - 1.3.1 Adam-Gibbs Theory and Cooperatively Rearranging Region . . . 6
  - 1.3.2 Potential Energy Landscapes . . . 7
  - 1.3.3 Geometric Frustration . . . 9
  - 1.3.4 Dynamic Facilitation . . . 9
- 1.4 Molecular Dynamic Simulation . . . 11
  - 1.4.1 Overview . . . 11
  - 1.4.2 Statistical Mechanics . . . 12
  - 1.4.3 Molecular Dynamics Algorithm . . . 13
  - 1.4.4 Verlet Algorithm . . . 14
- 1.5 Structural Analysis . . . 15
  - 1.5.1 Radial Distribution Function . . . 15
  - 1.5.2 Common Neighbor Analysis . . . 17
  - 1.5.3 Bond Order Parameters . . . 18
  - 1.5.4 Average Bond Order Paramters . . . 20
  - 1.5.5 Disorder Parameter . . . 20
  - 1.5.6 Voronoi Analysis . . . 21
- 1.6 Structure in Lennard Jones Nano Particles . . . 22
- 1.7 Research Objectives . . . 24

2 Local Structure in Binary Lennard Jones Nanoparticles 25
- 2.1 Introduction . . . 25
- 2.2 Model and Method . . . 25
  - 2.2.1 Simulation Model . . . 25
  - 2.2.2 Structural Analysis Methods . . . 26
- 2.3 Results . . . 27
  - 2.3.1 Thermodynamics of Nanoclusters . . . 27
  - 2.3.2 Radial Distribution Function . . . 29
  - 2.3.3 Density Profile . . . 30
  - 2.3.4 Structural Analysis of Nanoclusters Using Bond Orientational Order/Disorder Parameters . . . 32
  - 2.3.5 Temperature Dependence of Orientational Bond Order/Disorder Parameters . . . 38

2.3.6 $qA(i)_4$-$qA(i)_6$ Plots for Lenard Jones Nanoclusters 46
2.3.7 Voronoi Diagram 50
2.4 Discussion 57
2.4.1 Summary of hypothesis 57
2.4.2 Phase diagram 57
2.4.3 Change in local structure with varous composition 59
2.4.4 Future work 61

References **63**

Appendix A Figures **69**

List of Figures

1.1 Free energy diagram for nucleation. The red line shows the change of Gibbs free energy ΔG as a function of radius r. The blue line shows the interfacial energy as a function of radius, the green line shows the volume energy as a function of radius. 3
1.2 Temperature as a function of nucleation time. The dash line indicates a cooling schedule to form a glass. Reproduced under permission from reference [17] 4
1.3 Arrhenius representation of liquid viscosities showing Angells strong fragile pattern. Strong liquids exhibit approximate linearity (Arrhenius behavior). Fragile liquids exhibit super-Arrhenius behavior, their effective activation energy increasing as temperature decreases. Reproduced under permission from reference [11] 5
1.4 Temperature dependence of the liquids volume V or enthalpy H at constant pressure. T_m is the melting temperature. A slow cooling rate produces a glass transition at T_{ga}; a faster cooling rate leads to a glass transition at T_{gb}. Reproduced under permission from reference [11] 6
1.5 Classification of particle configurations according to multidimensional potential energy minima that can be reached by steepest-descent paths called quenches. 8
1.6 Left: The plateau emergence observed near T_g from incoherent intermediate scattering function $F_s(q,t)$. Right: mean square displacement $<r^2(t)>$. Reproduced under permission from reference [12] 10
1.7 The pictures are renderings of the mobility field $\kappa(\vec{r},t;\Delta t)$ for typical equilibrium trajectories of 10^4 particles. The displacement time,t, is given in reference to the $1/e$ time for the Van Hove self-correlation functions at the corresponding temperatures. The rendering shades each particle according to the size of the particles displacement from its initial position. Reproduced under permision from reference [70] 11
1.8 Radial distribution function for Lenard-Jones liquid. 16
1.9 Radial distribution function for FCC (blue line) and FCC-HCP mixture (red line). Reproduced under permission from [86] 17
1.10 A cluster of atoms with bonds connected when the distance between the two atoms are less than r_{cut}. CNA index of the red atom pair is (6,4,3) 18
1.11 Atomic arrangement for FCC, ICO, HCP and BCC (CsCl for binary components) structures. 18
1.12 (a): Two-dimensional Voronoi tessellation construction. (b): A Voronoi Cluster of tetrahedron in three dimension. Red lines provide a guide to the eye. 21
1.13 A comparison of (a) two-dimensional graphs of the ordinary Voronoi tessellation and (b) the radial plane construction. In case of radial plane construction, the bisetting method takes the radius into account. The local structure, i.e., the number of faces for the Voronoi cell also depends on the atom size. Reproduced under permission from[96]. 22
1.14 Atomic arrangement for a bicapped squared antiprism Voronoi cell. 23

2.1 Potential energy as a function of temperature for a $x_B = 0.3$ nanocluster system , with cooling rate marked. The intersection of two linear fittings shows the calculation of T_g. 27
2.2 Cluster freezing and glass transition potential energy per particle as a function of temperature. The numbers on each line indicate the B-type particle fraction. In all data, error bars indicate standard deviation of the data for ten independent runs. 28
2.3 Inherent Structure Energy per atom (EIS) for different B-type fraction as a function of temperature. EIS decreases with increase of B-type fraction, as the system sample lower energy landscape. 29
2.4 Radial Distribution for $x_B = 0.3$ nanocluster. Figure(a) shows the $g(r)$ of liquid state at high temperature. Figure(b) shows the $g(r)$ of glassy state at low temperature. 31
2.5 Radial Distribution for $x_B = 0.4$ nanocluster. Figure(a) shows the $g(r)$ of liquid state at high temperature. Figure(b) shows the $g(r)$ of crystal state at low temperature. 31
2.6 (a), The density and (b), the fraction of B atoms as a function of radius from the center of the $x_B = 0.1$ nanocluster. 33

2.7 (a), The density and (b), the fraction of B atoms as a function of radius from the center of the $x_B = 0.2$ nanocluster. . . . 33
2.8 (a), The density and (b), the fraction of B atoms as a function of radius from the center of the $x_B = 0.3$ nanocluster. . . . 34
2.9 (a), The density and (b), the fraction of B atoms as a function of radius from the center of the $x_B = 0.4$ nanocluster. . . . 34
2.10 Distribution of local order parameters with different symmetry index l, for pure A nanocluster at high and low temperature. . . . 35
2.11 Distribution of average local order parameters with different symmetry index l, for pure A nanocluster at high and low temperature. . . . 35
2.12 Distribution of disorder parameters with different symmetry index l, for pure A nanocluster at high and low temperature. . . . 36
2.13 Distribution of disorder parameters with different symmetry index l, for $x_B = 0.1$ nanocluster at high and low temperature. . . . 37
2.14 The number density of atoms with $D(i)_6 < 1.0$, as a function of radius from the center of the $x_B = 0.1$ nanocluster. Red line is a guide to the eye. B composition and temperature are shown in the graph. . . . 38
2.15 Distribution of average local order parameters with different symmetry index l, for $x_B = 0.2$ nanocluster at high and low temperature. . . . 39
2.16 Distribution of average local order parameters with different symmetry index l, for $x_B = 0.4$ nanocluster at high and low temperature. . . . 39
2.17 Disorder parameters $< D >_l$ with $l = 3, 4, 6, 8$ for $x_B = 0, 0.1, 0.2, 0.3, 0.33, 0.35$ and 0.4 nanoclusters. Every point represents average value from 2000 configurations collected in the equilibrium process. The error bar shows the standard deviation of these 2000 configurations. 40
2.18 Average order parameter with $l = 6$ at different temperature. Every point represents the average value from 2000 configurations collected in the equilibrium process. The error bar shows the standard deviation of these 2000 configurations. . . . 42
2.19 Average order parameter with $l = 4$ at different temperature. Every point represents the average value from 2000 configurations collected in the equilibrium process. The error bar shows the standard deviation of these 2000 configurations. . . . 42
2.20 Average order parameter with $l = 8$ at different temperature. Every point represents the average value from 2000 configurations collected in the equilibrium process. The error bar shows the standard deviation of these 2000 configurations. . . . 43
2.21 Local order parameter with $l = 6$ at different temperature. Every point represents the average value from 2000 configurations collected in the equilibrium process. The error bar shows the standard deviation of these 2000 configurations. . . . 43
2.22 Disorder parameter with $l = 6$ at different temperature. Every point represents the average value from 2000 configurations collected in the equilibrium process. The error bar shows the standard deviation of these 2000 configurations. . . . 45
2.23 Global order parameter with $l = 6$ at different temperature. Every point represents the average value from 2000 configurations collected in the equilibrium process. The error bar shows the standard deviation of these 2000 configurations. Insert shows an expanded view of the low Q_6 region. . . . 45
2.24 $qA(i)_4$-$qA(i)_6$ distribution for one pure A nanocluster at $T = 0.20$. All 600 atoms are colored and categorized into 3 major types based on the structure identified by CNA method. . . . 47
2.25 $qA(i)_6$-$qA(i)_8$ distribution for one pure A nanocluster at $T = 0.20$. All 600 atoms are colored and categorized into 3 major types based on the structure identified by CNA method. . . . 47
2.26 $qA(i)_4$-$qA(i)_6$ distribution for 10 pure A nanoclusters at $T = 0.20$. Different colors indicate atoms' local structural environment identified by CNA method. Only 3 types of structures are shown, while other atom data are not plotted. . . . 48
2.27 $qA(i)_4$-$qA(i)_6$ distribution for $x_B = 0.1$ nanocluster at (a)$T = 0.20$ and (b)$T = 0.35$. Red points represents B atoms and black point represents A atoms. . . . 49
2.28 $qA(i)_4$-$qA(i)_6$ distribution for $x_B = 0.2$ nanocluster at $T = 0.20$. Red points represents B atoms and black point represents A atoms. . . . 50

2.29 $qA(i)_4$-$qA(i)_6$ distribution for $x_B = 0.3$ nanocluster at (a)$T = 0.20$ and (b)$T = 0.55$. Red points represents B atoms and black point represents A atoms. Atoms with q4 above 1.0 are visualized in the square box. 51
2.30 $qA(i)_4$-$qA(i)_6$ distribution for $x_B = 0.4$ nanocluster at (a)$T = 0.35$ and (b)$T = 0.55$. Red points represents B atoms and black point represents A atoms. 51
2.31 The number density of atoms with $qA(i)_4 > 0.1$, as a function of radius from the center of the $XB = 0.2$ nanocluster. Red line is a guide to the eye. B composition and temperature are shown in graph. 52
2.32 10 most frequent Voronoi cell for $x_B = 0.1$ nanocluster system at temperatures above and below glass transition temperature. 53
2.33 10 most frequent Voronoi cell for $x_B = 0.2$ nanocluster system at temperatures above and below glass transition temperature. 53
2.34 10 most frequent Voronoi cell for $x_B = 0.3$ nanocluster system at temperatures above and below glass transition temperature. 54
2.35 Temperature dependence of 4 predonimant Voronoi Cell in inherent structure of $x_B = 0.1$ nanocluster. 55
2.36 Temperature dependence of 4 predonimant Voronoi Cell in inherent structure of $x_B = 0.2$ nanocluster. 55
2.37 Temperature dependence of 4 predonimant Voronoi Cell in inherent structure of $x_B = 0.3$ nanocluster. 56
2.38 Phase diagram. Phase Transition temperature as a function of B-type particle fraction x_B. Glass transition occurs in system with $x_B = 0.1, 0.2, 0.3$. Crystallization is observed when $x_B > 0.3$ and $x_B < 0.1$. 58

A.1 Radial Distribution for pure A nanocluster. Figure(a) shows the $g(r)$ of liquid state at high temperature. Figure(b) shows the $g(r)$ of crystal state at low temperature. 70
A.2 Radial Distribution for $x_B = 0.1$ nanocluster. Figure(a) shows the $g(r)$ of liquid state at high temperature. Figure(b) shows the $g(r)$ of glassy state at low temperature. 70
A.3 Radial Distribution for $x_B = 0.2$ nanocluster. Figure(a) shows the $g(r)$ of liquid state at high temperature. Figure(b) shows the $g(r)$ of glassy state at low temperature. 71
A.4 Distribution of average local order parameters with different symmetry index l, for $x_B = 0.1$ nanocluster at high and low temperature. 71
A.5 Distribution of local order parameters with different symmetry index l, for $x_B = 0.1$ nanocluster at high and low temperature. 72
A.6 Distribution of local order parameters with different symmetry index l, for $x_B = 0.2$ nanocluster at high and low temperature. 72
A.7 Distribution of disorder parameters with different symmetry index l, for $x_B = 0.2$ nanocluster at high and low temperature. 73
A.8 Distribution of average local order parameters with different symmetry index l, for $x_B = 0.3$ nanocluster at high and low temperature. 73
A.9 Distribution of local order parameters with different symmetry index l, for $x_B = 0.3$ nanocluster at high and low temperature. 74
A.10 Distribution of disorder parameters with different symmetry index l, for $x_B = 0.3$ nanocluster at high and low temperature. 74
A.11 Distribution of local order parameters with different symmetry index l, for $x_B = 0.4$ nanocluster at high and low temperature. 75
A.12 Distribution of average disorder parameters with different symmetry index l, for $x_B = 0.4$ nanocluster at high and low temperature. 75
A.13 $D(i)_4$-$D(i)_6$ distribution for 10 pure A nanoclusters at $T = 0.20$. 76
A.14 $D(i)_4$-$D(i)_6$ distribution for $x_B = 0.1$ nanocluster at $T = 0.20$. 76
A.15 $D(i)_4$-$D(i)_6$ distribution for $x_B = 0.2$ nanocluster at $T = 0.20$. 77
A.16 $D(i)_4$-$D(i)_6$ distribution for $x_B = 0.3$ nanocluster at $T = 0.20$. 77

List of Abbreviations

CRR	cooperatively rearranging region
PEL	Potential Energy Landscape
MSD	mean square displacement
MD	Molecular Dynamics
LTE	Local Truncation Error
LJ	Lennard-Jones
KA	Kobb-Andersen
CNA	Common Neighbor Analysis
FCC	Face Center Cubic
BCC	Body Center Cubic
HCP	Hexagonal Close Pack
ICO	Iconsahedron
EIS	Inherent Structure Energy
VVA	Velocity Verlet Algorithm

Chapter 1

Introduction

1.1 Overview

Glasses are amorphous solid materials that lack the long range order of crystalline materials. They are usually formed through the rapid cooling of the liquid melt that causes the viscosity of the liquid to increase rapidly until the system becomes a solid at the glass transition. The glass transition occurs without any clear thermodynamic signature and the resulting material retains the structural properties of the liquid.

Glasses appear in a wide range of natural and engineered materials[1]. Glass transition affects the protein conformations and its dynamical properties upon folding[2, 3]. Widely-used art framework window glass has been known for centuries and is the best example of a glass, prepared by cooling of sand-lime-soda chemicals[4]. Metallic glasses are a more modern development that have demonstrated great stability and mechanical strength, due to the addition of third, fourth elements to the alloy, that has lead to them being used as new materials in high stress applications, such as golf clubs[5, 6].

Despite our extensive ability to manipulate the properties of glass materials, a fundamental understanding of why glasses form still remains elusive[7, 8]. The goal of this project is to study nanoscale clusters, with an emphasis to understanding how the composition of a material can influence the local structure around the constituent atoms and affect the glass forming properties. To achieve this, the research work will focus on studying local structure in a binary mixture nanoparticle as a function of the composition and identify the glass forming region of the phase diagram.

The remainder of the introductory chapter is organized as follows. Section 1.2 describes the phenomenology of the glass transition including kinetic and thermodynamic aspects and Section 1.3 outlines the main theoretical approaches used to understand glasses. Section 1.4 provides an overview of molecular dynamics simulation, the main tool used in this thesis before Section 1.5, which describes the methods of structural analysis used to study glassy materials and nanoparticles. Section 1.6 provides a review of structural studies in Lennard Jones particles before the main goals and scope of the thesis is outlined in Section 1.7.

1.2 Phenomenology of the glass transition

1.2.1 Supercooled liquids: Nucleation and Slow Dynamics

When a liquid is cooled below its equilibrium freezing temperature, it becomes metastable with respect to the crystal phase and should crystallize. Nucleation requires the reorganization of the liquid structure to form a cluster of the crystal phase and involves the crossing of a free energy barrier[9]. As such, it is a kinetic process and the nucleation time ranges over many orders of magnitude depending on variables such as the temperature and the degree of metastability[10]. If the cooling rate is fast enough then crystallization can be avoided and molecules in the vicious liquid rearrange so slowly that the system cannot sample the configurations of the crystalline state. Upon further cooling it eventually forms a glass[11, 12].

For an idealized model, just consider the homogeneous case where a solid nucleus spontaneously appear within the undercooled phase. Above the melting temperature, T_m, liquid phase has the lowest free enery, so the liquid is stable. Once $T \leq T_m$, the crystal becomes thermodynamically favored, and the system will prefer to crystallize via nucleation, aided by thermal fluctuations. The formation of a solid nucleus leads to a Gibbs free energy change,

$$\Delta G = G_S - G_L = V(G_S^0 - G_L^0) + A_{surface}\gamma,$$

where $G_S^0 - G_L^0$ is the difference between free energies per unit volume of solid and liquid. Assuming the cluster is a sphere of radius r, $V = \frac{4\pi r^3}{3}$ is the volume of the solid phase. $A_{surface} = 4\pi r^2$ is the surface area, and γ is solid/liquid interfacial free energy[13]. The total change of the Gibbs free energy in nucleation can be expressed as,

$$\Delta G(r) = \frac{4\pi r^3}{3}(G_S^0 - G_L^0) + 4\pi\gamma r^2. \tag{1.1}$$

The nucleation process can be interpreted as a competition between the thermodynamic driving force and interfacial resistance, induced by thermal fluctuation[14]. This competitive process results in a $\Delta G - r$ curve, shown as the red line in Fig. 1.1. The maximum of the red curve shows that there is an energy barrier that needs to be overcome before a system can change phase. Maximizing Eq. 1.1 gives:

$$r_c = -2\gamma/(G_S^0 - G_L^0), \tag{1.2}$$

$$\Delta G(r_c) = \frac{16\pi\gamma^3}{3(G_S^0 - G_L^0)^2}. \tag{1.3}$$

$\Delta G(r_c)$ is the energy barrier to be overcome in order to nucleate. When r is small, the interface term dominates and the embryo of the new phase tends to shrink. When r is larger than the critical size r_c, the

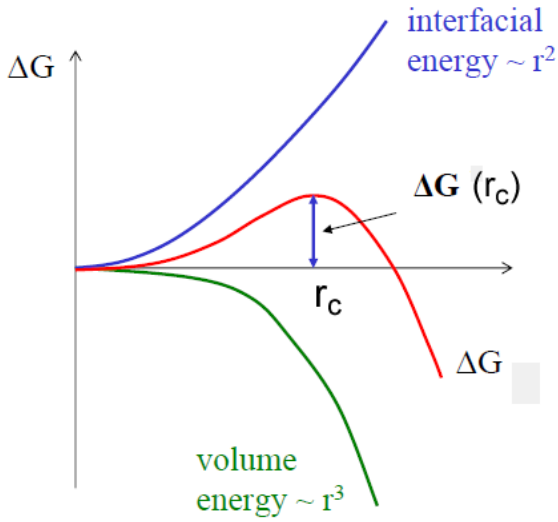

Figure 1.1: Free energy diagram for nucleation. The red line shows the change of Gibbs free energy ΔG as a function of radius r. The blue line shows the interfacial energy as a function of radius, the green line shows the volume energy as a function of radius.

volume term dominates and the nucleus grows spontaneously. The nucleation time τ can be predicted by the Arrhenius principle[15]:

$$\tau = \frac{\tau_0}{V} \exp\left[\frac{G(r_c)}{k_B T}\right], \tag{1.4}$$

where τ_0 is the characteristic relaxation time that is temperature-dependent, and k_B is the Boltzmann constant. Included in τ_0 is a factor that accounts for the rate at which new molecules or atoms are added to the critical cluster allowing it to grow. As the temperature decreases, the molecular rearrangements become slow causing τ_0 to increase[16]. In Eq. 1.3, at $T = T_m$, (T_m is the melting temperature), $G_S^0 - G_L^0$ equals zero, and the nucleation time diverges because the critical size and barrier to nucleation become infinite. At T_g, the nucleation time also diverges as the relaxation time becomes infinte. So there exists a temperature, T_{min}, at which nucleation time reaches its minimum, τ_{min}. The nucleation curve [17] (Fig 1.2) shows that the crystallization line and the nucleation line are separated. At high temperature, the liquid has low viscosity, and the nucleus grows easily. However, below a specific temperature, T_{sp}, the relaxation time exceeds the nucleation time, and hence the growth of nucleus is slowed by the high viscosity, which dominates the crystallization. To avoid crystallization, a subtle cooling schedule, shown by the dash line in Fig. 1.2 is needed, and the cooling rate then should reach at least $1/\tau_{min}$[18].

1.2.2 Kinetic Aspects of Glass

There are some common and dominating physical features of glass that provides understanding of glassy behavior and the potential applications of glasses[12]. The first one is the rapid increase in the shear viscosity with decreasing temperature[19]. And the most outstanding feature is the inhomogeneity of glass, both

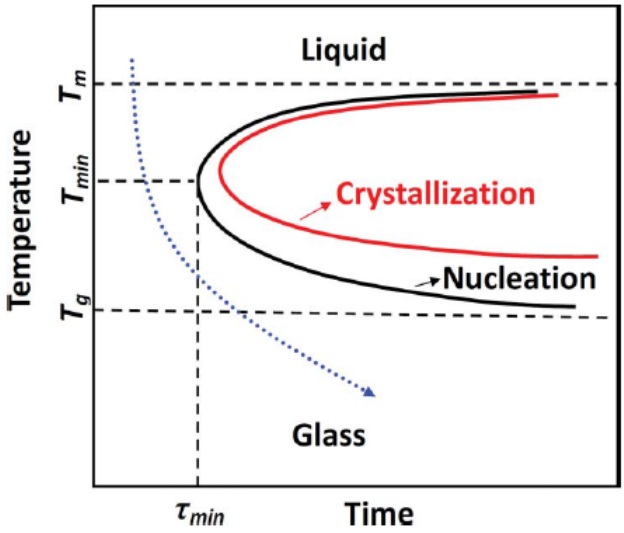

Figure 1.2: Temperature as a function of nucleation time. The dash line indicates a cooling schedule to form a glass. Reproduced under permission from reference [17]

structurally[20, 21] and dynamically[22, 23, 24].

The increase in relaxation time for some supercooled liquids such as SiO_2 and GeO_2, which are covalent bond network forming systems, can be well described by an Arrhenius behavior [25, 26, 27]:

$$\tau_\alpha = \tau_0 \exp(\frac{E}{k_B T}), \tag{1.5}$$

where τ_0 is the characteristic relaxation time, and E is an activation energy barrier associated with the structural rearrangement of the liquid that must be overcome. This equation suggests a rather simple activation mechanism for relaxation. For example, similar to the breaking a chemical bond.

Other liquids, referred as fragile liquids, exhibit a more remarkable slow-down in the dynamics, where the structural relaxation time increases 10-15 orders of magnitude in a very small temperature range as T_g is approached. This behavior can be reasonably well fit by the Vogel-Fulcher-Tamman equation (VFT)[28, 29, 30],

$$\tau_\alpha = \tau_0 \exp \frac{DT_0}{T - T_0}, \tag{1.6}$$

where $T_0 > 0$ is the temperature where the relaxation time is expected to diverge. Equation 1.6 suggests an effective activation energy obtained from the slope of VFT curve, which increases as T decreases. The divergence of the relaxation time at a temperature above $T = 0$ has led to the suggestion that there is a thermodynamic phase transition to an ideal glass state underlying the kinetic glass transition observed in experiment. The parameter D, then provides a measure of the degree of fragility. The rapid increase in the viscosity, indicating a growing energy barrier for molecular rearrangements, suggests the presence of cooperative motion[31], where the molecules need to rearrange in a concerted way. This is in contrast to the simple activated dynamics of strong liquids. Figure 1.3 shows the logarithm of τ_α as a function of

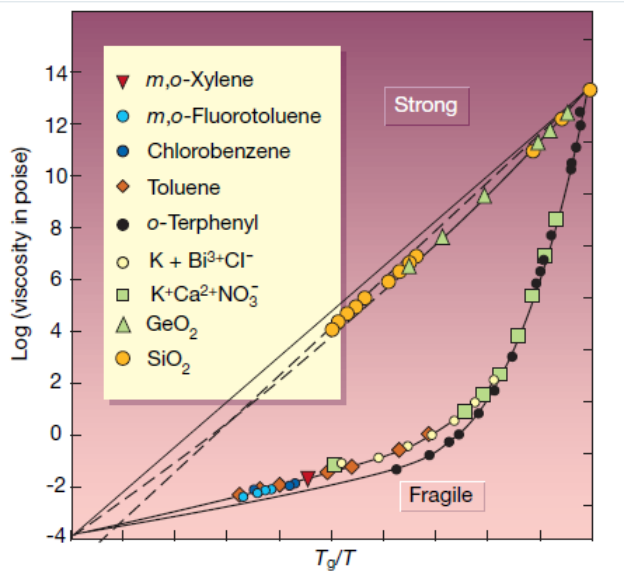

Figure 1.3: Arrhenius representation of liquid viscosities showing Angells strong fragile pattern. Strong liquids exhibit approximate linearity (Arrhenius behavior). Fragile liquids exhibit super-Arrhenius behavior, their effective activation energy increasing as temperature decreases. Reproduced under permission from reference [11]

$1/T$ near T_g region for several materials. And it also shows how the network forming liquids exhibit strong behaviour while the molecular liquids, which interact through weaker Van der Waals type interactions, are more fragile[32, 33].

There are other good fits for the fragile curves[12], such as Bassler Law[34]:

$$\tau_\alpha = \tau_0 exp(K(\frac{T^*}{T})^2). \tag{1.7}$$

A key feature of the parabolic expression is that it predicts the dynamics only diverge at T=0, which rules out the possibility of an ideal glass transition. Another fit is to replace $1/T$ by $1/T - 1/T_{on}$[35] , where T_{on} represent the onset temperature for cooperative behavior. The cooperative motion and the difference between the fragile/strong liquid give rise to the heterogeneity feature of glass. Spacial heterogeneity means that the cluster comprises both liquid-like and solid-like regions which have distinctive properties. Dynamic heterogeneity suggests that particles in some regions are faster or slower than the average, presenting relaxation time scale varies spatially[36, 37].

1.2.3 Thermodynamic Aspects of Glass

Based on the above analysis, a glass can be obtained by fast-cooling (to avoid crystallization) the liquid below its glass transition temperature T_g. Figure 1.4 shows the temperature dependence of a liquid's enthalpy (or volume) at constant pressure. The intersection of the liquid line and the glass line provides a definition of T_g[11]. T_g increases as the cooling rate increases: $T_{gb} \geq T_{ga}$. The reason is that the slower a liquid is cooled, the more time the molecules have to sample configuration space, which helps them remain in equilibrium to

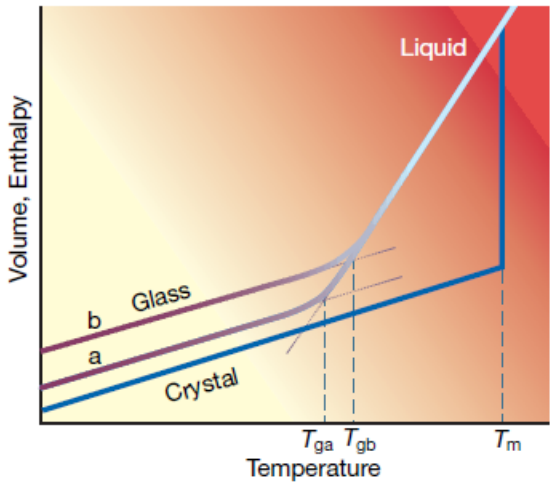

Figure 1.4: Temperature dependence of the liquids volume V or enthalpy H at constant pressure. T_m is the melting temperature. A slow cooling rate produces a glass transition at T_{ga}; a faster cooling rate leads to a glass transition at T_{gb}. Reproduced under permission from reference [11]

a lower temperature[38, 39]. However, in practice the dependency of T_g on the cooling rate is weak, so T_g is a nontrivial property.

The entropy of the liquid at T_m is higher than that of the crystal, and the heat capacity of the liquid is also larger than that of the crystal, and at the glass transition, the system falls out of equilibrium trapping the system in a state of high entropy. The entropy difference between the glass and the crystal, extrapolated to the absolute zero at a certain temperature, is known as the residual entropy.[40, 41]. So if the system is cooled more slowly, this entropy difference continues to decreases until the liquid entropy became equal to that of the crystal. If the glass transition did not occur, the entropy of the liquid would necessarily become negative as the system approaches $T = 0$. This is a phenomenon called the entropy crisis or the Kauzmann paradox[42], since the entropy is inherently a positive quantity. The entropy crisis could be avoided if the system underwent a phase transition to an ideal glass state at the Kauzmann temperature. Since the glass transition is a kinetic phenomenon, this indicates a connection between the kinetics and thermodynamics of supercool liquids and glasses[43], and the significance of investigating the kinetics and thermodynamics of glassy nanoparticles lies here.

1.3 Theories of glass transition

1.3.1 Adam-Gibbs Theory and Cooperatively Rearranging Region

Adam-Gibbs theory provides a connection between kinetics and thermodynamics[44, 45]:

$$\tau_\alpha = A \exp \frac{B}{T s_c}, \tag{1.8}$$

where A and B are constants, τ_α is the relaxation time and s_c is the configurational entropy, which is equal to the entropy difference between the supercooled liquid and corresponding crystal. In Adam-Gibbs theory, the concept of a cooperatively rearranging region (CRR) is provoked and these are the smallest number of particles required to rearrange cooperatively to produce particle motion and structural relaxation. Each CRR rearranges independently of any other region in the system and must be of a minimum size in order to lead to relaxation. This has the effect of breaking up the system into many distinct subsystems which provides a connection to their configurations. It is these CRR that give rise to dynamic heterogeneity and stretched exponential features observed in their relaxation time behavior.

The entropy of the liquid decreases more rapidly than that of the crystal, as shown in Fig.1.4 for o-terphenyl[11]. Were this trend to continue, when the system is further cooled, the entropy of the supercooled liquid would eventually equal the entropy of the crystal at a temperature called Kauzmann temperature, T_k. Since the configurational contribution to the specific heat is Tds_c/dT, the disappearance of s_c would lead to a discontinuity in the specific heat, indicating a phase transition at T_k and the divergence of relaxation time[46].

1.3.2 Potential Energy Landscapes

The potential energy landscape (PEL) is a convenient framework for understanding thermodynamic and dynamic aspects of the glass transition[47]. This theory was originally developed by Goldstein [48], and further developed by Stillinger [49]. The PEL has also been used extensively as a paradigm to describe the folding of proteins[47]. The principle separates the statistical-mechanical description of the many-body system into two distinct parts: the mechanically stable packing part and the vibrational part. The canonical partition function for a classical many-body system can then be transformed so that the temperature-independent packing statistics and the thermal excitations are uniquely separated. This requires the mapping of particle configurations in the multidimensional potential energy surface to local minima that can be reached by steepest-descent paths referred as quenches[49]. Configurations that map to the same potential energy minima are then collected together into local basins of attraction. Subsequently, the thermodynamics and dynamics of the liquid can be described in terms of the number of basins and the saddle points that separate them. Fig 1.5 shows this separation pictorially.

The canonical partition function for N structure-less particles at inverse temperature $\beta = 1/k_BT$ is:

$$Z_N = (\lambda^{3N} N!)^{-1} \int \exp(\beta\phi(\vec{r}))d\vec{r}, \tag{1.9}$$

where λ is the mean thermal de Broglie wavelength, ϕ is the potential energy of a configuration, $\vec{r} = \{r_1, r_2, , r_N\}$. Separating the partition function by the local minima causes the canonical partition function to transform formally from a multidimensional integral over all configurational coordinates to a one-dimensional

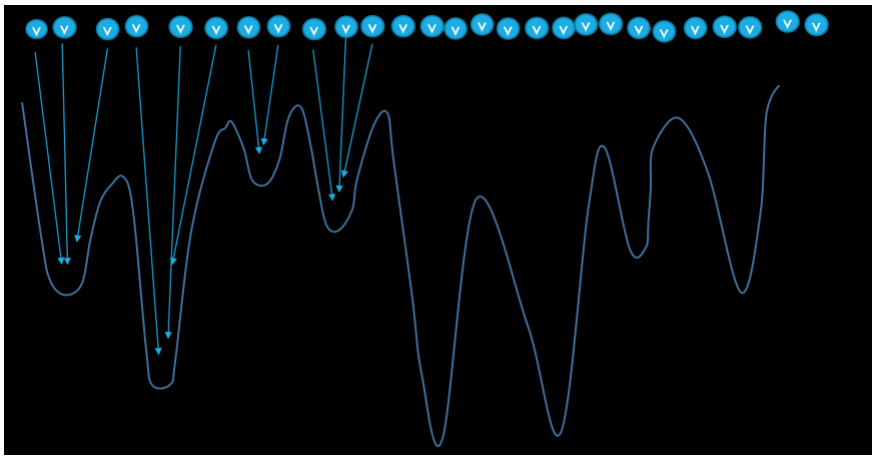

Figure 1.5: Classification of particle configurations according to multidimensional potential energy minima that can be reached by steepest-descent paths called quenches.

integral over potential energy[49],

$$Z_N = \lambda^{-3N} \int_{i=\phi_0}^{\phi_u} \exp(Ng(\phi) - \beta m - \beta f(\beta, \phi)) d\phi, \tag{1.10}$$

where ϕ is the potential energy, ϕ_0 and ϕ_u is limit of the potential energy region, $g(\phi)$ is the enumeration function that accounts for the number of basins with a given potential energy. This one-dimensional partition function is convenient in understanding glass phenomena. The thermodynamic and dynamics of the system can then be described in terms of the number of basins, and how the system moves between them as a function of temperature. At sufficiently high temperature, the system is ergodic. And it is able to sample all possible basins. However, in the thermodynamic limit, the system samples the set of basins that minimize the free energy. At a low enough temperature the system eventually becomes stuck in a single minimum. As the cooling rate of the liquid is decreased, the system has more time to explore the PEL and is able to to find its way to deeper minima, of which there are fewer. This corresponds to the glass transition.

Reviewing Adam and Gibbs theory in terms of the PEL description, one can separate entropy into two distinct parts: the entropy of vibration inside one minima and the number of distinct mechanically stable minima. The so-called configurational entropy can be expressed[48]:

$$s_c = \log N_{metastable}, \tag{1.11}$$

where $N_{metastable}$ is the number of basins that is accessible to the metastable liquid of the temperature T. Then the configurational entropy is defined as a the logarithm of the number of existing energy minima. Thus, in particular, the ideal glass transition can be understood as the situation where the system becomes trapped in a unique low energy basin, and where configurational entropy vanishes[50].

1.3.3 Geometric Frustration

The theory of structural changes leading to the glass transition have been investigated extensively[51, 52, 53]. Despite the fact that crystalline structure has been well understood, for instance by coordination number, and that glassy structure occurs when crystallization is avoided, the relationship between structural changes and glass transition has been elusive[54, 55, 56]. Theories of the glass transition that focus on the role of local structure in liquid phase argue that certain types of local, low energy structures that cannot pack to form crystals effectively frustrate crystal formation[12].

One recent theory, involving geometric frustration, proposes that the glass transition can be seen as a crystallization-like transition in curve space, where the curve "crystal nuclei" are frustrated in Euclidean space. In three dimensions the icosahedron is locally the most dense arrangement of atoms, but it does not pack space. However, as space is curved, the icosahedra becomes a more efficient packing and the glass transition disappears[57]. A recent article describes the existing clusters in Kob-Andersen system topologically, which indicates that a bi-capped squared antiprism is the main type of static order causing the dynamic slowdown[58]. Again, this local order is energetically favourable, but it is not compatible with forming a crystal in this system. Similarly there is evidence that in the glassy nanoparticle system, these bi-capped squared antiprisms form a connecting network, retarding the motion of molecules[59]. It is also worth noting that, ultrastable glass, which are formed through the vapour deposition of a material onto a cold substrate, have extremely low energies and large numbers of these locally favoured structures including the bicapped squared antiprism[60].

The nanobeam electron diffraction technique has been utilized to probe the local atomic structure in metallic glass and there is evidence of cluster-assembled structures of metallic glass systems[61].

1.3.4 Dynamic Facilitation

Fluctuations are the subject of dynamic heterogeneity[62, 63] and they are reflected in various dynamic parameters[64]. For example, the dynamic structure factor $F_s(q,t)$, which can be assessed experimentally by inelastic neutron scattering[65], exhibits a plateau in the supercooled liquid above the glass transition temperature. At high temperatures, because the atoms move freely without collective interactions, the decay of $F_s(q,t)$ can be simply described by a normal exponential relaxation with a single relaxation time[66]. This is shown in Fig. 1.6. As the temperature decrease, the decay of $F_s(q,t)$ reaches a plateau at intermediate times and then presents another exponential decay. This is a feature of slow dynamics at low temperature[67]. The mean square displacement (MSD) of the atoms tells the same story. The MSD has an early time behavior where $< r^2(t) >$ is linear with t^2, dominated by ballistic dynamics, followed by a diffusive regime, where $< r^2(t) >$ is linear with t and the motion is dominated by collisions. However, when approaching T_g, the ballistic and diffusive regimes are separated by a plateau, where the labelled atoms are beyond the ballistic regime. It seems that some underlying mechanism is preventing the atoms from a typical diffusive motion,

such that the atom remains confined in a small cage surrounded by its neighbors[68, 69].

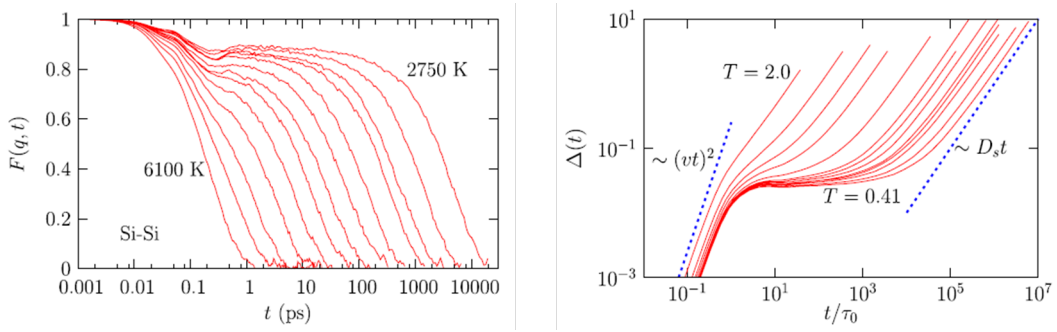

Figure 1.6: Left: The plateau emergence observed near T_g from incoherent intermediate scattering function $F_s(q,t)$. Right: mean square displacement $<r^2(t)>$. Reproduced under permission from reference [12]

Structures with fluctuations can be resolved by investigating parameter fields[70]. One of these is:

$$K = \int_V d\vec{r}\Delta t \sum_{t=0}^{t_{obs}} \kappa(\vec{r}, t; \Delta t), \tag{1.12}$$

where the integral extends over the net volume of the system, V, and

$$\kappa(\vec{r}, t; \Delta t) = \sum_{i=1}^{N} \left[\vec{r}_i(t + \Delta t) - \vec{r}_i(t)\right]^2 \delta(\vec{r} - \vec{r}_i(t)), \tag{1.13}$$

where $\delta(\vec{r} - \vec{r}_i(t))$ is Dirac's Delta. The function $\kappa(\vec{r}, t; \Delta t)$, is a mobility field, similar to the MSD that measures the ability of a particle to move over time.

The calculated result of $\kappa(\vec{r}, t; \Delta t)$ for a systems of Lennard Jones atoms[70] is shown in Fig.1.7. Darker shading represents a more significant displacement. White shading means nil displacement. Typically, at high enough temperature, string-structures emerge and then retract from the central dark region. However, at temperature around T_g, string-like structures emitted from one dark region no longer retract, but rather meld into the original dark region. Again, from the new, larger dark region, further string-structures surge[70]. These features demonstrate a facilitated dynamics –mobility in a region of space that induces following motion in an neighbouring region, and dynamics on small length scales surge easier than dynamics depending on cooperative motions.

Dynamic facilitation provides an indication why a glass can form and why it may age very slowly[71]. There are deep basins in trajectory space where initial conditions are remembered for all times. Those corresponding to ordered crystals are often easily accessible at equilibrium conditions. However, those associated with disordered solids not seen at equilibrium but occur in ensembles weighted away from equilibrium, can still be remembered for times far into the future and become nonergodic glassy states driven under specific conditions[70]. In the case of dynamic facilitation, the glass transition represents a a dynamic transition in trajectory phase space rather than a thermodynamic or structural transition as suggested by other theories.

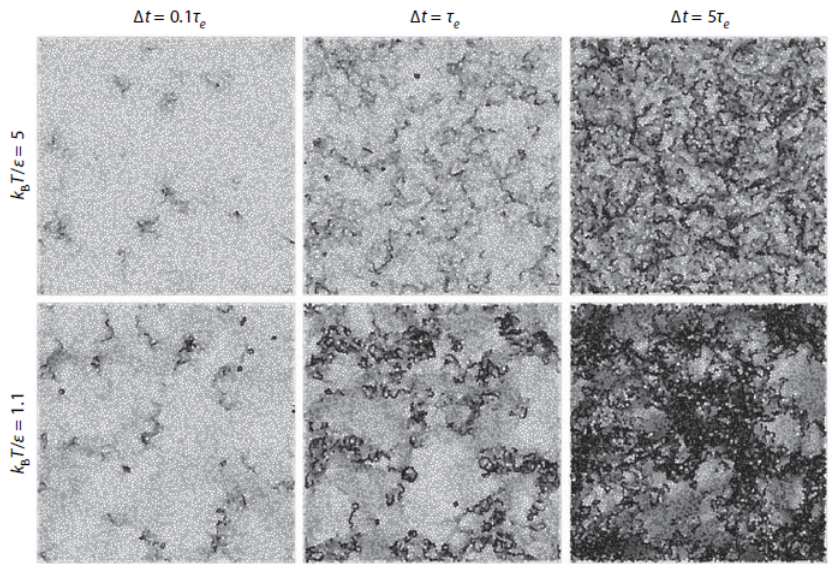

Figure 1.7: The pictures are renderings of the mobility field $\kappa(\vec{r}, t; \Delta t)$ for typical equilibrium trajectories of 10^4 particles. The displacement time,t, is given in reference to the $1/e$ time for the Van Hove self-correlation functions at the corresponding temperatures. The rendering shades each particle according to the size of the particles displacement from its initial position. Reproduced under permision from reference [70]

1.4 Molecular Dynamic Simulation

1.4.1 Overview

While experiments are the core of chemistry, all experimental methods have intrinsic and practical limitations. An alternative is to use numerical applications of various theoretical models, such as computer simulations. Such studies can give complementary information on the problem studied, essentially forming a bridge between theory and experiment. In particular, simulations can provide molecular level insight that is difficult to obtain directly through experiment and can often be performed under conditions not accessible to experiment. For example, under high pressure, or very at extreme temperatures.

Molecular dynamics (MD) simulation is one of the numerical methods applied in modelling mesoscale and nanoscale systems. The basic principle of MD is to model the system with an appropriate potential that describes the interactions between the atoms or molecules. With the potential energy known for a given configuration of the atoms it is possible to calculate the forces and use Newtons equations of motion to describe how the system evolves with time. The properties of the system can then be calculated from configurations of the atoms at different times.

1.4.2 Statistical Mechanics

Molecular dynamics simulation generates a sequence of points in phase space as a function of time subject to a series of conditions that define the ensemble. There are several different ensembles used in statistical mechanics[72] that can be sampled by molecular dynamics simulation:

1. Microcanonical ensemble (N, V, E): a collection of systems with a fixed number of atoms, N, a fixed volume, V, and a fixed energy, E. This corresponds to an isolated system.

2. Canonical Ensemble (N, V, T): This is a collection of systems with a fixed number of atoms, N, a fixed volume, V, and a fixed temperature, T.

3. Isobaric-Isothermal Ensemble (N, P, T): This ensemble is characterized by a fixed number of atoms, N, a fixed pressure, P, and a fixed temperature, T.

4. Grand canonical Ensemble (μ, V, T): A collection of systems with a fixed chemical potential, μ, a fixed volume, V, and a fixed temperature, T.

In Monte Carlo simulation, that generate a set of states as part of a Markov chain satisfying detailed balance [73], averages corresponding to experimental observables are defined as ensemble averages, which are taken over a large number of replicas of the system considered simultaneously:

$$< A >_{ensemble} = \sum_s A_s P_s, \tag{1.14}$$

where $< A >_{ensemble}$ is the ensemble average of a physical quantity, A_s is the physical quantity of a specific state s, and P_s is the probablity of the state. For example to calculate the potential energy $< U >$ of a canonical system, it is necessary to start with partition function Z_N, which involves an integration over all possible configurations $(x_1, \cdots, x_N)$:

$$Z_N = \int e^{-\beta U(x_1, \cdots, x_N)} dx_1, \cdots, dx_N, \tag{1.15}$$

where $\beta = \frac{1}{k_B T}$, k_B is Boltzmann constant. Based on statistics theory, then the potential energy obtained by ensemble average is:

$$< U >= \frac{1}{Z_N} \sum_s U_s e^{-\beta U_s}. \tag{1.16}$$

In practise, the Monte Carlo method is designed to generate states with the correct probability, assuming that the system is ergodic and can effectively sample configuration space. In molecular dynamics simulations, one calculates time averages by measuring the property in independent configurations of the system that are well separated in time. Resolving this leads us to one of the most fundamental axioms of statistical mechanics, the ergodicity hypothesis, which states that the time average equals the ensemble average[74]:

$$< A >_{ensemble} = < A >_{time} . \tag{1.17}$$

The mechanism is that if one allows the system to evolve in time indefinitely, the system will eventually pass through all possible states visiting each micro state with the correct probability. The purpose of a molecular dynamics simulation is to generate enough representative configurations such that this equality is satisfied. Fortunately, in practice it is not necessary for the simulation to sample every state, which would take the age of the universe in any reasonably sized system, because the average properties are dominated by a few highly probable states.

1.4.3 Molecular Dynamics Algorithm

The basic routine of molecular dynamics simulation is[75]:

1. Set the initial conditions: initial velocity, v_0, and positions.

2. Get the forces $F_i(t)$ and update neighbour list.

3. Solve equations of motion over dt.

4. Perform ensemble control.

5. Move the system one time step from t to $t + dt$ by a chosen integration algorithm.

6. Calculate the desired physical quantities.

The core of molecular dynamics simulation scheme is the potential $U(r_{ij})$ used to describe the atomic interactions, where r_{ij} is the vector connecting two atoms. There are many potentials used to describe glass forming liquids, but the four commlonly used potentials are:

1. Hard sphere potential[76]:

$$U(r_{ij}) = \begin{cases} 0, r_{ij} > \sigma \\ \infty, r_{ij} < \sigma \end{cases} \tag{1.18}$$

   Here σ is the diameter of the sphere. This is the simplest potential that describes the exclusive interaction without any cohesive interaction and is commonly used in theoretical investigations of idealized problems.

2. Ionic potential[77]:

$$U(r_{ij}) = \frac{q_i q_j}{r_{ij}}. \tag{1.19}$$

   This is the Coulomb interaction of charges, where q_i, q_j are the signed magnitudes of the charges. It is often used to account for charge-charge interaction or polarization.

3. Lennard-Jones potential:

$$U(r_{ij}) = 4\epsilon[(\sigma/r_{ij})^{12} - (\sigma/r_{ij})^{6}], \tag{1.20}$$

where ϵ is the depth of the potential well, and σ is the finite distance at which the inter-particle potential is zero[78]. This is the van der Waals interaction in inert gases and molecular systems and is often used to model general effects rather than properties of a specific material. This is the potential chosen for my research.

4. Morse potential[79].

$$U(r_{ij}) = \epsilon[e^{-2\alpha(r_{ij}-r_0)} - 2e^{-\alpha(r_{ij}-r_0)}], \tag{1.21}$$

where α controls the energy of the bond. It is similar to Lennard-Jones but is a more bonding orientated suitable for interactions when attractive force comes from the formation of a chemical bond.

When the force model is selected, Newtons second law,

$$F = ma = m\frac{dv}{dt} = m\frac{d^2x}{dt^2},$$

where x is used to describe an atom direction, is used to determine the acceleration of each atom in the system[80]. Integration of the equations of motion then yields a trajectory that describes the positions, velocities and accelerations of the atoms as they vary with time. From this trajectory, the average values of properties can be determined. The method is deterministic; once the positions and velocities of each atom are known, the state of the system can be predicted by:

$$x = \frac{1}{2}at^2 + v_0t + x_0, \tag{1.22}$$

where v_0, x_0 are the initial velocity and initial position, respectively. Commonly used algorithms for the integration of Newton's second law are[73, 81, 82]: the Verlet algorithm, the Leap-frog algorithm, the Velocity Verlet and the Beemans algorithm. All the algorithms assume the positions, velocities and accelerations can be approximated by a Taylor series expansion. The Verlet algorithm is used in this research and is described in next section.

1.4.4 Verlet Algorithm

The integration of Newton's second law of motion is performed by Verlet algorithm. An integrator advances the trajectory over small time increment Δt:

$$\vec{X}^{3N}(t_0) \rightarrow \vec{X}^{3N}(t_0 + \Delta t) \rightarrow \vec{X}^{3N}(t_0 + 2\Delta t)...\vec{X}^{3N}(t_0 + L\Delta t), \tag{1.23}$$

where $\vec{X}^{3N}$ is the position vector of the atom and L is usually within $10^4 - 10^7$. There are many methods for integration of Newtons equation of motion and Velocity Verlet Algorithm (VVA)[75] is used for the current research. Assuming the atomic trajectory, $\vec{X}^{3N}(t)$, is smooth, the initial configuration is based on sites of a square lattice, and velocity is generated by random normal distribution with magnitude determined by the temperature scale starting with $\vec{X}^{3N}(t_0)$ and $\vec{V}^{3N}(t_0)$:

$$\vec{X}^{3N}(t_0 + \Delta t) = \vec{X}^{3N}(t_0) + v_i(t_0)\Delta t + 1/2(\frac{f_i}{m})(\Delta t)^2 + o(\Delta t)^4, \tag{1.24}$$

where f_i is the force. After the coordinates $\vec{X}^{3N}(t_0 + \Delta t)$ are calculated, $f^{3N}(t_0 + \Delta t)$ can be evaluated and the velocity is then obtained:

$$V_i(t_0 + \Delta t) = V_i(t_0) + 1/2[(f_i(t_0)/m) + ((f_i(t_0 + t))/m)]\Delta t. \tag{1.25}$$

The system has advanced by one step. Since $\vec{X}^{3N}(t_0 + \Delta t)$ and $V_i(t_0 + \Delta t)$ are known at the same time, this algorithm is convenient to use.

Concerning the precision of this algorithm, it is interesting to know to what degree does the outcome of the above recursion scheme mimic the real trajectory $\vec{X}^{3N}(t_0)$. In Eq. 1.24, assuming $X_i(t_0)$ and $v_i(t_0)$ are exact, and assuming a perfect computer with no machine error associated with storing the numbers or carrying out floating-point operations, the computed $\vec{X}^{3N}(t_0 + \Delta t)$ would still be off from the $\vec{X}^{3N}(t_0 + \Delta t)$ by $0(\Delta t)^4$, which is an intrinsic error of the algorithm. And this is a local truncation error (LTE)[83].

Clearly, as $\Delta t \to 0$, $LTE \to 0$, but that does not guarantee the algorithm works, because what we want is $X_i(t_0 + t')$ for a given t', not $X_i(t_0 + \Delta t)$. To obtain $X_i(t_0 + t')$, we must integrate $L = t'/\Delta t$ steps, and the difference between the computed $X_i(t_0 + t')$ and the real $X_i(t_0 + t')$ is called the global error[75]. An algorithm can be useful only if when $\Delta t \to 0$, the global error goes to 0.

It is also important to be aware of the time scales accessible by simulation. The slowest cooling rate we can reach in simulation is still several orders of magnitude faster than that of experiment. Nevertheless, we can measure molecular details that are difficult to examine directly by experiment.

1.5 Structural Analysis

1.5.1 Radial Distribution Function

The radial distribution function gives the probability of observing a second molecule with a distance r relative to that probability of the ideal gas situation, and it can be used to understand how atoms are distributed in the system.

Based on the partition function, the probability that we have atom 1 at a fixed point r_1 in dr_1, and atom 2 at a fixed point r_2 in dr_2, etc etc is[84]:

$$P^N(r_1, , r_N)dr_1...dr_N = \frac{exp[-\beta U(r^N)]dr_1...dr_N}{Z_N}, \tag{1.26}$$

where $Z_N = \int exp[-\beta U(r^N)]dr^N$ is the partition function.

To obtain the probability of finding atom 1 at a point r_1, atom 2 at a fixed point r_2, ..., atom n at a fixed point r_n, independent of the position of the other atoms, it is necessary to integrate over the positions of the remaining $N - n$ atoms:

$$P^n(r_1, , r_n) = \frac{\int exp[-\beta U(r^N)]dr_{n+1}...dr_N}{Z_N}. \tag{1.27}$$

Here the particle identities remain. To obtain the probability of finding any n atoms with fixed positions it is necessary to take into account the number of ways of choosing the n particles, which gives [84]:

$$\rho^{(n)}(r_1, \cdots, r_N) = \frac{N!}{(N-n!)} P^{(n)}(r_1, \cdots, r_N). \tag{1.28}$$

A correlation function $g^{(n)}$ can be defined such that it measures deviations away from a random distribution:

$$\rho^{(n)}(r_1, \cdots, r_n) = \rho^{(n)} g^{(n)}(r_1, \cdots, r_n), \tag{1.29}$$

where

$$g^{(n)}(r_1, \cdots, r_n) = \frac{N! V^n}{N^n (N-n)! Z_N} \int \cdots \int exp(-\beta U_N) dr_{n+1} \cdots dr_N. \tag{1.30}$$

The radial distribution function is the most important of these:

$$g^{(2)}(r_1, r_2) = g^{(2)}(r_{12}) = g(r) \tag{1.31}$$

as it can be related to thermodynamic properties such as Helmholtz free energy, pressure and the static structure factor of the system. It can also be obtained in practice using X-ray diffraction or neutron diffraction, giving a direct link between simulation and experiment[85].

Figure 1.8 shows a typical radial distribution function for the single component Lennard-Jones liquid. At distances short compared to the atom diameter, $g(r)$ is zero because of the volume exclusion associated with the repulsive core. The peak structure structure identifies the local ordering around an atom, with the first peak identifying the local cage structure. Since the liquids have no long range order the peaks decay away to one, indicating a random ideal gas type structure[40].

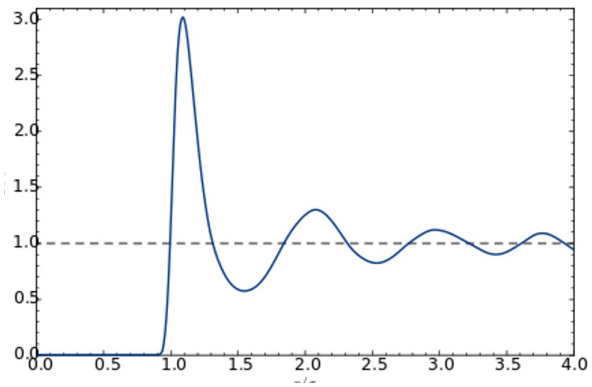

Figure 1.8: Radial distribution function for Lenard-Jones liquid.

In the case of crystal, the radial distribution features peaks with the periodic crystal structure. Fig. 1.9 shows the $g(r)$ of face center cubic(FCC) and FCC-HCP(Hexagonal closed packed) mixture structures[86].

In the case of mixtures, such as a binary mixture containing two different atom types A and B, it is possible to decompose the radial distribution function into its components, $g_{AA}(r)$, $g_{BB}(r)$ and $g_{AB}(r) = g_{BA}(r)$. The radial distribution function can be used to distinguish liquid/glassy and crystalline systems. Since the

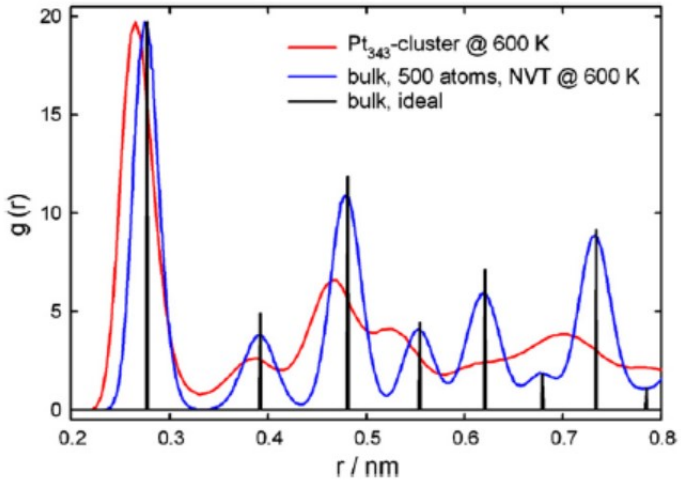

Figure 1.9: Radial distribution function for FCC (blue line) and FCC-HCP mixture (red line). Reproduced under permission from [86]

first peak/minima of the radial distribution indicates the first atomic layer of the center, it can also be used to identify the cut-off distance for different types of neighbor analysis method such as the Common Neighbor Analysis and the calculation of bond order parameters.

1.5.2 Common Neighbor Analysis

Although crystal structures can be identified by comparing radial distribution function peaks with a standard structure, many times different structures are present in a simulated configuration, all of which generate peaks leading to a complex pattern. For example, the peaks from face centred cubic (FCC) and hexagonal close packed (HCP) crystals overlap to generate broad peaks.

Common neighbor analysis (CNA) provides a way to identify the local structures around an individual atom. CNA is commonly used in the study of crystalline alloy structures[87]. It is a correlation method used to detect local structure arrangements based on the local topology. Each pair of nearest neighbor atoms is given a CNA index, (j, k, l), where j is the number of nearest neighbors belonging to both atoms, k is the number of bonds in these j atoms, l is the number of bonds in the longest connecting chain formed by the k bonds. Two atoms are considered to have a bond if the distance between them is smaller than a threshold distance r_{cut} determined by the first minima of radial distribution function. For instance, in Fig. 1.10, the atom pair (in red color) have 6 neighbor atoms connected, so $j = 6$. Only 4 bonds formed by these 6 neighbor atoms, so $k = 4$. And one can see that only 3 chains are linked, that is the length of the longest chain in the $k = 4$ bonds is 3, so $l = 3$.

n_{CNA} triplets (j, k, l) in the n_{CNA} neighbor bonds: $n_{CNA}(i, j, k)$ are compared to a reference indexes to assign a crystal structure. For instance, FCC has $12(4, 2, 1)$, HCP has $6(4, 2, 1), 6(4, 2, 2)$, and body center cubic (BCC) has $6(4, 4, 4), 8(6, 6, 6)$[88]. Figure 1.11 visualizes the configurations of FCC, ICO (icosahedron),

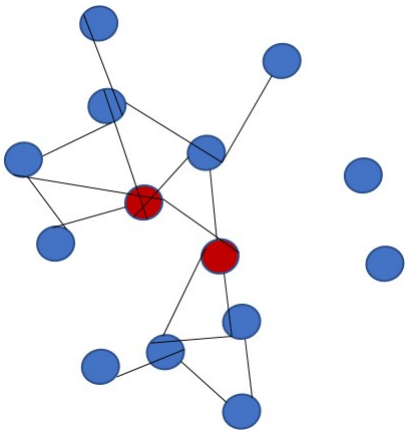

Figure 1.10: A cluster of atoms with bonds connected when the distance between the two atoms are less than r_{cut}. CNA index of the red atom pair is (6,4,3)

HCP and BCC structures. The CNA method can be used in binary system on the condition that the radius of the two atoms are close. For more precise classification, the CNA has to be extended to Binary CNA by considering the atom identity as a criterion[86].

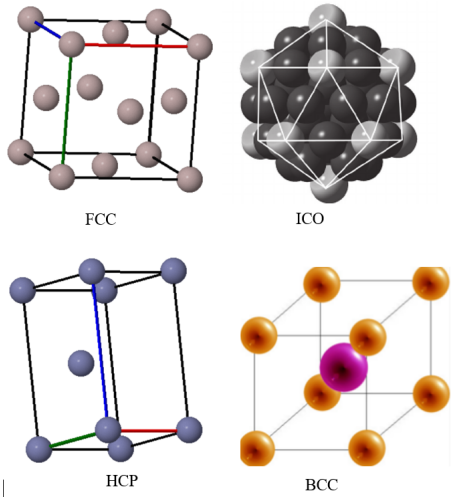

Figure 1.11: Atomic arrangement for FCC, ICO, HCP and BCC (CsCl for binary components) structures.

1.5.3 Bond Order Parameters

Gases and liquids, well below the critical point, can easily be distinguished on the basis of density. However, liquids and different crystal structures often have very similar densities, but they do exhibit symmetry differences. The broken symmetry of the crystal relative to the liquid can be identified in terms of orientational order around an atom. Steinhardt et al.[89] introduced bond orientational order parameters based on spherical harmonic functions to study the formation of FCC, HCP and icosahedral order in supercooled liquids and

glasses. They have now been used in various forms to study a variety of different systems including single component Lennard-Jones clusters[90], a Gaussian core system[91] and metallic glass[92].

The neighboring atoms of a given atom (i) can be defined as those atoms that have an interatomic distance less than a cutoff radius of a given value, generally equal to the distance of the minimum between the first and the second peaks of the pair correlation function[91]. A bond joining two neighbours is defined by a vector joining the atoms' center. The complex vector for a atom (i) associated with a bond $r_{ij} = |r_i - r_j|$ are the set of numbers[93]:

$$q(i)_{lm}(r_{ij}) \equiv Y_{lm}(\theta(r_{ij}), \phi(r_{ij})), \tag{1.32}$$

where $\theta(r_{ij}), \phi(r_{ij})$ are the polar and azimuthal angles of the bond with respect to an arbitrary but fixed reference frame, $Y_{lm}(\theta(r_{ij}), \phi(r_{ij}))$ are the usual spherical harmonics, l is a integer parameter and m is an integer that values from $m = -l$ to $m = +l$.

Since the bond between atoms i and j may be arbitrarily taken as either r_{ij} or $r_{ij} = -r_{ji}$, it is helpful only to consider the even-l vector $q(i)_{lm}(r_{ij})$, because such bond inversions would affect these parameters. The complex vector of atom (i) is then attained by averaging $q(i)_{lm}(r_{ij})$ over all nearest neighbor atoms:

$$q(i)_{lm} = \frac{1}{N_b} \sum_{N_b(i)} q(i)_{lm}(r_{ij}), \tag{1.33}$$

where N_b is the number of nearest neighbor atoms. Then the local order parameters of atom (i) and invariant with respect to rotations of the reference frame, $q0(i)_l$ is[91]:

$$q0(i)_l = \sqrt{\frac{4\pi}{2l+1} \sum_{m=-l}^{l} |q(i)_{lm}|^2}, \tag{1.34}$$

Global bond order parameters Q_{lm}, Q_l can be defined by the same spherical function, which can be applied to identify global structures of an entire cluster. For a global bond order parameter, the average spherical harmonics is calculated over all bonds found in the cluster:

$$Q_{lm} \equiv \frac{1}{N_{bonds}} \sum_{bonds} Q_{lm}(r_{ij}), \tag{1.35}$$

and

$$Q_l \equiv \sqrt{\frac{4\pi}{2l+1} \sum_{m=-l}^{l} |Q_{lm}|^2}. \tag{1.36}$$

In both a liquid and a crystal, atoms experience a variation in their local environment as a result of thermal motion. This gives rise to a distribution of bond orientational orders and the identity of a given atom is determined by comparing its value against the distributions of each phase. In some cases, the distributions of the phases overlap making difficult to determine an atom identity. This can be overcome by using more than one order parameter. For example, by constructing a two dimensional plane of $q0(i)_4$-$q0(i)_6$, the crystal structure of an atom can be identified by its position in the plane. This method has been successfully applied to distinguished BCC and FCC blocks occuring in the crystallization of supercooled liquids of Xenon at high temperature and high pressure[94].

1.5.4 Average Bond Order Paramters

Lechner and Dellago[91] proposed a method to increase the accuracy of the crystal structure determination, which extends the average of the bond order parameters over nearest neighbor atoms as well, giving

$$qA(i)_l = \sqrt{\frac{4\pi}{2l+1}\sum_{m=-l}^{l}|qA(i)_{lm}|^2}, \tag{1.37}$$

where

$$qA(i)_{lm} = \frac{1}{N_{neighbor}}\sum_{N_{neighbor}} q(i)_{lm}. \tag{1.38}$$

Here, the sum over $N_{neighbor}$ runs over all neighbors of the center atom (i) plus the center atom itself. Thus, to calculate the $qA(i)_{lm}$ of the center atom, one uses the local orientational order vectors $q(i)_{lm}$ averaged over the center atom and its surroundings. While $q0(i)_l$ holds the structural information of the first shell around the center atom, its averaged version $qA(i)_l$ also consider atomic structure in the second shell. Using the parameter $qA(i)_l$ instead of $q0(i)_l$ increases the accuracy of the identifying different structures by means of a coarsening of the spatial resolution. The $qA(i)_4$-$qA(i)_6$ have been used to identify different structures in Lenard-Jones liquid and Gausiann core form model for nucleation study[91].

1.5.5 Disorder Parameter

Kawasaki and Onuka[95] used the Steinhardt orientational bond order parameters as the basis for developing disorder parameters used in binary Lennard-Jones particles in three dimensions to distinguish local environment. Consider the scalar product of bond order parameter:

$$S_{ik} = \sum_{m=-l}^{l} q_{lm}^{i}(q_{lm}^{k})^*, \tag{1.39}$$

where $(q_{lm}^{k})^*$ is the conjugated vector of q_{lm}^{k}. The larger the S_{ik}, the more aligned the two vectors are, indicating a similar of local environment. When the alignment is perpendicular, this scalar product goes to zero, showing no similarity of the local environment. For every atom (i) in the nanocluster, the disorder parameter can be calculated as:

$$D(i) = \frac{1}{N_b}\sum_{N_b}(S_{ii} + S_{kk} - 2S_{ik}), \tag{1.40}$$

If the vectors are normalized, S_{ii} and S_{kk} are always equal to 1. If atom (i) and (k) share the same environment, then $2S_{ik}$ is close to 2, and $D(i)$ is close to zero. If atom (j) and (k) are very disorder, $2S_{ik}$ goes to zero and $D(i)$ is close 2. Thus, when $D(i)$ goes to 2, the two local atomic environment are anti-correlated. Finally, the overall disorder of the cluster can be represented by the average of $< D >$ over all the atoms:

$$< D >= \sum_{i=1}^{N}\frac{D(i)}{N}. \tag{1.41}$$

Being a highly ordered system, the crystal has a small non-zero $< D >$ value that arises from the vibrations of the atoms around their local lattice sites. For atoms in grain boundaries or crystal defects, $< D >$ has values of $(0.1 - 0.5)$. $< D >$ increases dramatically in the crossover from a poly-crystalline solid to glass.

1.5.6 Voronoi Analysis

The featured peaks in the distribution of the bond orientational order parameters are useful to distinguish liquid and solid-like structures. Glassy structure and liquid structure are similar and have large overlap in their distribution of bond order parameters, making it difficult to analyse glassy structures using bond order parameters. The local structure of an atom in an amorphous system such as a liquid and glass can also be characterized by means of Voronoi Analysis[88]. The Voronoi tessellation divides the volume of space surrounding a set of points, such as a particle center in a configuration of atoms, into a series of polyhedra (see Fig.1.12a for a two dimensional Voronoi tessellation construction). Any point within a given polyhedra lies closest to the center point than any other atom center and the bisecting boundary denotes the line of equidistant points between two atoms centres. In the case of a polydisperse atomic systems, where the atoms are represented by different size spheres, it is necessary to use the radial plane construction to complete the tessellation. This weights the distance between atom centres according to their sizes and ensures the bisecting plane is located between the spheres at contact[96]. This is demonstrated in Fig.1.13 Therefore the overlapping of the Voronoi plane and the large-size atoms can be avoided.

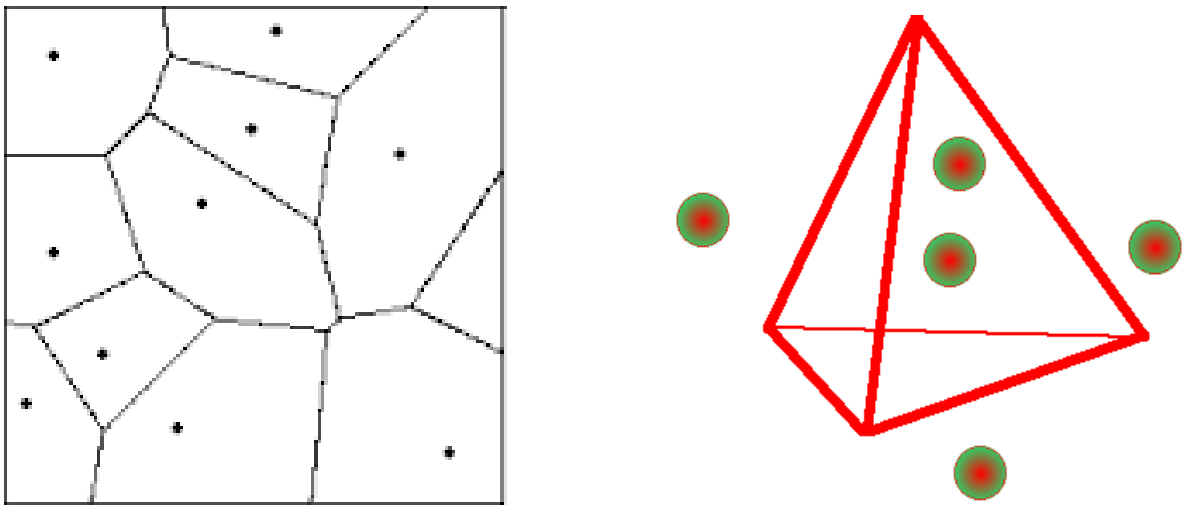

(a) **(b)**

Figure 1.12: (a): Two-dimensional Voronoi tessellation construction. (b): A Voronoi Cluster of tetrahedron in three dimension. Red lines provide a guide to the eye.

The Voronoi tessellation has been used extensively in simulation to study the structure of amorphous materials[97, 98]. It has been applied to investigate the stability of metal alloys[98] and the glass forming

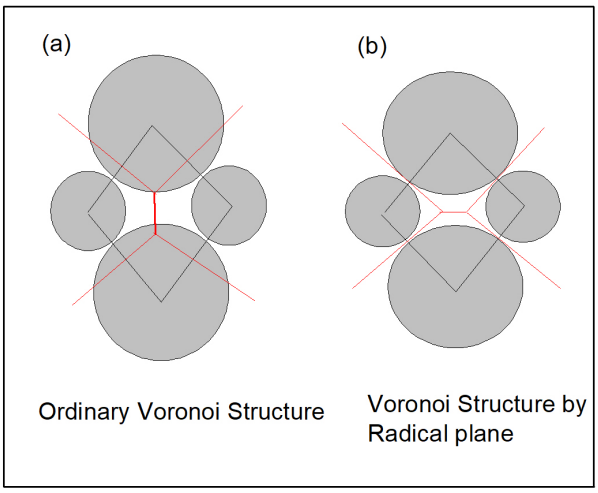

Figure 1.13: A comparison of (a) two-dimensional graphs of the ordinary Voronoi tessellation and (b) the radial plane construction. In case of radial plane construction, the bisetting method takes the radius into account. The local structure, i.e., the number of faces for the Voronoi cell also depends on the atom size. Reproduced under permission from[96].

mechanism of metallic glasses[99]. In particular, nearest neighbors can be identified as those atoms that share a face of the polyhedra. The Voronoi analysis is rarely used in crystal structures. The reason is that the Voronoi vertices generated from symmetric crystal structure are very sensitive to thermal fluctuation. And two different structure could have the same set of Voronoi index. So it is mainly used in structures without long-range order, such as liquid and glass.

The environment around an atom can be characterized by Voronoi index which lists the number of faces with i edges: $(n3 \quad n4 \quad n5 \quad n6 \cdots)$. In most situations, only $n = 3$ to 6: $(n3 \quad n4 \quad n5 \quad n6)$ are used since high index values are rare[17]. For example: the bicapped squared antiprism found in ultra stable glass[17] is (0 2 8 0). The structure of (0 2 8 0) is shown in Fig. 1.14. The Voronoi index for an icosahedron is (0 0 12 0). The sum of the indices also give the total number of nearest neighbors.

1.6 Structure in Lennard Jones Nano Particles

The structure of small nanoparticle clusters is of considerable interest because they form a variety of structures not observed in the bulk. They also have a large surface to volume that makes them attractive for applications in catalysis. The Lennard-Jones potential is the one of the simplest that has an attractive well making it possible to form clusters and the structure of these have been studied extensively[47]. When the temperature is low enough, the cluster's potential energy minimum will be the global free energy minimum. For a small size

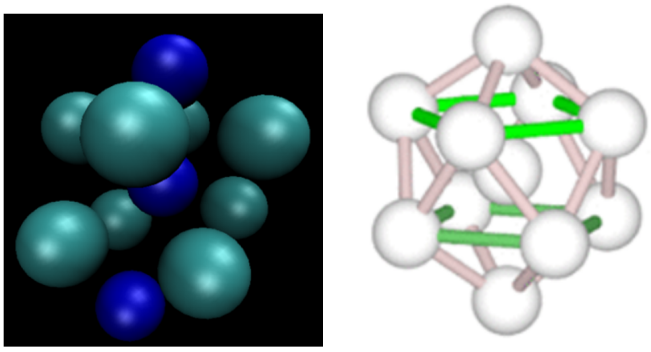

Figure 1.14: Atomic arrangement for a bicapped squared antiprism Voronoi cell.

single component Lennard-Jones cluster range $0 - 1000$, the majority of its global minima can be described as Mackay icosahedra[100], with perfect icosahedra occuring with size 13, 55, 147, 309, 561.... These low energy "magic number" clusters are generated by the formula,

$$\frac{1}{3}(10n^3 + 15n^2 + 11n + 3), n = 1, 2, 3 \cdots \tag{1.42}$$

This Mackay icosahedron is often favored over other structure due to its relatively spherical topology with large number of nearest neighbor contacts. The icosahedron is formed from the packing of 20, each formed from a FCC arrangements of atoms. This ensures that the surface of the icosahedron has the low energy 1,1,1 interface. The interface between the packed tetrahedra form a local HCP place and the edges of the tetrahedra have five fold symmetry extending out from the central atom. However, the tetrahedral subunits do not pack space and this introduces a strain into the icosahedron structure. When the strain energy is too large, the icosahedron becomes unstable. Since the strain energy increase with cluster size, the icosahedron decompose and the decahedron form the global minima structure for cluster with size range of $10^3 - 10^5$. When the cluster size is larger than 10^5, its structure is dominated by FCC packing[47].

The global minimum structure represents the best way to pack the atoms, but higher energy packing arrangements are also possible and the number of these increases exponentially with the number of atoms in the nanoparticle. All the minima for small clusters have been obtained by exhaustively searching the potential energy landscape. The focus of these studies has been on the nature of global structure at the cluster. The local environment of Lenard Jones glassy nanocluster and how they affect the crystallization and glass forming behaviors are also important. Research[90] in a 600 size Lennard-Jones clusters reveals that for single component Lennard-Jones clusters, the energetically favored local structure is the FCC tetrahedral subunits form in the core with a disordered surface. indicating structural inhomogeneity within a cluster. When supercooled, this Lennard-Jones cluster core froze into different size tetrahedral structures with the length having 5, 6, 7 and 8 atoms.

As noted earlier, it is the local structure surrounding an individual atom that is of interest in considering the properties of a glass, rather than the global structure. A recent study of glass forming in a nanoparticle systems, using the Kobb-Andersen binary Lennard Jones mixtures with A-B ratio 80:20, showed that

supercooled nanoparticles can sample the same low energy structures as those found in ultra-stable glasses formed through vapour deposition[59]. In particular, these simulations showed that a particular local structure related to the bicapped squared antiprism played an increasing important role in the glassy structure as the nanoparticle was cooled. This work also suggested that the mobility of atoms at the surface coupled to the particles in the core which allowed them to relax to the low energy inherent structures. Unpublished work by the same authors shows that the supercooled nanoparticles exhibits a fragile-strong crossover as the temperature decreases[59]. It also reveals that T_g increase as $N^{\frac{-2}{3}}$. This research suggest nanoparticle systems could be useful tools for exploring the underlying properties of the glass transition.

1.7 Research Objectives

The goal of my research is to examine the effects of composition on the glass forming properties of Kobb-Andersen binary Lennard Jones clusters. Changing the composition of the cluster can change the nature of the local packing structures that influence the ability of the fluid phase to form crystals or glasses and provide insight to the relationship between local structure and glassy dynamics. The hypothesis for this research is:

1. Composition alters the glassing forming ability of KA binary Lenard Jones clusters.
2. Composition alters the type and distribution of local structures observed in the supercooled and glassy phases of KA binary Lenard Jones clusters.

The main objective will be to map out the phase diagram for binary alloy nanoparticles with a size $N = 600$ as a function of composition and identify the glass forming composition region. This will be achieved by calculating the caloric curves (energy vs temperature at at fixed cooling rate) for the clusters with different compositions and identifying freezing and glass transition temperatures. Average orientational bond order parameters, qA_4, qA_6, D_4, D_6 will be used help identify crystal and glassy structures. The glass forming ability of the clusters, measured in terms of glass transition temperature and inherent structure energies, will be correlated with the presence of local topological cluster types, denoted by their Voronoi index.

Chapter 2

Local Structure in Binary Lennard Jones Nanoparticles

2.1 Introduction

This chapter presents results and discussion of this research with a focus on the local structure analysis of Lennard-Jones nanoparticles with various compositions. The model and methods are described in Section 2.2. Results are shown in Section 2.3 including the thermodynamics of the Lennard-Jones nanoparticles, radial distribution function, density profile, bond orientational order parameters and Voronoi analysis. Lastly, the discussion concerning the research hypothesis, phase diagram, change of local structure with composition and future work are shown in Section 2.4.

2.2 Model and Method

2.2.1 Simulation Model

The system under study is a binary mixture cluster containing $N = 600$ atoms that interact by means of the Lennard-Jones potential:

$$U_{ij}(r) = 4\epsilon_{ij}[((\sigma_{ij}/r)^{12}) - (\sigma_{ij}/r)^{6}], \tag{2.1}$$

where i and j can be either of atom types A or B, ϵ is the well depth and a measure of how strongly the two atoms attract each other, σ is the distance at which the intermolecular potential between the two atoms is zero, so σ is a measurement of how close two non-bonding atoms can approach and is thus referred to as the van-Der-Waals radius. It is equal to one-half of the internuclear distance between non-bonding atoms and r is the distance of separation between both atoms.

The LJ system parameters are $\sigma_{AA} = 1.0$, $\sigma_{BB} = 0.88$, $\sigma_{AB} = 0.8$, $\epsilon_{AA} = 1.0$, $\epsilon_{BB} = 0.5$, $\epsilon_{AB} = 1.5$. The mass of all atoms is set to $m = 1.0$. Reduced units are used with respect to σ_{AA} and ϵ_{AA}/k_B, where k_B is Boltzman constant. The potential is cut off at a distance of $r_c = 2.5\sigma_{AA}$. No interaction is considered for atom pairs beyond this distance. At the cut off distance the potential value is close to zero so the energy of the system is not significantly effected. However, limiting the potential range reduces the number of interactions

that need to be calculated and help speed up the simulation.

Molecular dynamics simulations are performed at different compositions of B atoms with mole fraction $x_B = N_B/(N_A+N_B)$ ranging from 0 to 0.5 in the canonical ensemble using the velocity Verlet algorithm. The time step is $dt = 0.003$, and the unit of time is $\sqrt{(\sigma_{AA}^2 m/\epsilon_{AA})}$. The length of the simulation box containing the 600 atoms is designed to be $15.874011\sigma_{AA}$ for systems with 10% B-type atoms or more. In systems with 0% and 5% B-atoms, a length of $20.874011\sigma_{AA}$ is chosen, in order to sufficiently contain a greater number of large A-type atoms, and thus to prevent interaction across the periodic boundary. The C++ implementation of this Molecular Dynamic Simulation (MD) is derived from a book called *The Art of Molecular Dynamic Simulation*[75].

The temperature is kept constant by velocity scaling, and the unit of temperature is given by k_B/ϵ_{AA}. The supercooled glassy nanoclusters are prepared as follows: the atoms are initially placed on the lattice sites of a square lattice and are assigned random velocity vectors that are then rescaled to ensure a starting temperature of $T = 1.0$. The system is then equilibrated for 200000 time steps before being cooled at a rate of 10^{-6}. At each T, a configuration of the cluster is equilibrated for 200000 time steps. For the equilibrium energy and inherent structure energy calculations, 1000 configurations are sampled, each separated by 100 time steps. For the structural analysis, 200 configurations, each separated by 1000 time steps, are saved to disk for analysis. A total of 10 independent simulations are performed for each cluster composition which gives a total of 2000 configurations that are studied for system. The configurations are quenched to their local inherent structure using the Fire algorithm[73]. The inherent structure quench removes noise due to thermal vibrations around a local free energy minimum and which enhances the structure identification.

2.2.2 Structural Analysis Methods

The CNA method is performed for the pure-A nanocluster, with the neighbor cutoff distance 1.3. Any atom within this distance is considered to be a near neighbor. For each atom in the cluster, $q_{lm}(r)$ for all near neighbors by Eq. 1.33. Local bond order parameter q0 is calculated by Eq. 1.34. In order to improve the accuracy of the distinguishing different structural types, average bond order parameter is also calculated for every atom using Eq. 1.37.

The Voronoi index for this system is generated by the $Voro++$ library[101]. To generate the Voronoi polyhedra for a cluster it is placed within a spherical container with a given radius. The container then acts as one of the walls for the Voronoi polyhedron of the atom on the surface of the cluster. A surface atom is distinguished as a Voronoi polyhedron that has a wall without a corresponding atom, generating a atom $id = -99$. Even though a change in container radius can result in a different Voronoi Cell construction due to cell-overlapped effect, thus changing the identification of surface atoms, this method is used, since the number of surface atoms does not vary significantly with different container radii.

2.3 Results

2.3.1 Thermodynamics of Nanoclusters

Potential Energy of Nanoclusters

Figure 2.1 shows the caloric curve for a system with $x_B = 0.3$, undergoing two different cooling rates. Two linear fits for the liquid line and glass line are shown in the plot to demonstrate how T_g is calculated from the intersection of these two lines. It can be observed that T_g moves from 0.34 to 0.31 as the cooling rate decrease from 3.3×10^{-4} to 3.3×10^{-6}. This feature is consistent with the fact that the slower a cluster is cooled, the more time the system has for sampling all the locally stable minima. As a result, the liquid remains in equilibrium to a lower temperature.

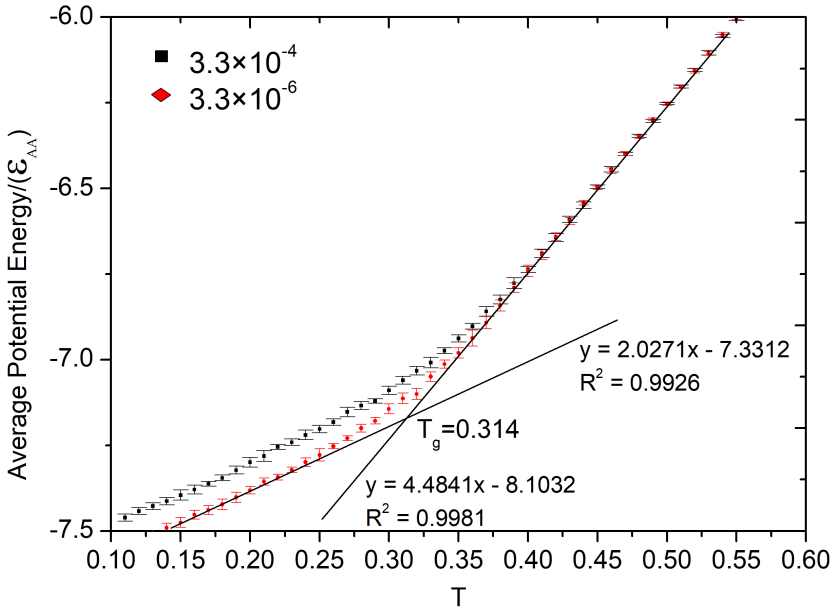

Figure 2.1: Potential energy as a function of temperature for a $x_B = 0.3$ nanocluster system , with cooling rate marked. The intersection of two linear fittings shows the calculation of T_g.

Caloric curves of the nanocluster system with increasing B-atom composition are shown in Fig 2.2. The average potential energy per atom ϵ is plotted at different temperatures during the cooling process. The B-atom composition is indicated by the numbers on the curves. In these calculations, configurations are generated from Molecular Dynamic simulations. Each state point is averaged over 1000 configurations during the equilibrum process obtained from 10 independent simulations runs. The error bars represent the standard deviation of the data. A general trend of lowering energies per atom as x_B increase is observed. This is the result of the increasing number of energetically favourable A-B interactions that occur with increasing x_B.

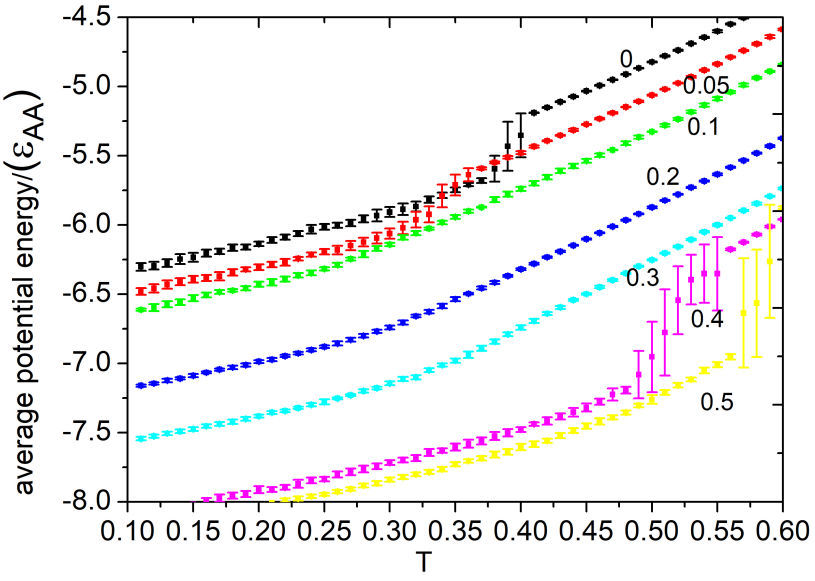

Figure 2.2: Cluster freezing and glass transition potential energy per particle as a function of temperature. The numbers on each line indicate the B-type particle fraction. In all data, error bars indicate standard deviation of the data for ten independent runs.

All systems exhibit a high temperature liquid droplet regime. A sharp decrease in the potential energy, along with large fluctuations, are characteristic of freezing to a crystalline type structure. The large fluctuation in energy in the transition region occurs because nucleation to an ordered state is a stochastic process. Above the transition region, all the clusters are liquid with a high energy. Once the clusters become metastable, a fraction of the clusters freeze on the time scale of the simulation so the energy calculation is averaged over high and low energy configurations. As the temperature is lowered, the driving force for nucleation increases, so a greater number of the clusters freeze on the simulation time scale. Eventually the temperature is low enough that all clusters are solid so the energy fluctuations become small again. In the case of $x_B = 0$, it is known to freeze to icosahedral/decahedral type structures[90]. These are formally non-crystalline global structures, but the atoms exhibit highly ordered environments of varous types. Figure 2.2 suggests compositions $x_B = 0, 0.05, 0.4, 0.5$ all freeze. A smooth transition located by slopes is indicative of a glass transition. Fig 2.2 suggests that glass transition are observed for the nanoclusters with $x_B = 0.1, 0.2, 0.3$. T_g, obtained by the intersection of linear fit of liquid curve and glassy portion curve, have values of $T_g = 0.28$, 0.30 and 0.32 respectively for the three glassy systems.

Inherent Structure Energy

The inherent structure energy diagram shown in Fig. 2.3 can be used to distinguish between crystallization and a glass transition. Each state point is averaged over 1000 configurations during equilibrium. We have 10 independent simulation runs, with error bars represent the standard deviation of these independent runs.

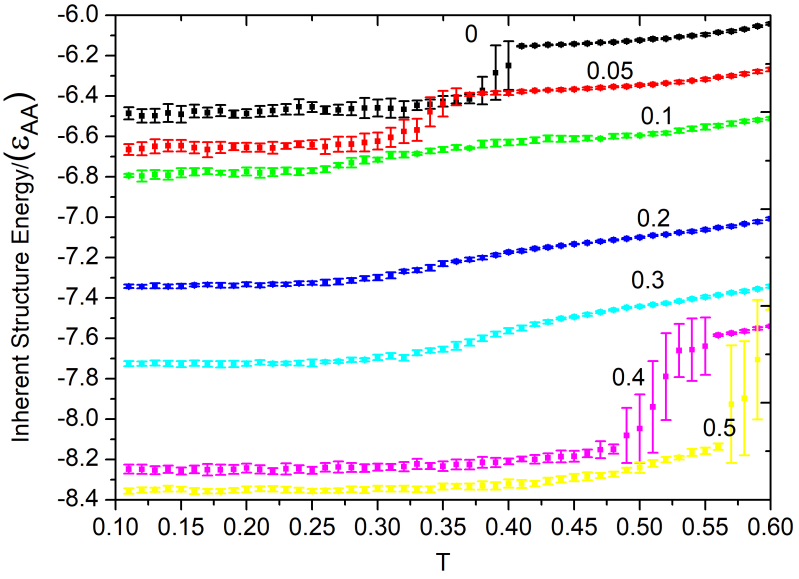

Figure 2.3: Inherent Structure Energy per atom (EIS) for different B-type fraction as a function of temperature. EIS decreases with increase of B-type fraction, as the system sample lower energy landscape.

A sharp decrease in inherent structure energy with large fluctuations can be observed in $x_B = 0.0, 0.05, 0.4$ and 0.5 nanoclusters. These are the features of freezing to crystalline type structure. A glass transition occurs for the systems with $x_B = 0.1, 0.2, 0.3$, which show a smooth curve when undergoing the phase transition. The $x_B = 0.3$ system seems to be the best glass former, since it had a comparatively lower inherent structure energy due to more A-B interaction. As the B-type fraction in this LJ nanocluster system increases, the inherent structure energy becomes lower, suggesting a more stable energy landscape is sampled.

At high temperature in the liquid state, the inherent structure energy decreases slowly as the temperature decreases in comparison to the potential energy shown in Fig. 2.2. The system has enough energy and a low density making it possible for the cluster to sample all possible minima on the potential energy landscape. As the temperature decreases, the system moves to deeper, low energy basins to stay in equilibrium.

Once the temperature is reduced below T_g, the inherent structure energy is low and it is temperature-independent. That is, at this point, the nanocluster system is trapped in a deep minima because the system does not have enough energy to reorganize the atoms and cross the energy barriers between different basins.

2.3.2 Radial Distribution Function

The radial distribution function is calculated in order to investigate the binary Lenard Jones nanolcluster configurations collected during the equilibrium. The radial distribution function, $g(r)$ which was described in Section 1.4.1, is determined by calculating the distance between all particle pairs and binning them into

histograms with a width of $0.25\sigma_{AA}$. The histogram is then normalized with respect to the distribution of an ideal gas, where particle histograms are completely uncorrelated. The radial distribution of $x_B = 0.3$ and 0.4 nanoclusters are shown in Fig. 2.4 and Fig. 2.5. The radial distribution for pure A, $x_B = 0.1$ and 0.2 nanoclusters are included in Appendix A.

The first peak in the radial distribution function locates the position of atoms in the first shell that are possible for caging an atom. These are usually large, even in the liquid state, and are usually just above the σ_{AB} distances defined in the potential indicating the atoms are siting in the potential minimum. The $g(r)_{AB}$ peak, located at $r = 0.83$, is the largest peak because this is the strongest interaction, followed by the $g(r)_{AA}$ peak. The first peak in $g(r)_{BB}$ is the smallest because it is a weak interaction and there are less B atoms at these mixture compositions. The $g(r)$ of these two cluster goes to zero at distances above $r = 2.8$ because of the finite size of the cluster. The lack of sharp peaks at longer distances in Fig. 2.4 suggests that the system become more and more similar to ideal gas as r increases. The appearance of minima is caused by exclusion between different atom layers.

The radial distribution functions above and below the transition temperature for $x_B = 0.3$ shown in Fig. 2.4 are similar suggesting the cluster remains amorphous, that is, it is a glass. Strong peaks shown in Figure 2.5(b) compared with Figure 2.5(a) indicate the structural order that appears below the transition for the $x_B = 0.4$ nanocluseter. The $g(r)_{AA}$ peaks overlap totally with $g(r)_{BB}$ peaks, but $g(r)_{AB}$ presents different peak position than $g(r)_{AA}$. The peak overlap of $g(r)_{AA}$ and $g(r)_{BB}$ suggests that the A atoms alone form the same structure as B atoms alone. This structure formed by A atoms are interlocked with the one formed by B atoms, resulting a second different structure composed of A-B atoms. This is consistent with the formation of CsCl-type crystal structure.

2.3.3 Density Profile

To investigate how A and B atoms are distributed in this system, the density profile and composition distribution are calculated for $x_B = 0.1, 0.2, 0.3$ and 0.4 nanocluster systems. (See Fig 2.6, Fig 2.7, Fig 2.8, Fig 2.9 respectively). All (a) figures plot $\rho = N(R)/V(R)$ where $N(R)$ is the number of atoms in a shell with a volume $V(R)$ and a shell thickness $0.25\sigma_{AA}$, located at a radius R from the mass center of the cluster. All (b) figures plot the probability of finding a small B atom within the same shell obtained from

$$P(N_b) = \frac{N_b(R)}{N_(R)}.$$

The configurations selected are at a temperature around 0.8 of the phase transition temperature. The remarkable density fluctuation around the cluster core, shown by elongated error bars, reflects the reduced number of atoms in the volume of the center core, but it is also due to the effect of the atomic layering effect caused by the volume exclusion of the atoms. From all of the density plots, we observe that the number density decays to zero around $6.0\sigma_{AA}$, which is the distance from the surface to cluster core. An obvious difference is that, density for $x_B = 0.1$ system decays more smoothly than the other two clusters. All the

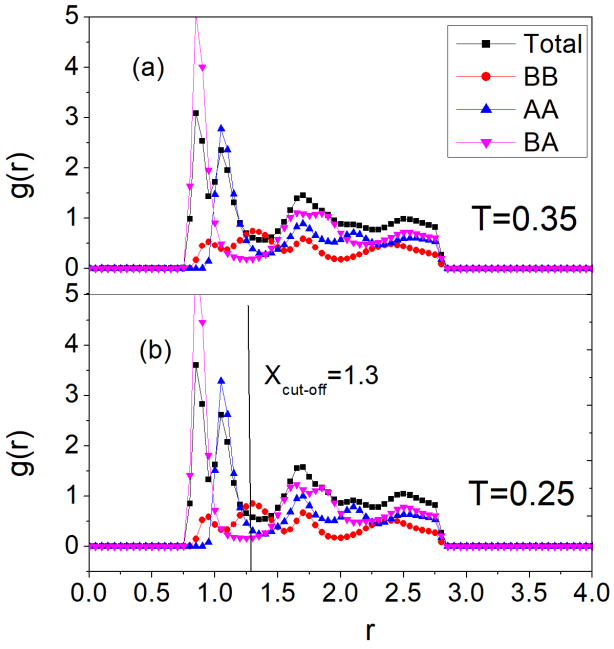

Figure 2.4: Radial Distribution for $x_B = 0.3$ nanocluster. Figure(a) shows the $g(r)$ of liquid state at high temperature. Figure(b) shows the $g(r)$ of glassy state at low temperature.

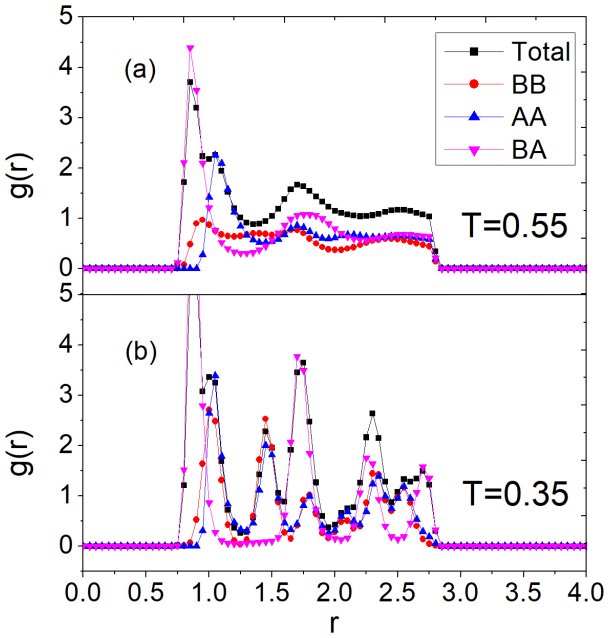

Figure 2.5: Radial Distribution for $x_B = 0.4$ nanocluster. Figure(a) shows the $g(r)$ of liquid state at high temperature. Figure(b) shows the $g(r)$ of crystal state at low temperature.

density profiles have a value of 1.5ρ at a distance of 0.5-4σ_{AA}, this indicates that the general density of the nanoclusters is 1.5ρ. The surface region of the cluster occurs in the range of $4 - 6\sigma_{AA}$.

For all the systems studied, the probability of finding a B atom in the core is higher than expected based on the cluster stoichiometry, which also means the surface is enriched with A atoms. This occurs because the system lowers its energy the most by maximizing the number of AB interactions. The effect is most apparent in the $x_B = 0.1$ nanocluster, where B atom probability decays at a distance around 2.0σ, very close to the center. But the density of $x_B = 0.1$ nanocluster decays at 4.0σ. At this distance, the B atoms probability already goes to zero. The $x_B = 0.1$ and 0.2 nanoclusters show similar features. The B atoms probability near the center of the nanocluster is always larger than the cluster stoichiometry, indicating the core enrichment of B atoms in the glassy nanoclusters. For example, in $x_B = 0.3$ nanoclusters, the B atoms probability near the center is approximately 0.4, which is significantly larger than 0.3. Even in the $x_B = 0.4$ nanoclusters, the B atoms probability near the center is 0.5, larger than the 0.4 stoichiometry. In fact, the 0.5 stoichiometry is consistent with the later structural demonstration that $x_B = 0.4$ nanocluster forms a CsCl type crystal. At a distance of $R = 1.0$, the B atom probability is 0.35 for the 3 glassy systems: $x_B = 0.1, 0.2, 0.3$. This stoichiometry is consistent with that of bicapped square anti-prism, with Voronoi index 0 2 8 0.

2.3.4 Structural Analysis of Nanoclusters Using Bond Orientational Order/Disorder Parameters

Figures 2.10a 2.10b, Fig. 2.11a 2.11b and Fig. 2.12a 2.12b show the probability distributions for the orientational bond order parameters, $q0(i)_l, qA(i)_l$ and $D(i)_l$, given by Eqs. 1.34, 1.38 and 1.40 respectively, with $l = 3, 4, 6$ and 8, for the pure A nanoclusters above and below the freezing transition temperature. Figure 2.10a shows that the local bond order parameter distributions functions exhibit sharp peaks in the solid phase indicating the presence of different but well defined local structures around an atom. In the liquid phase the distributions become more Gaussian like, which is consistent with the broader range of local structures. The average bond order parameters and disorder parameters in the solid phase (Figs. 2.11a and 2.12a) still show some peak structure, but this is reduced because these functions include information from the second neighbour shell which leads to some randomization of the order parameter.

By comparing the $q0(i)_l$ distribution and the $qA(i)_l$ distribution in Fig. 2.10a 2.10b, and Fig. 2.11a 2.11b, it is possible to observe a reduced overlap between the liquid state and crystal state for the $qA(i)_l$ order parameter, making it easier to distinguish liquid and solid state. Because of this, $qA(i)_l$ is chosen instead of $q0(i)_l$ for constructing order parameter plane $qA(i)_4$-$qA(i)_6$ in the later section to analyze local structure of the nanoclusters. In the $qA(i)_l$ distribution for pure A nanoclusters, $qA(i)_6$ has the greatest distinction between crystal and liquid state compared with $l = 3, 4$ and 8. And then $l = 8$ has a better distinction compared with $l = 3, 4$. However, the the $l = 4$ order parameters have been used previously in the literature[91].

A full set of distribution functions were calculated for all order parameters and all nanoparticle stoi-

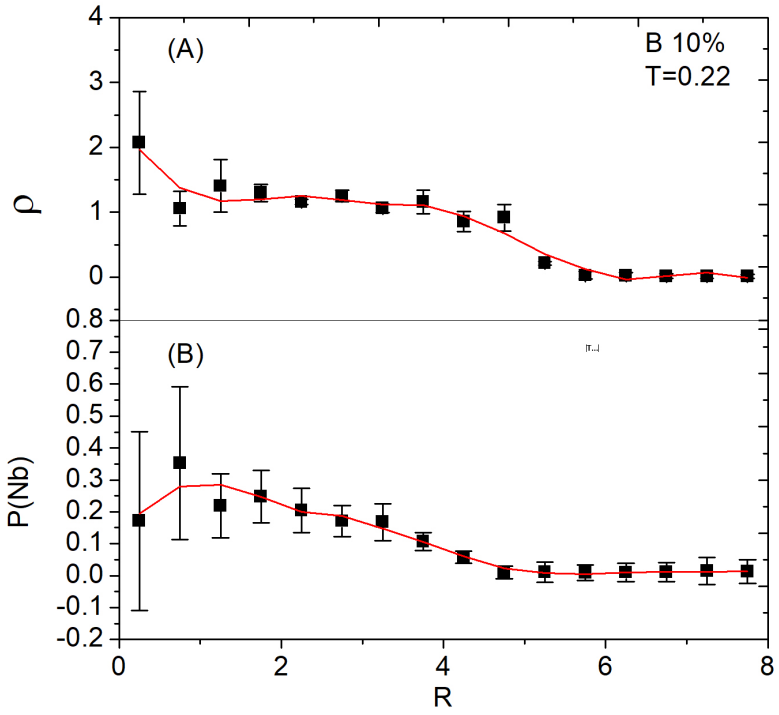

Figure 2.6: (a), The density and (b), the fraction of B atoms as a function of radius from the center of the $x_B = 0.1$ nanocluster.

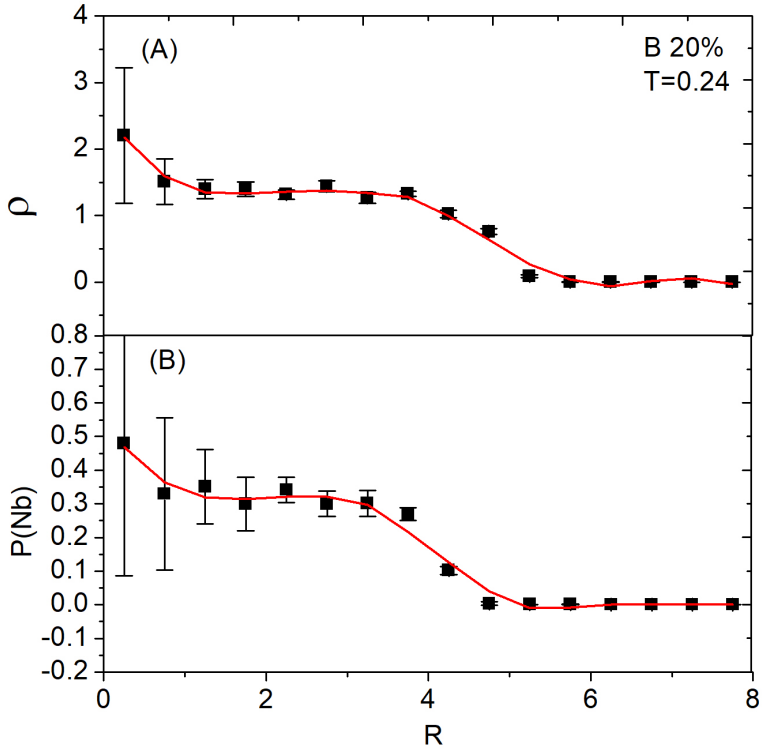

Figure 2.7: (a), The density and (b), the fraction of B atoms as a function of radius from the center of the $x_B = 0.2$ nanocluster.

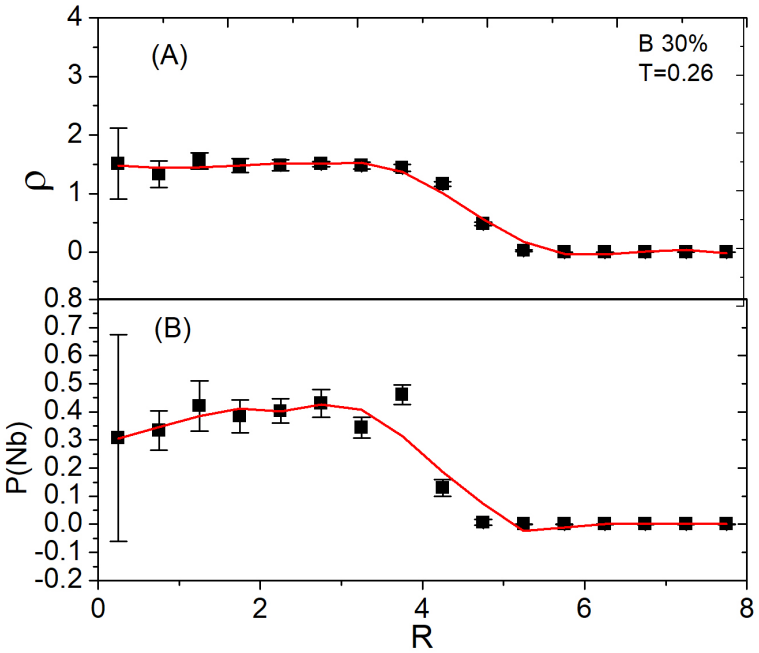

Figure 2.8: (a), The density and (b), the fraction of B atoms as a function of radius from the center of the $x_B = 0.3$ nanocluster.

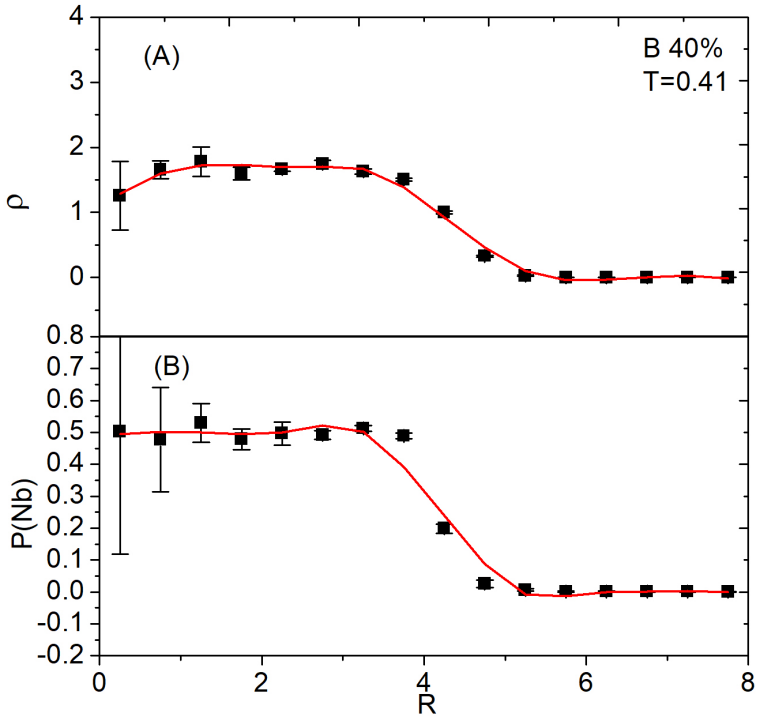

Figure 2.9: (a), The density and (b), the fraction of B atoms as a function of radius from the center of the $x_B = 0.4$ nanocluster. .

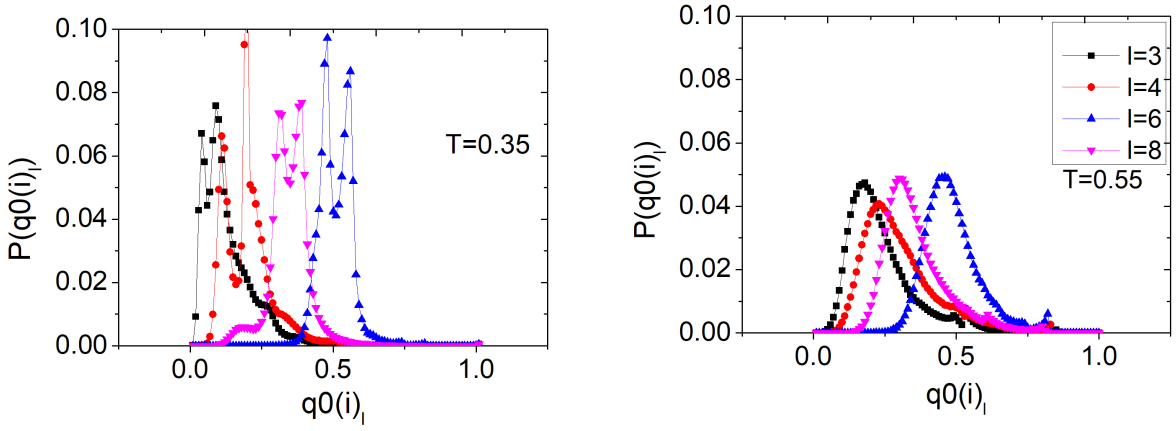

(a) (b)

Figure 2.10: Distribution of local order parameters with different symmetry index l, for pure A nanocluster at high and low temperature.

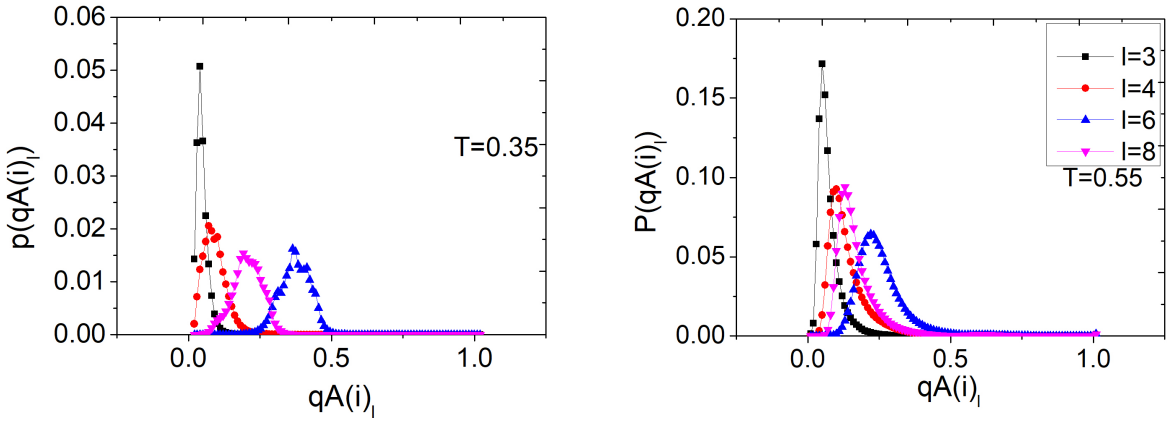

(a) d **(b)** d

Figure 2.11: Distribution of average local order parameters with different symmetry index l, for pure A nanocluster at high and low temperature.

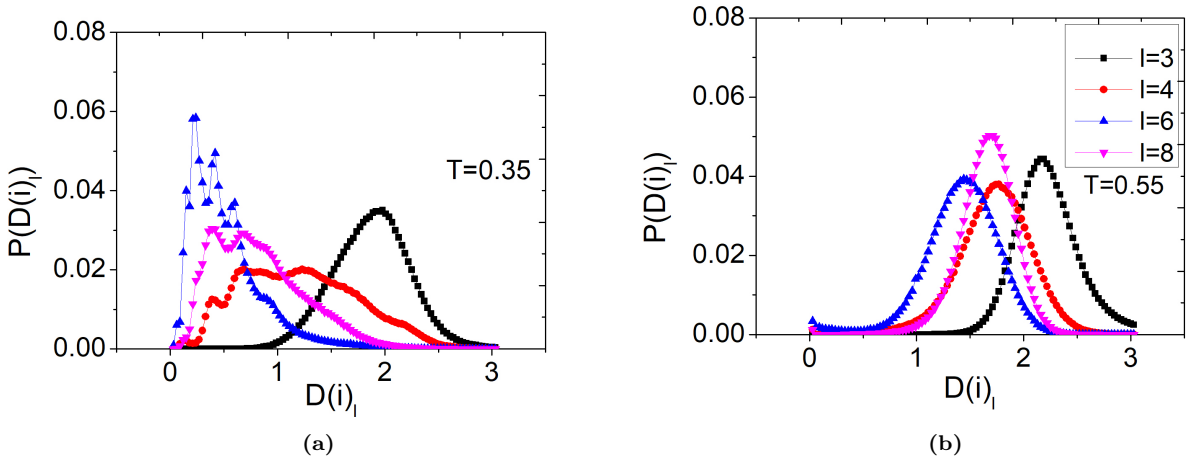

Figure 2.12: Distribution of disorder parameters with different symmetry index l, for pure A nanocluster at high and low temperature.

chiometries. However, in describing the structural properties of the mixed clusters, only those distributions that contain important features are discussed in the main text. The remaining plots can be found in Appendix A.

Figure 2.13a and Figure 2.13b show the disorder parameter distribution for the $x_B = 0.1$ nanoclusters at a high temperature above the glass transition temperature, and a low temperature below the glass transition temperature, respectively. The disorder parameter distributions above and below the transition temperature for this cluster are similar, suggesting the cluster remains amorphous. However, the $D(i)_6$ distribution exhibits a small shoulders at small values of $D(i)_6$, and this is may be an indication of partially crystallization, even though the potential energy plot in Fig. 2.2 suggests that $x_B = 0.1$ nanocluster forms a glass at low temperature.

In order to understand how the atoms with small $D(i)_6$ are spatially distributed in the $x_B = 0.1$ cluster, a number density distribution is plotted in Fig. 2.14, which shows the number density as a function of radius from the center of the cluster. The number density is calculated by finding the number of atoms with $D(i)_6 < 1$ in a shell with width $0.25\sigma_{AA}$, and then divided by the volume of the shell:

$$P = \frac{N(D(i)_6 < 1)}{V(R)}. \tag{2.2}$$

Every data point represents the average number density from 10 configurations chosen from 10 independent runs. The error bars are the standard deviation of the 10 values. From this graph, the number density distribution of small $D(i)_6$ atoms has zero value in the core, suggesting that core atoms are comparatively disordered. P begins to increase at $r = 1.2$, and reaches a maximum $P = 0.28$ at $r = 4.8$, which is very close to the surface. At $r = 5.5$ P becomes zero since $r = 5.5$ is the finite size of the cluster.

In these 10 configurations containing 6000 atoms, 1179 atoms have $D(i)_6 < 1.0$, and 1178 out of 1179 of them are A atoms. This number tells us that it is the A atoms that present small disorder in $x_B = 0.1$

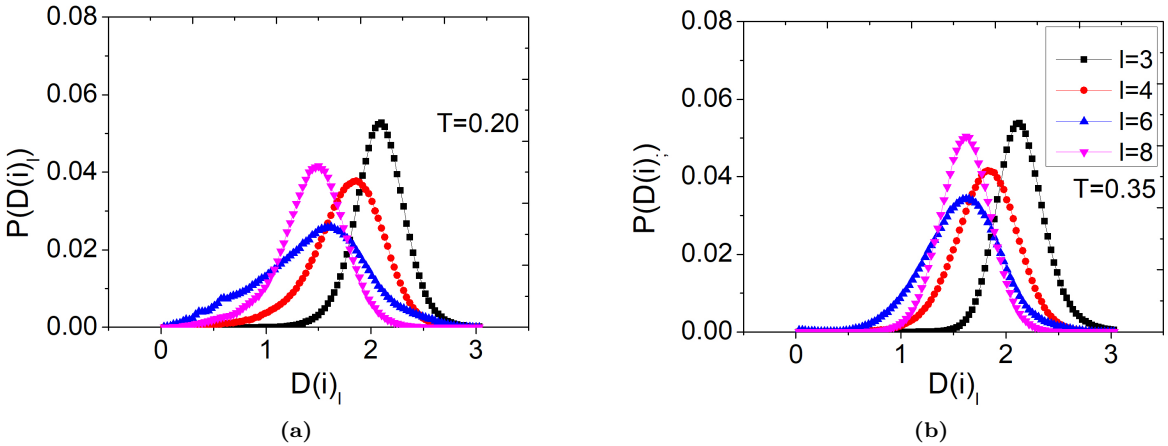

Figure 2.13: Distribution of disorder parameters with different symmetry index l, for $x_B = 0.1$ nanocluster at high and low temperature.

nanocluster.

Figure 2.15a and Figure 2.15b show the average order parameter distribution for $x_B = 0.2$ nanoclusters at high temperature, above the glass transition temperature, and low temperature below the glass transition temperature respectively. It can be seen that the liquid and the glass have similar $qA(i)_l$ distributions with close peak values and similar shape. Both liquid and glass $qA(i)_l$ distributions exhibit peaks in the small $qA(i)_l$ value region below 0.25. This feature indicates that liquid and glass have similar local structural environment. The distribution functions for the $x_B = 0.3$ are similar again supporting the identification of these nanoclusters as being glasses.

Figure 2.16a and Figure 2.16b show the average order parameter distribution for the $x_B = 0.4$ nanoclusters at a high temperature above crystallization temperature, and a low temperature below crystallization temperature. It can be seen that at high temperature, $T = 0.55$, the $qA(i)_l$ distributions for this nanocluster exhibit peaks at small $qA(i)_l$ value region below 0.25, consistent with the liquid state seen for $x_B = 0.2$ system. As the temperature decreases to $T = 0.35$, $qA(i)_6$ distribution shows multiple peaks close to $qA(i)_6 = 0.4$, suggesting that more than one local structures is present in this $x_B = 0.4$ nanocluster. This feature is consistent with the structural feature demonstrated in the radial distribution function $g(r)$, which shows that the A type atoms alone form the same structure as that constructed by the B type atoms alone. But A and B atoms together forms a completely different structure with A and B atoms interlocking with each other. The $l = 8$ average order parameter distribution shows a similar behaviour. Other order/disorder parameters distribution are included in the Appendix A for reference.

In order to understand the disorder level of the three glassy nanoclusters and their nearby crystal structure, a phase diagram at low temperature $T = 0.11$ is plotted in Fig. 2.17. This shows the overall disorder parameter average taken from 2000 configurations for $x_B = 0, 0.1, 0.2, 0.3, 0.33, 0.35, 0.4$ nanoclusters. The error bars indicate the standard deviation of these configurations. In Fig. 2.17, the average disorder param-

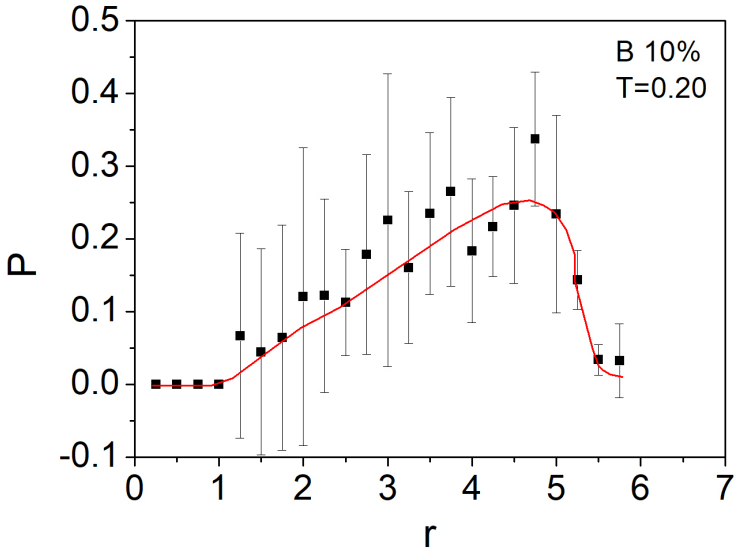

Figure 2.14: The number density of atoms with $D(i)_6 < 1.0$, as a function of radius from the center of the $x_B = 0.1$ nanocluster. Red line is a guide to the eye. B composition and temperature are shown in the graph.

eter $< D >_6$ in Eq. 1.41 as a function of composition is given. In $x_B = 0$, and 0.4 clusters, the disorder parameters $< D >_6$ at T=0.11 are below 0.5, which supports by the observation that $x_B = 0$, and 0.4 clusters crystallize upon cooling. In contrast, the $x_B = 0.1, 0.2$ and 0.3 nanoclusters have disorder parameters above 1.0, indicating of the amorphous glassy state.

In the $x_B = 0.1, 0.2, 0.3$ nanoclusters, $< D >_6$ increase as x_B increase. Since the disorder of $x_B = 0.4$ cluster is sharply reduced, to help locate the maximum, the disorder parameter for $x_B = 0.33, 0.35$ clusters are calculated. The results show that the $< D >_6$ of these two systems is smaller than that of $x_B = 0.3$. The $< D >_6$ for $x_B = 0.33$ nanocluster is 1.7, indicating a highly amorphous structure. When $x_B = 0.35$, the disorder parameter becomes 0.7, a comparatively small value. The error bars of the average $< D >_6$ calculated from configurations during equilibrium indicate the structural homogeneity of the cluster. The $x_B = 0.2, 0.3$ nanoclusters have very small error bars, while the $x_B = 0.1$ system shows a comparatively large error bars. The reason for this fluctuation can be accounted by the partial ordering observed in the $x_B = 0.1$ system.

2.3.5 Temperature Dependence of Orientational Bond Order/Disorder Parameters

As previously mentioned, different peak positions in the $qA(i)_6$ distributions indicates structurally different phases at high and low temperature. While the crystal and liquid have very different peak positions, the glass and liquid have very similar distribution with a large overlap, since the glass is amorphous. In order

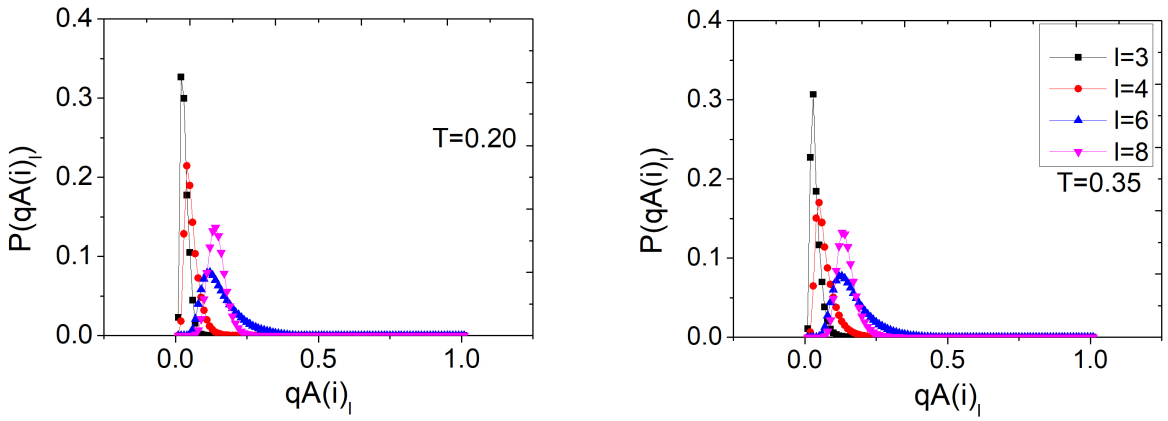

Figure 2.15: Distribution of average local order parameters with different symmetry index l, for $x_B = 0.2$ nanocluster at high and low temperature.

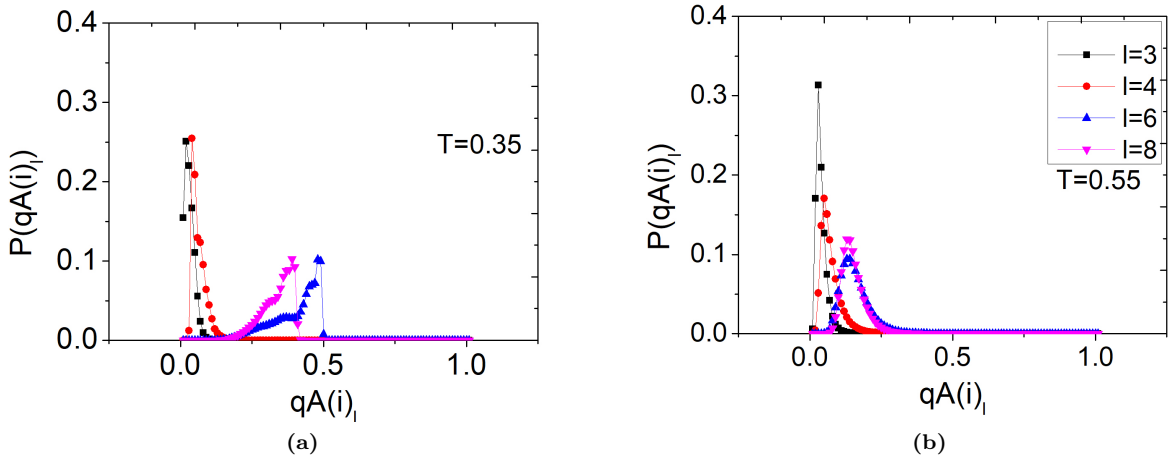

Figure 2.16: Distribution of average local order parameters with different symmetry index l, for $x_B = 0.4$ nanocluster at high and low temperature.

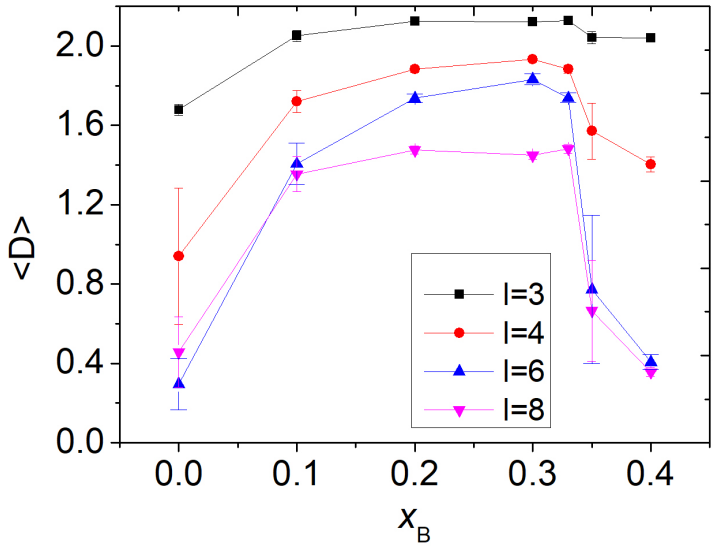

Figure 2.17: Disorder parameters $< D >_l$ with $l = 3, 4, 6, 8$ for $x_B = 0, 0.1, 0.2, 0.3, 0.33, 0.35$ and 0.4 nanoclusters. Every point represents average value from 2000 configurations collected in the equilibrium process. The error bar shows the standard deviation of these 2000 configurations.

to understand how structure varies within a continuous temperature range, the ensemble averages of the order/disorder parameters are plotted as a function of temperature.

Figure 2.18 shows the overall average order parameter qA_6, which is the average of $qA(i)_6$ over all 600 atoms in a configuration, as a function of temperature. Every data point is the average value over 2000 configurations of the same temperature, with error bars showing the standard deviation of the 2000 values. Different B atom fractions are indicated by different colors. At high temperature, where all the clusters are in the liquid state, qA_6 decrease as the B atoms fraction increase. Also in the liquid state, qA_6 decrease slightly as temperature decrease.

For the pure A nanocluster, the qA_6 has a value around 0.5 in the liquid state, and it suddenly increases at the temperature where crystallization occurs. At low T, qA_6 increases slightly as T decreases, suggesting a more ordered structure, and a larger extent of crystallization. Also at low temperature region, large error bars are observed, which is the evidence of structural heterogeneity of pure A crystal. This feature supports the previous results that pure A nanocluster forms different size FCC, HCP and ICO structures[90].

For the $x_B = 0.4$ nanocluster, qA_6 has value around 0.35 in the liquid state, and it has an abrupt increase to 0.45 at the temperature around $T = 0.51$ where crystallization occurs. At low T, qA_6 increases slightly as temperature decreases, indicative of a more crystalline state. The error bar is very small compared with that of the pure A crystal former, suggesting a homogeneous crystal structure. For the three glass forming nanoclusters with $x_B = 0.1, 0.2$ and 0.3 there is no abrupt increase at the glass transition temperature in the $qA_6 - T$ curves. At the low temperature below glassy transition, qA_6 decreases very slightly as T decreases.

The qA_4, the average local parameter with is also plotted as a function of temperature in Fig. 2.19

with different B atom fraction indicated by different color. At high temperature, where all the clusters are in the liquid state, qA_4 decreases as the B atom fraction increases. Also in the liquid state, qA_4 shows obvious decrease as temperature decreases. For the pure A nanocluster, qA_4 has a value around 0.18 in the crystal state, and it continues to decrease as T decrease. The error bars again indicate its structural heterogeneity. The qA_4 of the $x_B = 0.4$ nanocluster shows a large decrease at its melting point $T = 0.51$. At low temperature, its qA_4 is very small, around 0.12, and does not change much when T decreases. For the $x_B = 0.1, 0.2$ and 0.3 nanoclusters, there is no abrupt decrease at the phase transition temperature. In the glassy state, their qA_4 decrease very slightly as T decreases and they have similar values around 0.15.

In order to better understand the temperature dependence of the order parameters and how they are connected to the local structure of the nanocluster, the $qA_8 - T$ curves for the four nanoclusters are also plotted in Fig. 2.20. The data point shows the ensemble average of qA_8 from 2000 configurations, with error bars demonstrating the fluctuation. In the liquid state at high T, the qA_8 decreases as T decreases. And it can be seen that in the liquid state the qA_8 is small when the B atom fraction is large. The $x_B = 0.4$ nanocluster has a qA_8 around 0.35 in the liquid state, and shows an abrupt increase to 0.40 at its phase transition temperature $T = 0.51$. Similar feature were seen in the pure A nanocluster, which has a qA_8 around 0.38 in the liquid state, first decreases to 0.32 when cooled down, and then shows an increase to 0.35 at its phase transition temperature $T = 0.41$.

At low T, the qA_8 of the $x_B = 0.4$ nanocluster is much larger than that of the pure A system. This feature is different from the $qA_6 - T$ and $qA_4 - T$ plots, which show that the qA_6 and qA_4 of the the $x_B = 0.4$ nanocluster is much smaller than that of the pure A system. The large error bars in the pure A nanocluster again show the structural heterogeneity of this system. The three glassy nanoclusters with $x_B = 0.1, 0.2$ and 0.3 show decreasing qA_8 as T decreases in the liquid state. They do not exhibit an increase of qA_8 during the glass transition. Instead, they continue to decrease but at a slower rate. In contrast to the $qA_6 - T$ and $qA_4 - T$ plots where clusters with large fraction of B atoms have smaller qA_6 and qA_4 at the same temperature, $qA_8 - T$ shows that clusters with large fraction of B atoms have larger qA_8 at the same temperature. This feature suggests that more A-B interactions increase the value of qA_8.

The temperature dependence of $q0_6$ is plotted in Fig. 2.21. Compared with the temperature dependence of qA_6, the $q0_6$ has a smaller value than qA_6 at the same temperature for the same B atom fraction. But there is a larger increase at the local order parameter at the crystallization temperatures. Figure 2.21 showing $q0_6 - T$ also suggests that in the liquid state, $q0_6$ decreases as T decreases, while in the crystal $q0_6$ increases as T decreases.

The $q0_6$ of the $x_B = 0.1, 0.2$ and 0.3 nanoclusters in the liquid state are very close compared with the difference of their qA_6 values. At low temperature below the glass transition, the $q0_6$ of the $x_B = 0.1$ nanocluster increases as T decreases. Obvious error bars also appear while the $qA_6 - T$ plot does not show error bars. This highlights the additional sensitivity of $q0_6$ to the local structure. It also suggests that while $x_B = 0.1$ nanocluster appears to exhibit glass transition at low temperature according to the potential energy

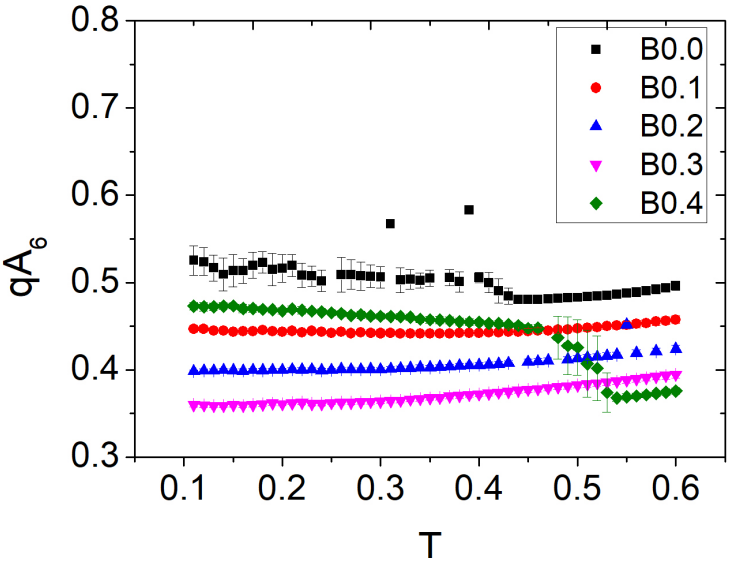

Figure 2.18: Average order parameter with $l = 6$ at different temperature. Every point represents the average value from 2000 configurations collected in the equilibrium process. The error bar shows the standard deviation of these 2000 configurations.

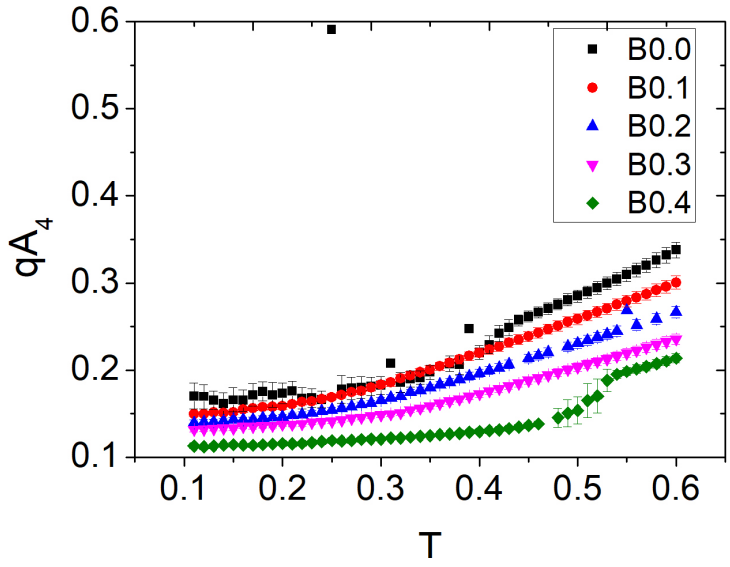

Figure 2.19: Average order parameter with $l = 4$ at different temperature. Every point represents the average value from 2000 configurations collected in the equilibrium process. The error bar shows the standard deviation of these 2000 configurations.

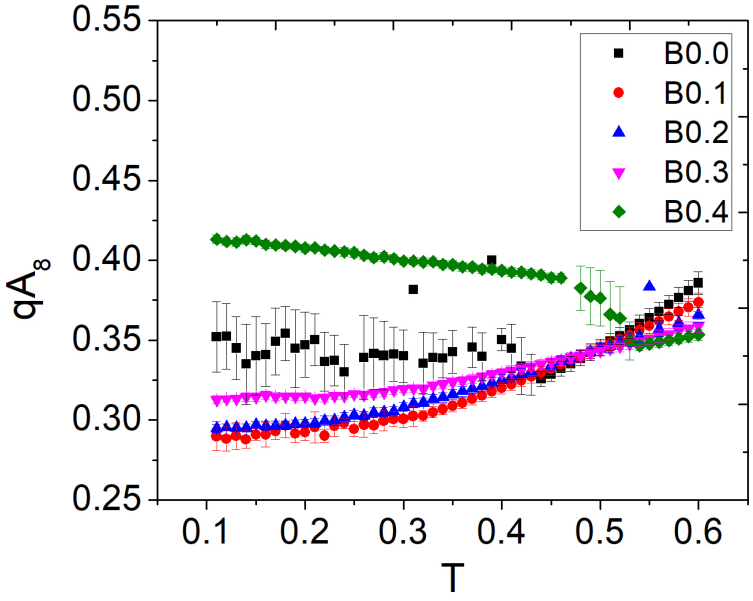

Figure 2.20: Average order parameter with $l = 8$ at different temperature. Every point represents the average value from 2000 configurations collected in the equilibrium process. The error bar shows the standard deviation of these 2000 configurations.

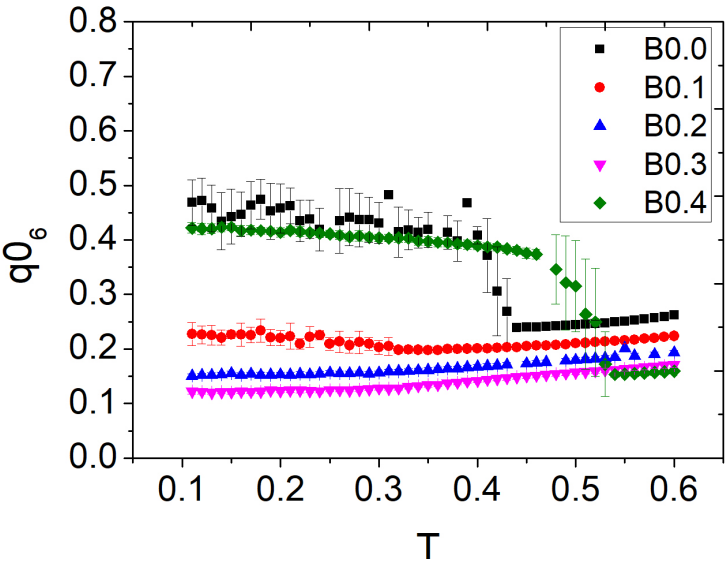

Figure 2.21: Local order parameter with $l = 6$ at different temperature. Every point represents the average value from 2000 configurations collected in the equilibrium process. The error bar shows the standard deviation of these 2000 configurations.

(see Fig. 2.2), there is a degree of local ordering.

The temperature dependence of the disorder parameter $< D >_6$ is plotted for the $x_B = 0, 0.1, 0.2, 0.3$ and 0.4 nanoclusters in Fig. 2.22. In the high temperature region the $< D >_6$ of the four cluster compositions are very similar and decreases slightly as temperature decreases in the liquid. The $< D >_6$ of the pure A nanocluser shows an abrupt decrease at its phase transition temperature $T = 0.41$. In the low temperature region, the $< D >_6$ decrease as T decreases, indicating a less disordered structure. The large error bars again indicate structural heterogeneity of the pure A nanocluster crystals. The $< D >_6$ of the $x_B = 0.4$ nanocluster also shows a huge decrease at $T = 0.53$. In the low temperature region, its $< D >_6$ decreases as T decreases, indicating a less disordered structure. But small error bars suggest a structural homogeneity for this crystal. For the $x_B = 0.2$ and 0.3 nanoclusters, there is no abrupt change in their $< D >_6 - T$ curves. At low T in the glassy state, $< D >_6$ increases very slightly as T decreases. In the $x_B = 0.1$ nanocluster at low temperature region, its $< D >_6$ is around 1.5, typically a large value indicating a glassy state. However, this $< D >_6$ decreases as T decreases in the low temperature region, with error bars indicating structural heterogeneity. This feature again supports that, while the $x_B = 0.1$ nanocluster generally forms a glass, some fraction of the atoms have a highly ordered local environment.

The global order parameter, which is determined by Eq. 1.36, measures the global order of the nanocluster. The temperature dependence of Q_6 is also plotted in Fig. 2.23. Every data point is the ensemble average of Q_6 taken over 2000 configurations, with error bars indicating the structural fluctuation and different colors for different B atom fractions. The inset graph shows the same plot but exhibit an enlarged Q_6 scale in order to see the changes of Q_6 with small values. Interestingly, in the liquid state, the Q_6 increase as T decreases for the pure A and the $x_B = 0.1$ nanoclusters. This increasing of order parameter as T decreases is not seen in the $q0_6 - T$, $qA_6 - T$, $qA_4 - T$ and $qA_8 - T$ plots. For the pure A cluster, a large increase of Q_6 to around 0.25 occurs at the crystallization temperature $T = 0.41$. The extremely large error bars suggest the structural heterogeneity of this system. It also suggest that the Q_6 is very sensitive to the structure difference between FCC, HCP and ICO. The $x_B = 0.4$ nanocluster also shows an abrupt incease of Q_6 to around 0.40 at $T = 0.51$. The very small error bars indicate that its crystal structure is perfectly homogeneous.

For the $x_B = 0.1$ nanocluster, the Q_6 increases as T decreases at low temperature, showing appreciable error bars. These features may suggest that the $x_B = 0.1$ nanocluster has some fraction of freezing atoms, even though it formed a glass at low T as supported by the small Q_6 values. For the $x_B = 0.2$ and 0.3 nanoclusters, Q_6 is stable in the liquid state. As T decreases, their Q_6 decreases slightly at the glass transition temperature. In the glass state, their Q_6 remains stable again as shown in the inset graph. For the three glassy clusters, the Q_6 decreases as the fraction of B atoms increases, indicating a less ordered structure with more A-B interactions.

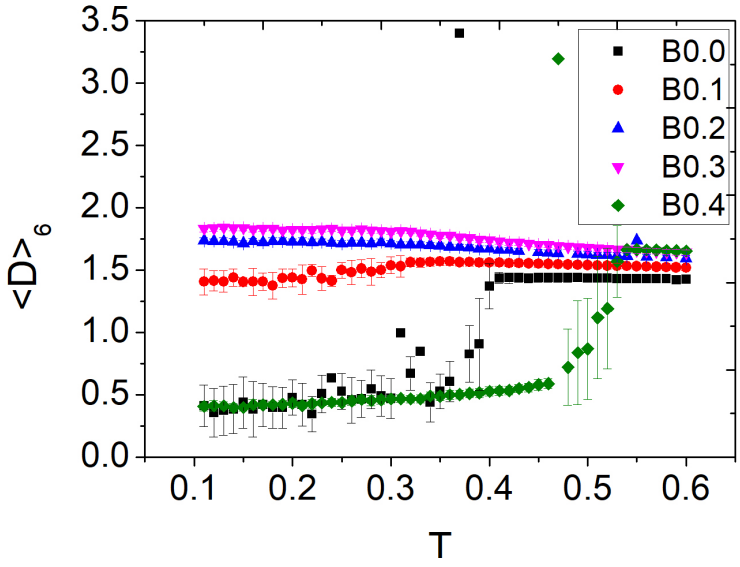

Figure 2.22: Disorder parameter with $l = 6$ at different temperature. Every point represents the average value from 2000 configurations collected in the equilibrium process. The error bar shows the standard deviation of these 2000 configurations.

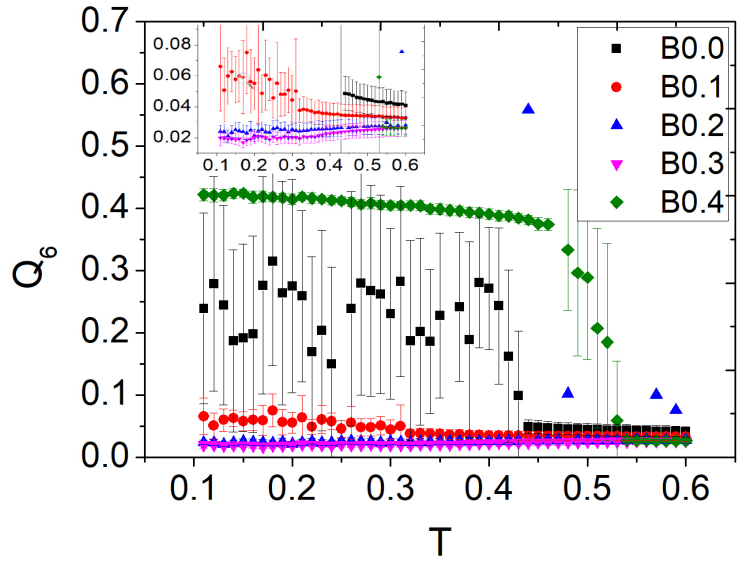

Figure 2.23: Global order parameter with $l = 6$ at different temperature. Every point represents the average value from 2000 configurations collected in the equilibrium process. The error bar shows the standard deviation of these 2000 configurations. Insert shows an expanded view of the low Q_6 region.

2.3.6 $qA(i)_4$-$qA(i)_6$ Plots for Lenard Jones Nanoclusters

$qA(i)_4$-$qA(i)_6$ planes are constructed for binary Lennard Jones nanoclusters with different B atom fractions in order to further investigate their local structures. Figure 2.24 shows the $qA(i)_4$-$qA(i)_6$ plane for a single pure A nanocluster configuration, with different colors indicating an atom's structural identity determined by Common Neighbor Analysis (CNA). From this figure, it can be seen that the CNA non-identified atoms (NON), colored in green, appear evenly distributed over the order parameter space, along with the FCC, HCP and ICOS type atoms. This feature suggests that the Common Neighbor Analysis inability to assign an atom to a given structure, does not necessarily mean the atom is disordered. However, it is important to note that the CNA focuses on connectivity between neighbors rather than the orientational ordering captured in $qA(i)_l$. Also, the calculation of Common Neighbor Analysis index is very sensitive to the choice of cut-off distance, which is determined by the first minima in radial distribution function $g(r)$. The FCC atoms in this pure A nanocluster appear at large values of $qA(i)_4$ and $qA(i)_6$, while the HCP atoms follows the FCC with smaller $qA(i)_4$ and $qA(i)_6$. The ICO atoms follows have small $qA(i)_4$ and median $qA(i)_6$ in the range of $0.2 - 0.4$.

The $qA(i)_6$-$qA(i)_8$ plane for the same pure A nanocluster configuration is plotted in Fig. 2.25. Most of the atoms are located in the diagonal position, possibly due to the similarity of $qA(i)_6$ and $qA(i)_8$. So it does not show an advantage in structure determination. Because $qA(i)_4$-$qA(i)_6$ plane has been widely used in the literature, it is chosen to analyze structures in order to compare with results(FCC, HCP and ICO region in the plane) obtained from the literature[91].

In the pure A nanocluster, the FCC atoms include various types such as surface FCC, grain boundary, etc.. HCP and ICO atoms have the same structural heterogeneity. In order to investigate $qA(i)_4$-$qA(i)_6$ distribution for bulk FCC, HCP and ICO atoms, Fig. 2.26 is plotted, which shows $qA(i)_4$-$qA(i)_6$ data for atoms with only bulk FCC, bulk HCP and bulk ICO structures for 10 independent configurations of the pure A nanoclusters. In general, the bulk FCC atoms in the nanocluster system have comparatively large $qA(i)_4$ and large $qA(i)_6$, while bulk ICO atoms have small $qA(i)_4$ values. Atoms with bulk HCP structures are distributed between bulk FCC atoms and bulk ICO atoms. This plot describes the structural evolution in the bulk from large $qA(i)_4$ and large $qA(i)_6$ FCC to ICO with small $qA(i)_4$ and medium $qA(i)_6$. The bulk FCC atoms are grouped into different regions in the $qA(i)_4$-$qA(i)_6$ plot with various feature values. The same phenomena is observed in the bulk HCP atoms. Saika-Voivod et al[90] showed that the grouping of global orientational bond order parameters were related to the formation of different sized tetrahedral FCC subunits formed within the cluster at freezing. The larger the tetrahedral subunit, the higher the degree of its ordering. These results suggest the local order parameters capture the same effect.

The $qA(i)_4$-$qA(i)_6$ plane of $x_B = 0.1$ nanocluster at $T = 0.20$ is plotted in Fig. 2.27(a). Every data point shows the $qA(i)_4$ and $qA(i)_6$ value of every atom in one configuration. All the data points are generally located in a diagonal position, where large $qA(i)_4$ is accompanied by large $qA(i)_6$, so $qA(i)_4$ and $qA(i)_6$ are positively correlated. Most of the atoms with small $qA(i)_4$ and small $qA(i)_6$ are B atoms, which are enriched in the core

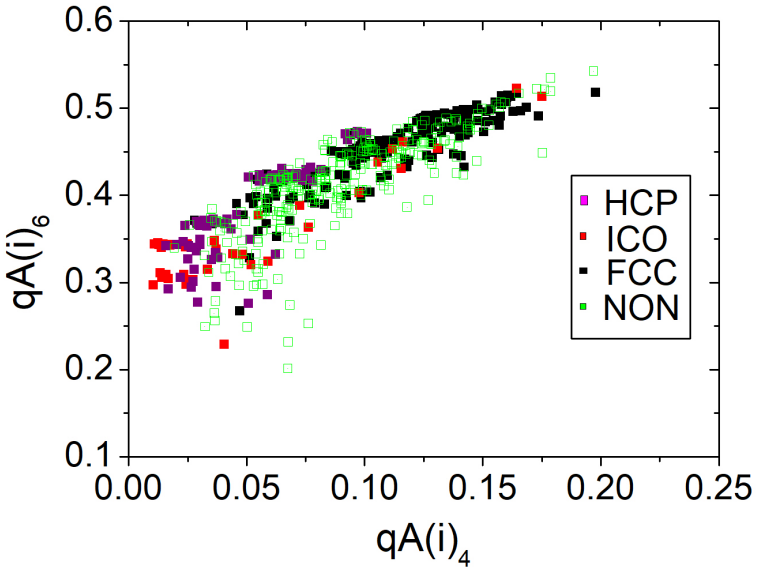

Figure 2.24: $qA(i)_4$-$qA(i)_6$ distribution for one pure A nanocluster at $T = 0.20$. All 600 atoms are colored and categorized into 3 major types based on the structure identified by CNA method.

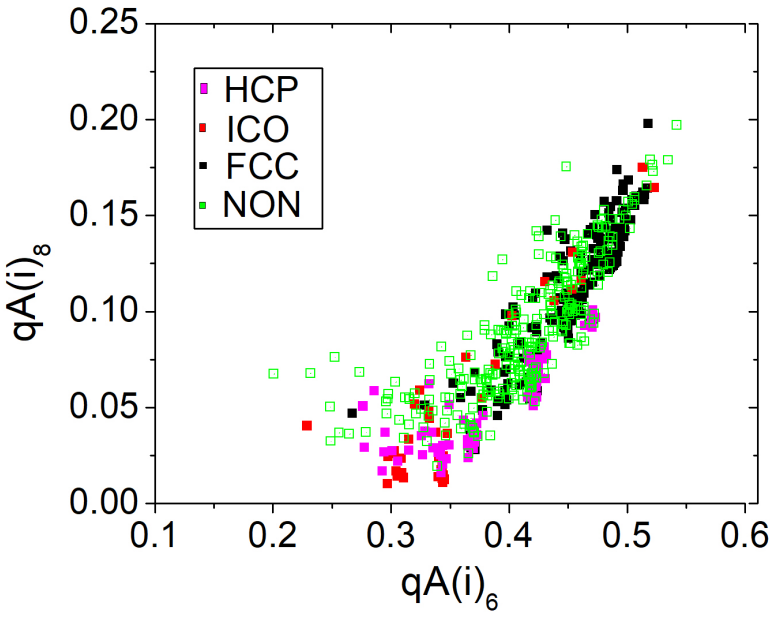

Figure 2.25: $qA(i)_6$-$qA(i)_8$ distribution for one pure A nanocluster at $T = 0.20$. All 600 atoms are colored and categorized into 3 major types based on the structure identified by CNA method.

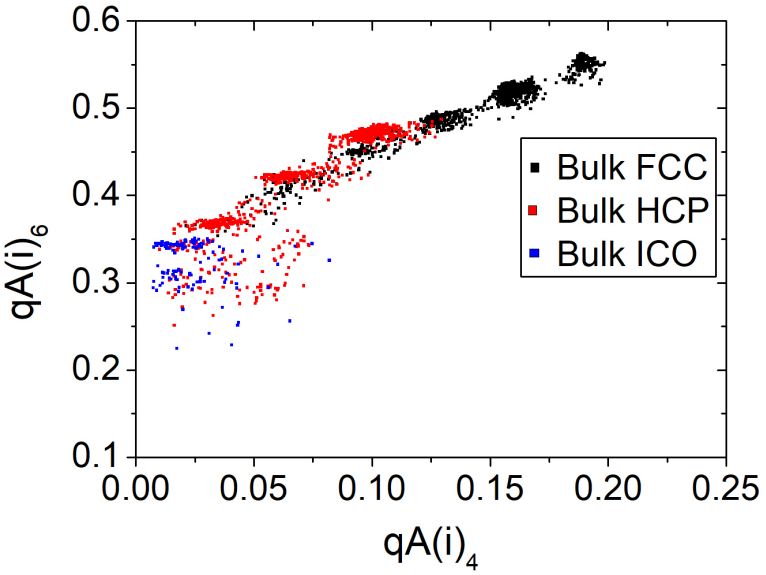

Figure 2.26: $qA(i)_4$-$qA(i)_6$ distribution for 10 pure A nanoclusters at $T = 0.20$. Different colors indicate atoms' local structural environment identified by CNA method. Only 3 types of structures are shown, while other atom data are not plotted.

as demonstrated by the Density profile in Fig. 2.6. Even though the $x_B = 0.1$ undergoes a glass transition when supercooled and the overall disorder at $T = 0.11$ is comparatively large, the $qA(i)_4$-$qA(i)_6$ plane of this cluster shows a significant amount of A atoms presenting large $qA(i)_4$ and $qA(i)_6$. These highly ordered atoms occupied the FCC and HCP region identified in the $qA(i)_4$-$qA(i)_6$ plane of the pure-A nanocluster. One can conjecture that these A atoms form either FCC or HCP crystal seeds at low temperature. These highly ordered A atoms are on the surface as demonstrated in the distribution in Fig. 2.14 obtained using the $< D >_6$ order parameter. Surface enrichment of A atoms allow them to potentially freeze while the B atom enrichment in the core keeps the core of the cluster amorphous.

In the $qA_6 - T$ plot for the $x_B = 0.1$ clusters, it can be seen that the qA_6 increases slightly as T decreases at the low temperature. This behavior is different from that of other glassy nanoclusters with $x_B = 0.2$ and 0.3, whose qA_6 decrease as T decrease. In order to compare $qA(i)_4$-$qA(i)_6$ distribution at high and low temperatures, $qA(i)_4$-$qA(i)_6$ plot at $T = 0.35$ is shown in Fig. 2.27(b). In the high temperature there are more atoms with large $qA(i)_4$. However, in the low temperature, there are more atoms having large $qA(i)_6$, but the number of atoms with large $qA(i)_4$ is significantly reduced. This observation supports the trend in the temperature dependence plot (Fig. 2.19) for the $x_B = 0.1$ clusters that as T decreases the qA_4 decreases significantly, while $qA(i)_6$ increase slightly.

The same $qA(i)_4$-$qA(i)_6$ plane is also plotted for the $x_B = 0.2$ of nanocluster at $T = 0.20$ in Fig. 2.28. From the plot it can be seen that as the number of B atoms increases, the amount of A atoms with large $qA(i)_4$ and $qA(i)_6$ significantly decreases. More data points are presented in the small $qA(i)_4$ and $qA(i)_6$ region. This suggests that as the number of B atoms increases, the energetically favorable A-B interaction

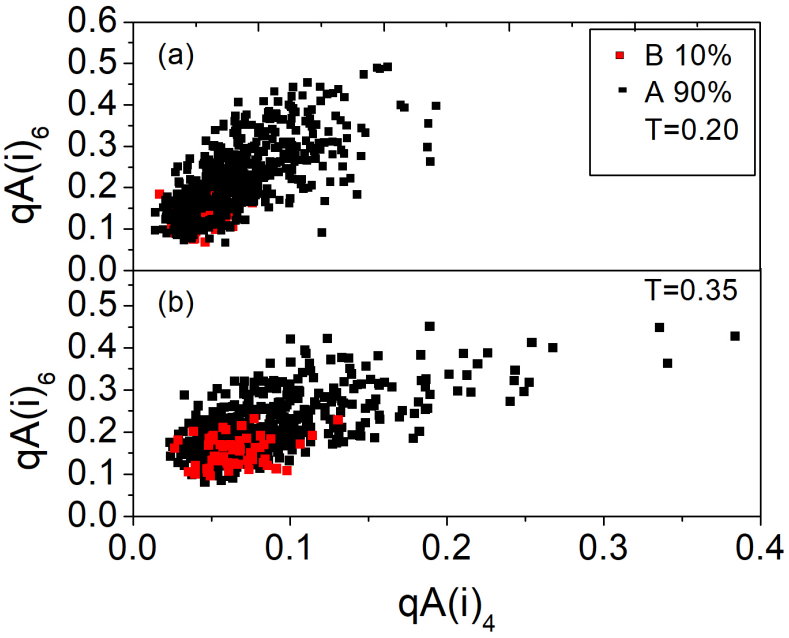

Figure 2.27: $qA(i)_4$-$qA(i)_6$ distribution for $x_B = 0.1$ nanocluster at (a)$T = 0.20$ and (b)$T = 0.35$. Red points represents B atoms and black point represents A atoms.

in the nanocluster generates more disordered A atoms and B atoms with small $qA(i)_4$ and $qA(i)_6$. Since B atoms are enriched in the core as shown by the density profile Fig. 2.7, this locally favored A-B interaction drives more A atoms to the core to form a relatively stable structure with B atoms.

The $qA(i)_4$-$qA(i)_6$ plane for $x_B = 0.3$ nanocluster at $T = 0.20$ is shown in Fig.2.29(a). Compared with the $x_B = 0.2$ nanocluster, the $qA(i)_4$-$qA(i)_6$ values show a moderate decrease. In order to compare $qA(i)_4$-$qA(i)_6$ in the glassy state at the low temperature with $qA(i)_4$-$qA(i)_6$ at high temperature of the liquid state, the $qA(i)_4$-$qA(i)_6$ plane for $x_B = 0.3$ at $T = 0.20$ (Fig. 2.29(a)) are plotted togerther with the same plane at $T = 0.55$ in Fig. 2.29(b). Unexpectedly, the overall $qA(i)_6$ values in the liquid state is slightly larger than that in the glassy state, indicating that some atoms in the liquid is more align and well-organized than the atoms in the glass structure. Similarly, the overall $qA(i)_4$ values at $T = 0.55$ is obviously larger than that at $T = 0.20$.

It appears that most of the atoms have similar orientational bond order at high and low T, while there is a significant change in the $qA(i)_4$ values for a small subset of mainly A type atoms. The insets show the atoms with $qA(i)_4$ values greater than 0.1 and suggest it is the surface atoms that vary the most from high to low temperature. In order to understand where these large $qA(i)_4$ atoms are located in this cluster, a number density distribution of $qA(i)_4 > 0.1$ atoms as a function of radius from the center is plotted in Fig. 2.31. The number density is calculated by finding $qA(i)_4 > 0.1$ atoms in a shell with width 0.25, and then divided by the volume of the shell. Again 10 configurations from the 10 independent runs are chosen to calculate P, with error bars showing the standard deviation. Figure 2.31 shows that the probability of

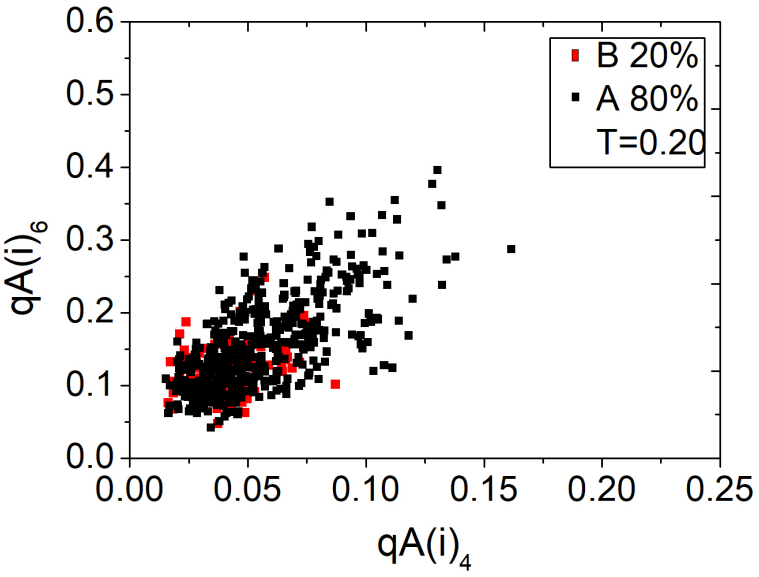

Figure 2.28: $qA(i)_4$-$qA(i)_6$ distribution for $x_B = 0.2$ nanocluster at $T = 0.20$. Red points represents B atoms and black point represents A atoms.

finding a $qA(i)_4 > 0.1$ atom is zero within $r = (0 - 3)$, so these more order atoms are located far from the core. P begins to increase at $r = 3.5$, and reaches a maximum of $P = 0.5$ at $r = 5.0$, and then it decreases, showing a Gaussian-like distribution.

Figure 2.30 shows the $qA(i)_4$-$qA(i)_6$ plane for the $x_B = 0.4$ nanocluster, at high and low temperature above and below the freezing point. In the high temperature liquid state, the $qA(i)_4$ ranges from 0.02 to 0.25, while $qA(i)_6$ is between 0.05 to 0.30. However, the majority of atoms have small $qA(i)_4$ and $qA(i)_6$, corresponding to amorphous liquid. As the temperature is decreased to $T = 0.35$, the majority of the atoms occupy a new $qA(i)_4$-$qA(i)_6$ region with small $qA(i)_4$ around 0.05 and large $qA(i)_6$ around 0.45. This region is not observed in the pure A nanocluster, indicating a different structure not seen in pure A nanoclusters. Compared with the literature, this region corresponds to the Body Center Cubic(BCC) structure[91].

2.3.7 Voronoi Diagram

Since glasses do not have the long range order and a large overlap was present in the bond order parameter ($qA(i)_4$ and $qA(i)_6$) distributions between the liquid state and the glassy state, another method to further understand nanocluster glassy structures is needed. Voronoi analysis was applied to investigate the three glassy inherent structures in the $x_B = 0.1, 0.2$ and 0.3 systems. The Voronoi polyhedra around the B atoms in the core were analyzed because these have been shown to be important in the bulk glass formers. Also, the Voronoi analysis at the surface is sensitive to small numerical fluctuations caused by boundary conditions.

At high temperature, $T = 0.35$, the B atoms in the core are identified to have 404 distinct types of Voronoi cell in 2000 configurations of the $x_B = 0.1$ nanoclusters. At low temperature in the glass state,

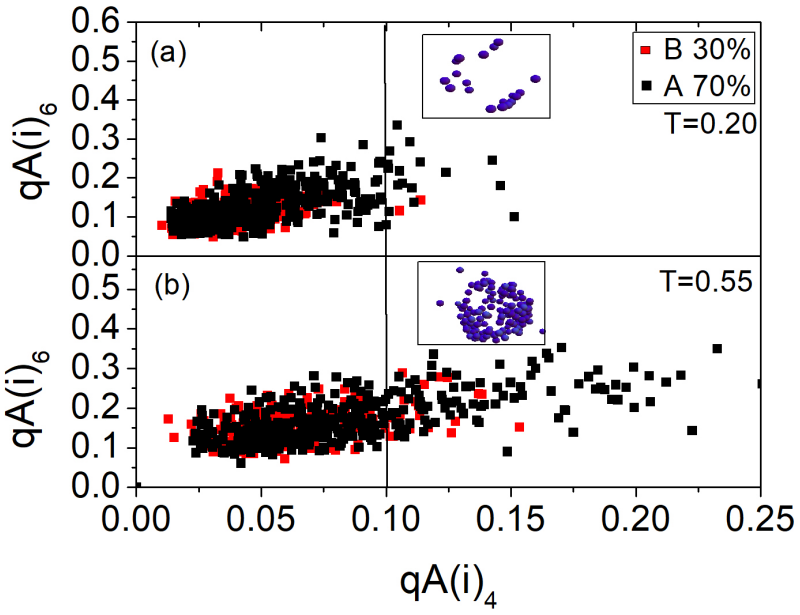

Figure 2.29: $qA(i)_4$-$qA(i)_6$ distribution for $x_B = 0.3$ nanocluster at (a)$T = 0.20$ and (b)$T = 0.55$. Red points represents B atoms and black point represents A atoms. Atoms with q4 above 1.0 are visualized in the square box.

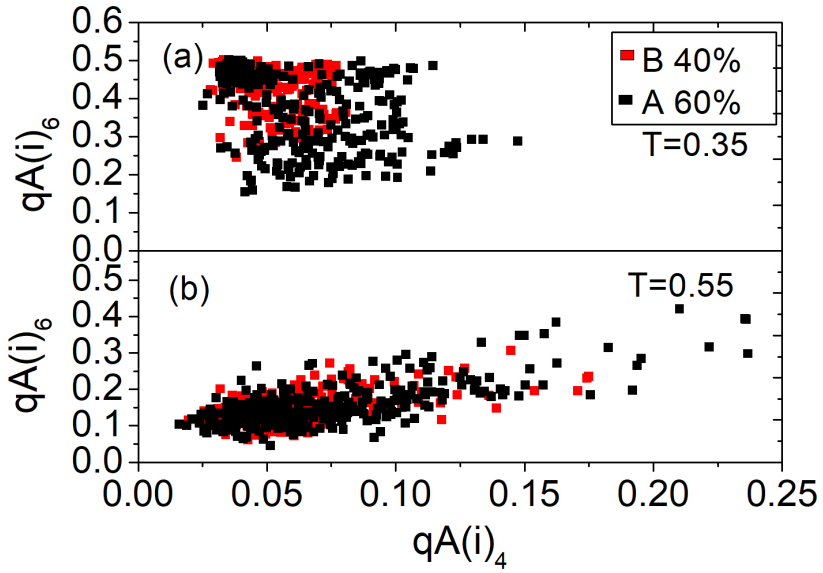

Figure 2.30: $qA(i)_4$-$qA(i)_6$ distribution for $x_B = 0.4$ nanocluster at (a)$T = 0.35$ and (b)$T = 0.55$. Red points represents B atoms and black point represents A atoms.

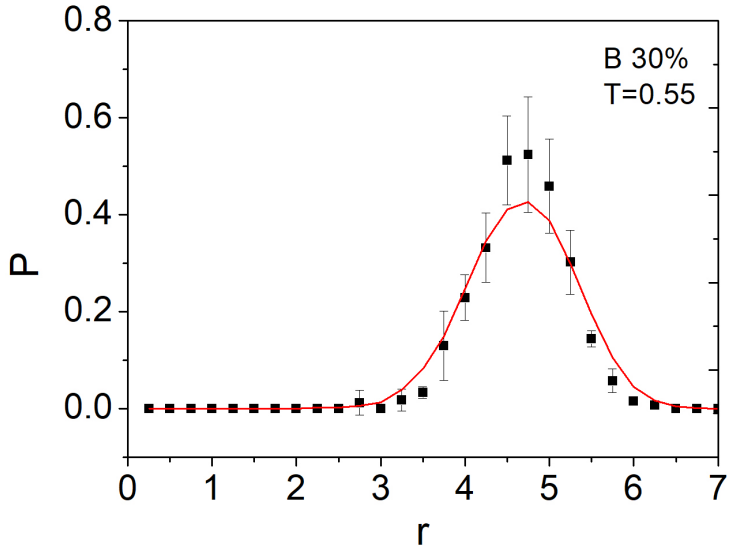

Figure 2.31: The number density of atoms with $qA(i)_4 > 0.1$, as a function of radius from the center of the $XB = 0.2$ nanocluster. Red line is a guide to the eye. B composition and temperature are shown in graph.

$T = 0.20$, this Voronoi cell number decreases to 116. The same decrease of Voronoi cell types from high temperature to low temperature was also observed for the glassy $x_B = 0.2$ and 0.3 nanoclusters. In the $x_B = 0.2$ nanoclusters, B atoms in the core of the liquid state at high temperature $T = 0.35$ have 697 types of Voronoi cells in 2000 configurations. At low temperature in the glass state $T = 0.20$, the Voronoi cell number decreases to 178. While in the $x_B = 0.3$ nanoclusters, the liquid state at high temperature $T = 0.35$ have 1012 types of Voronoi cell in 2000 configurations. At low temperature in the glass state, $T = 0.20$, only 343 types were observed. It is obvious that the types of Voronoi cell increase as the B atom fraction increase from $x_B = 0.1$ to $x_B = 0.3$, indicating that introducing B atoms increase the diversity of local structures.

Figures 2.32, 2.33 and 2.34 show the fraction of top 10 most predominant Voronoi cells of $x_B = 0.1, 0.2$ and 0.3 nanoclusters, at temperatures above and below the glass transition. Each Voronoi cell fraction is calculated by suming all Voronoi cells of the same index in 2000 configurations and then normalized by the total number of B atoms in the core.

The top 10 most predominant Voronoi polyhedron around the B core atoms in the three types of nanoclusters are the same, even though the B atom fraction increase from $x_B = 0.1$ to $x_B = 0.3$. These predominant Voronoi polyhedra have coordination numbers in the range of $9 - 11$, which is the low coordination number, prism-like structures. In the bulk Lennard-Jones liquid, the possibility to supercool the cluster below equilibrium melting temperature was due to the presence of icosahedron structures (0 0 12 0), which are more energetically preferred[59]. However, icosahedron structures are not observed in these nanoclusters.

The top 10 most predominant Voronoi polyhedra for $x_B = 0.1$ shown in Fig. 2.32 indicates that the largest fraction cells were observed in (0 2 8 0). When the temperature decreases from $T = 0.35$ to $T = 0.20$,

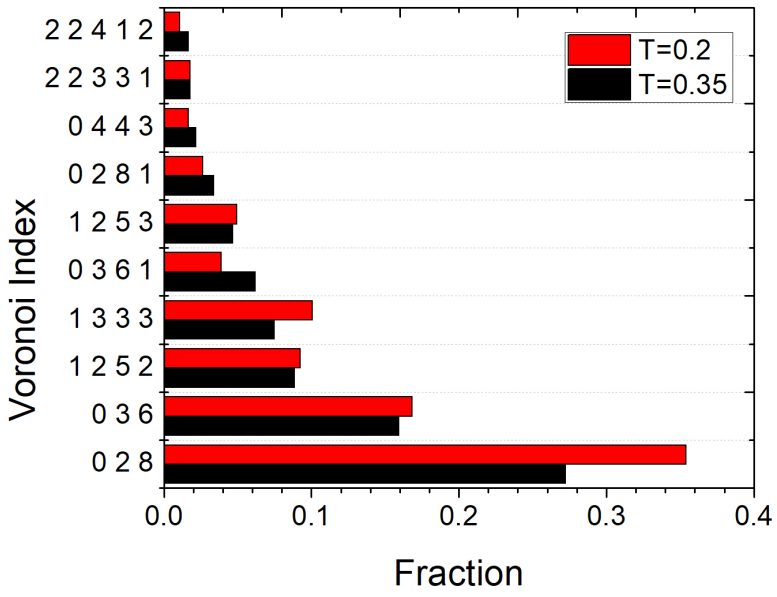

Figure 2.32: 10 most frequent Voronoi cell for $x_B = 0.1$ nanocluster system at temperatures above and below glass transition temperature.

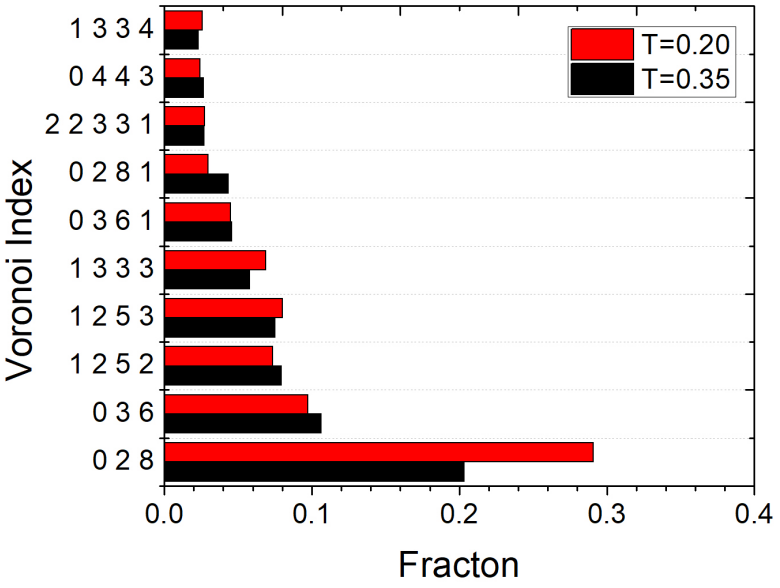

Figure 2.33: 10 most frequent Voronoi cell for $x_B = 0.2$ nanocluster system at temperatures above and below glass transition temperature.

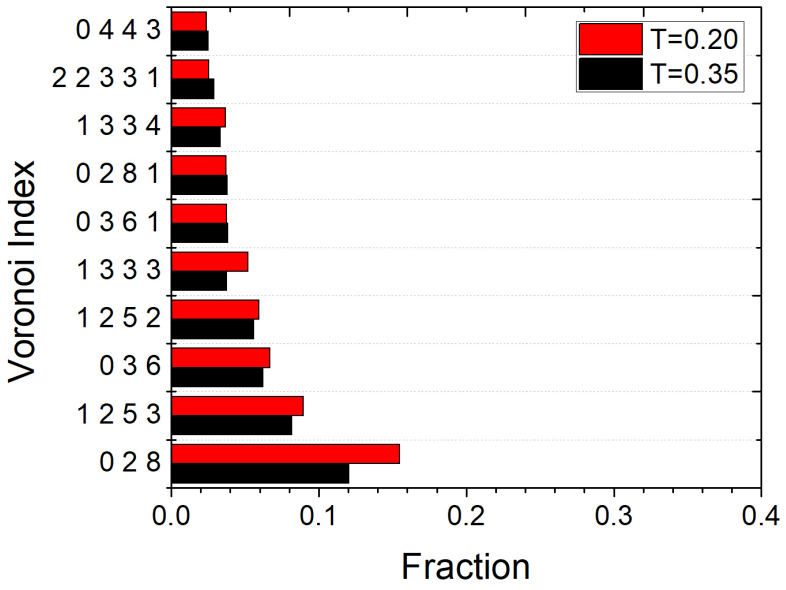

Figure 2.34: 10 most frequent Voronoi cell for $x_B = 0.3$ nanocluster system at temperatures above and below glass transition temperature.

the (0 2 8 0) polyhedron has the greatest increase. Other dominant polyhedra are (0 3 6 0), (1 2 5 2), (1 3 3 3).

The same Voronoi diagram for $x_B = 0.2$ is shown in Fig. 2.33. Again it indicates that the most predomiant polydedron is still (0 2 8 0). (1 2 5 3) becomes more dominant in $x_B = 0.2$ cluster compared with the number of (1 2 5 3) in $x_B = 0.1$ cluster. In the $x_B = 0.3$ cluster, (0 2 8 0) is again the most predominant type, but its fraction is small compared the (0 2 8 0) fraction in $x_B = 0.1$ and 0.2 clusters. Even at low temperature $T = 0.20$, the (0 2 8 0) fraction is only 0.16. As the number of B atoms increases from $x_B = 0.1$ to $x_B = 0.3$, the fraction of (0 2 8 0) at low temperature $T = 0.2$ decreases, suggesting that other Voronoi polyhedron become more and more important, occupying a larger fraction, such as (1 2 5 3), (1 2 5 2), (1 3 3 3). The broadening of the distribution of Voronoi polyhedra as x_B increases highlights the increasing diversity of local structure. This is consistent with the $x_B = 0.3$ clusters being identified as the most disordered structures according to orientational disorder parameters.

To further examine the structural change between the glass and liquid in supercooled nanoclusters, the temperature dependence of the fraction of Voronoi cell with index (0 2 8 0), (0 3 6 0), (1 3 3 3) and (0 2 8 1) are plotted in Figures 2.35, 2.36 and2.37 for each cluster compositions. The four chosen Voronoi cells are within the top 10 most frequent Voronoi cells in our nanoclusters and they exhibit most significant increase/decrease when supercooled.

Figure 2.35 shows the fraction of four types of Voronoi cell centered around the B type atoms in the core in the inherent structures of the $x_B = 0.1$ nanoclusters. Every data point in these plots represents

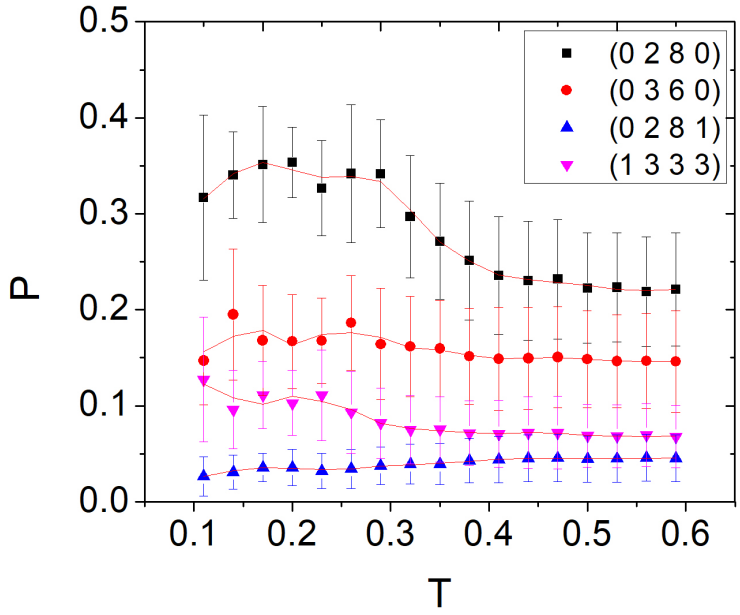

Figure 2.35: Temperature dependence of 4 predonimant Voronoi Cell in inherent structure of $x_B = 0.1$ nanocluster.

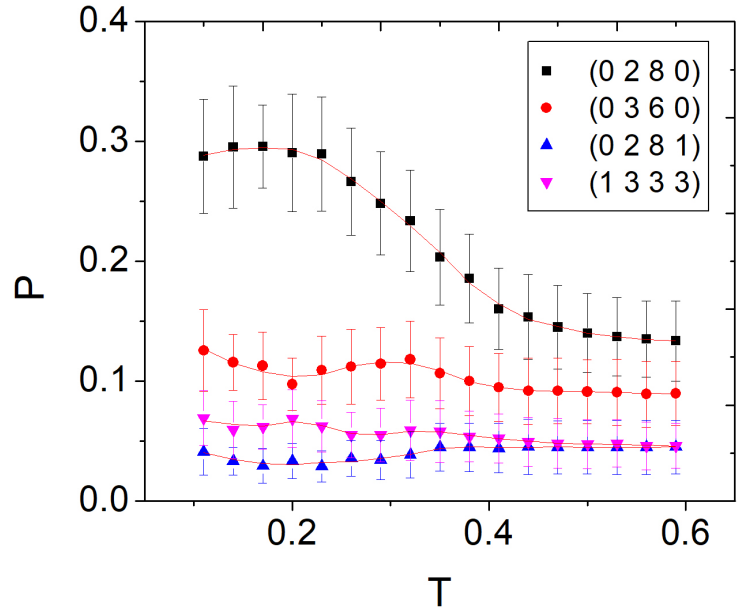

Figure 2.36: Temperature dependence of 4 predonimant Voronoi Cell in inherent structure of $x_B = 0.2$ nanocluster.

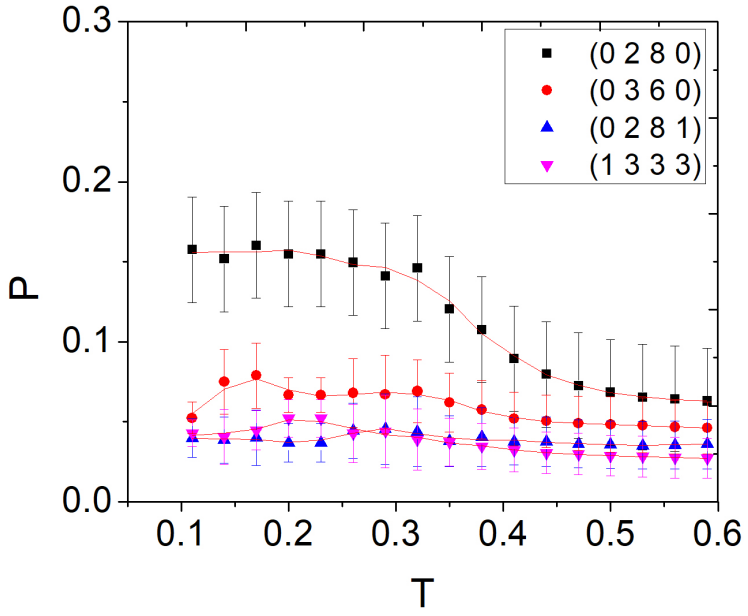

Figure 2.37: Temperature dependence of 4 predonimant Voronoi Cell in inherent structure of $x_B = 0.3$ nanocluster.

the average Voronoi cell fraction taken over 2000 configurations, and the error bars represents the standard deviation of these 2000 configurations. At both high and low temperature above and below glass transition, (0 2 8 0) has the largest fraction compared with (1 3 3 3), (0 3 6 0) and (0 2 8 1). At high temperature in the liquid state, about 22% of core B atoms have the (0 2 8 0) local structure. As the temperature decreases, the portion of (0 2 8 0) increases continuously before reaching a maximum of $P = 0.35$ at about $T = 0.18$. The fraction of the (0 3 6 0) structure also increases as T decreases, and reaches its maximum at $T = 0.18$. The fraction of the (1 3 3 3) structure increases as T decreases without showing a maximum. In contrast, the fraction of (0 2 8 1) decreases continuously as T decreases and it becomes close to zero when $T = 0.11$.

Figure 2.36 and 2.37 demonstrate the same temperature dependence of the four predominant Voronoi cell identified in the inherent structure of $x_B = 0.2$ and 0.3 nanoclusters. The similar feature in these three plots is that at low temperature, the (0 2 8 0) structure shows the largest fraction in all glassy nanoclusters and it exhibits the largest increase when supercooled.

In the $x_B = 0.2$ nanocluster, the fraction of (0 2 8 0) increases from 0.15 to 0.30 as temperature decreases. As T decreases, the fraction of (0 3 6 0) increases and then decreases to a minima at $T = 0.2$, and then increases again, while (1 3 3 3) shows a local maximum $T = 0.2$. As T decreases, the fraction of (0 2 8 1) decreases and then increases at $T = 0.2$. In the $x_B = 0.3$ nanocluster, the fraction of the 4 Voronoi cells are very close, but the (0 2 8 0) structure still has the largest fraction, which increase from 0.06 to 0.15 when T decrease. As T decreases, the fraction of (0 3 6 0) increases to a maximum at $T = 0.17$, and the (1 3 3 3) increases to a maximum at $T = 0.20$. In contrast with the $x_B = 0.1$ and 0.2 clusters, here (0 2 8 1) increases

as T decreases before reaching its maximum at $T = 0.3$. These features suggest that even though the four most predominant Voronoi cells are the same for the three glassy nanoclusters, their local structures show significant differences when the fraction of B atoms varies.

2.4 Discussion

2.4.1 Summary of hypothesis

In this research, the hypothesis is put forward that composition alters the glass forming ability of KA binary Lennard-Jones clusters. And at the same time, composition alters the type and distribution of local structures observed in the supercooled and glassy phases of KA binary Lennard-Jones clusters. Based in the hypothesis, the discussion centers on the phase diagram of binary Lennard-Jones nanoclusters. How their local structures vary with different B type atom fractions.

2.4.2 Phase diagram

A phase transition diagram is mapped out in Fig. 2.38 based on the phase transition temperature obtained in Fig. 2.2.

This phase diagram shows the phase transition temperature at various B-atom compositions. For the pure-A nanocluster and $x_B = 0.05, 0.4, 0.5$, the systems freeze upon cooling. A glass transition was observed with $x_B = 0.1, 0.2$ and 0.3. The V-shape phase transition curve shows the lowest T_g occurred in $x_B = 0.1$ system. It also indicates that the $x_B = 0.3$ system is the best glass former in our LJ nanocluster, since the $x_B = 0.3$ nanocluster undergoes a glass transition at the highest temperature. The glass transition temperatures in $x_B = 0.1, 0.2$ and, 0.3 nanoclusters are significantly lower than that of the bulk Lennard-Jones liquid. Figure 2.17 shows that $x_B = 0.33$ nanocluster still undergoes a glass transition at low T since its $< D >_6$ at $T = 0.11$ is large and close to that of $x_B = 0.30$ system, with small error bars indicating a homogeneous structure.

The pure-A nanocluster eventually crystallized into mainly FCC and HCP local environment, with a small fraction of ICO . The FCC, HCP and ICO crystals have different sizes, showing different $qA(i)_4$-$qA(i)_6$ values.

The $x_B = 0.1$ nanocluster appears to contain a glassy core with a more ordered surface below the phase transition temperature. The amorphous core is mainly composed of the (0 2 8 0) Voronoi cells. The more ordered surface is mainly composed of A atoms with large $qA(i)_4$-$qA(i)_6$ values consistent with the FCC/HCP structure. When a few small size B atoms are present in the nanoclusters, they form bicapped squared antiprism (0 2 8 0) with A atoms. And since those B atoms are distributed in the core shown by Fig.2.6, the bicapped squared antiprism constructed by B atoms are also distributed in the core. This structure frustrates crystallization and the $x_B = 0.1$ system forms a glass in general. One can speculate that

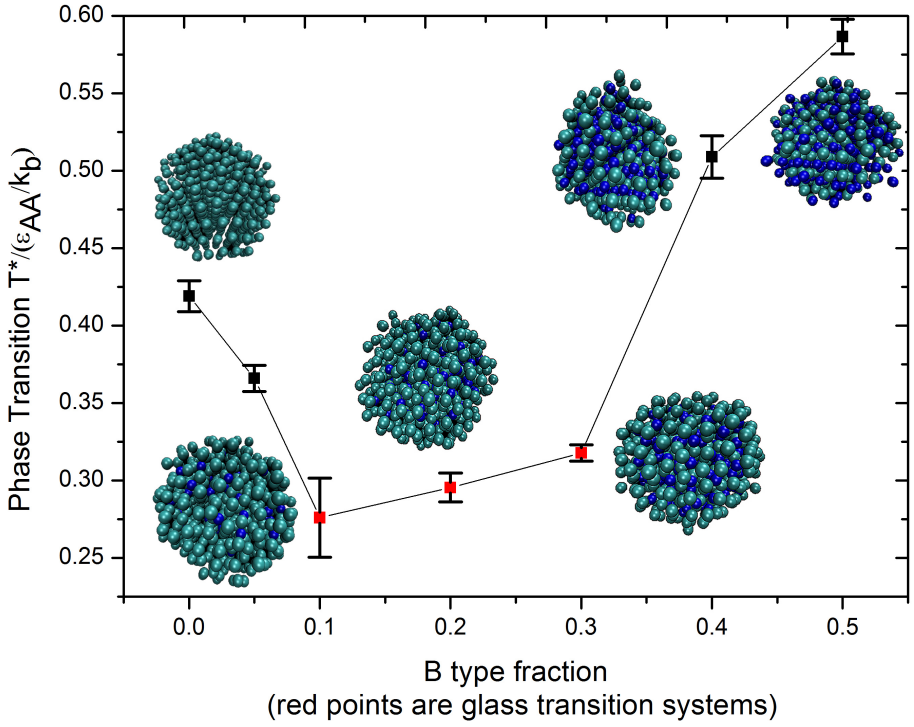

Figure 2.38: Phase diagram. Phase Transition temperature as a function of B-type particle fraction x_B. Glass transition occurs in system with $x_B = 0.1, 0.2, 0.3$. Crystallization is observed when $x_B > 0.3$ and $x_B < 0.1$.

this frustration of crystallization begins in the core and was mainly caused by bicapped squared antiprism. Even though $x_B = 0.1$ nanocluster forms a glass, structural heterogeneity is also observed at low temperature as shown by the large error bar in Fig. 2.17. This is caused by surface A atoms freezing into structures having large $qA(i)_4$ and $qA(i)_6$ as shown in Fig. 2.27. Eventually, this $x_B = 0.1$ nanocluster forms a glass instead of crystal. This is aided by the enrichment of the B atoms in the core. The surface ordering is also caused by the A enrichment. This effect is interesting because the crystallization of pure Lennard-Jones clusters was shown to begin in the core of the particles. However, in the binary mixtures, ordering is force to occur at the surface.

The $x_B = 0.2$ and 0.3 nanoclusters are good glass formers, since their configuration exhibit small error bars in $< D >_6$ at $T = 0.11$, and they show little fluctuation in their $qA_6 - T$ and $q0_6 - T$ curves, suggesting that their structures are homogeneous. The glass transition temperature for the $x_B = 0.3$ nanocluster is higher than that of the $x_B = 0.2$ nanocluster, which means that introducing more B atoms makes the system form a glass at a higher temperature. This probably as a result of increasing the number of A-B interaction. So the glass forming ability is better when $x_B = 0.3$.

The $x_B = 0.4$ system crystallized into the CsCl-type structure, which is found at $x_B = 0.5$ Lennard-Jones bulk crystal, at a comparatively high temperature. In the bulk system, the $x_B = 0.4$ Lennard-Jones liquid

forms an amorphous glass when cooled bellow the glass transition temperature. And $x_B = 0.5$ Lennard-Jones liquid freeze into CsCl type crystal. One reason for the crystallization in the $x_B = 0.4$ nanocluster is due to the enrichment of B atoms in the core and a large fluctuation leading to CsCl-type structure formed. Another possible reason for this difference is that the surface effect in nanocluster induces the system to nucleate more easily. Small cluster system usually freeze more easily than the bulk because the fluctuation are generally large.

There are some simulation studies attempting to crystallize $x_B = 0.2, 0.3, 0.4$ bulk Lenard Jones liquid, with one result showing crystal seeds composed of FCC/HCP structures[102] for $x_B = 0.2, 0.3$ and AB CsCl-type crystals for $x_B = 0.4$. They suggest that there is no competition effect between the FCC/HCP seed and CsCl-type seeds leading to glass formation because they are not formed in the same B atom fraction. My nanocluster system also supports the same argument. While pure A nanolucster forms FCC, HCP and ICO structures, CsCl-type structures with small $qA(i)_4$ and large $qA(i)_6$ are not found in this cluster. The $x_B = 0.4$ cluster forms CsCl-type structure with a perfect homogeneity as demonstrated by the small error bars in $< D >_6$, $qA_6{-}T$, $qA_4{-}T$ and $q0_6{-}T$. Again there is no competing effect between FCC/HCP structure and CsCl-type structure in our nanoclusters to induce glass transition. However, the most disordered liquid occurs at the x_B fraction where the crystal appears to change from FCC to the CsCl structure. This suggests that the liquid may have difficulty in identifying which local structure to form.

In between $x_B = 0.3$ and $x_B = 0.4$, Fig. 2.17 shows the nanoclusters structure with $x_B = 0.33, 0.35$ at low temperature $T = 0.11$. $< D >_6$ for $x_B = 0.33$ cluster is high, up to 1.7, with small error bars. Thus the $x_B = 0.33$ cluster is a good glass former and should have similar behavior as $x_B = 0.3$ cluster. When x_B increase to $x_B = 0.35$, the $< D >_6$ is 0.7, and intermediate value with large fluctuations indicating structural heterogeneity. This may suggest that $x_B = 0.35$ cluster is a mix of glassy state and crystal structure.

2.4.3 Change in local structure with varous composition

In the pure A nanocluster, the final state in the low temperature is a heterogeneous crystal, mainly composed of FCC and HCP structure, with some ICO atoms. These structures exhibit different sizes, causing a wide distribution in the $qA(i)_4$-$qA(i)_6$ plane. This structural heterogeneity, caused by various structure types and different sizes, is consistent with the large error bars observed in $< D >_6$ in $T = 0.11$.

When only 10% of B atoms are introduced into the cluster, they are highly enriched in the core, and since the A-B interaction is energetically favorable, it leads to some fraction of B atoms to core of the cluster and forms an amorphous structure mainly composed of Voronoi cell (0 2 8 0). Since the number of B atoms is too small to construct A-B interactions with all A atoms, surface enrichment of A atoms occurs as shown in the density profile in Fig. 2.6. These surface A atoms present small values of $D(i)_6$ (see Fig. 2.14) and large values of $qA(i)_4$ and $qA(i)_6$. Due to this structural heterogeneity and phase separation, the surface ordered effect is observed in this $x_B = 0.1$ clusters, as can be seen in the temperature dependence of $q0_6$, whose large error bars and increasing value of $q0_6$ as T decreases are evidence of freezing.

When the amount of B atoms increases to $x_B = 0.2$, surface enrichment of A atoms can still be observed. The favorable A-B interaction leads to enrichment of B atoms in the core, which forms (0 2 8 0) Voronoi cells with A atoms in the low temperature. In the density profile (Fig. 2.7) it can be seen that the probability of B atoms is 0.33, consistent with the A:B ratio in the (0 2 8 0) Voronoi cells. In the $x_B = 0.2$ nanoclusters, since the amount of B atoms increases, the surface freezing effect is suppressed, and there are no large values of $qA(i)_4$ and $qA(i)_6$ in Fig.2.28. Indeed, structural homogeneity is observed by the small error bars in $< D >_6$, $qA_6 - T$ and $qA_6 - T$. Due to this B atom increase, the $x_B = 0.2$ cluster is more glassy than the $x_B = 0.1$ cluster, with higher glass transition temperature and larger $< D >_6$ at $T = 0.11$.

When the number of B atoms increases further to $x_B = 0.3$, the core enrichment of B atoms is less obvious but it still shows that the core has a B-atom probability $P = 0.4$, larger than the stoichiometry 0.3. This cluster is a better glass former compared with the one with $x_B = 0.2$, since it shows higher glass transition temperature and larger $< D >_6$. In the $qA(i)_4$-$qA(i)_6$ plane, most atoms are drived to the region with smaller values of $qA(i)_4$ and $qA(i)_6$ since there are more energetically favorable A-B interactions. Structural homogeneity can also be seen from the small error bars in $< D >_6$, $qA_6 - T$ and $qA_6 - T$ for the $x_B = 0.3$ nanocluster.

In the $x_B = 0.4$ nanocluster, the core enrichment of B atoms can also be seen in Fig. 2.9, which shows that the B-atom probability in the core is 0.5. It is the core enrichment of B atoms that cause the $x_B = 0.4$ nanocluster to crystallize into the CsCl-type structure at low temperatures. This is a structurally homogeneous cluster compare with the pure A cluster, as demonstrated by the small error bars in $< D >_6$, $qA_6 - T$ and $q0_6 - T$. The crystal structure seen in pure A nanocluster, FCC, HCP and ICO, do not occurred in the $x_B = 0.4$ nanocluster, since the $qA(i)_4$-$qA(i)_6$ plane of the $x_B = 0.4$ nanocluster presents a different $qA(i)_4$-$qA(i)_6$ region. This may suggest that there is no competing effect between HCP/FCC and CsCl-type structure to flustrate freezing and forms a glass. Surface freezing is observed in $x_B = 0.1$ nanocluster, while in pure A atoms Lennard- Jones cluster, the energy minima is the formation of different size FCC subunit in the core with a disorder surface. Introducing small size B atoms not only disrupts the core crystallization of FCC, but leads to surface freezing.

The fraction of (0 2 8 0) structure with B atoms in the core decreases significantly as number of B-atom increase from $x_B = 0.1$ to $x_B = 0.3$. Nevertheless, the (0 2 8 0) Voronoi cell is the most predominant local structure in all three glassy systems, and has the biggest increase when the cluster is cooled to low temperature. Since the (0 2 8 0) Voronoi cell frustrate the crystallization upon supercooling, the change of B-atom composition from $x_B = 0.1$ to $x_B = 0.3$ does not change the glass forming mechanism. But this varying composition does change the local structure of the glassy nanoclusters. There are more Voronoi polyhedron becoming important as B atom fraction increase. This result is consistent with the increasing disorder from $x_B = 0.1$ cluster to $x_B = 0.3$ cluster.

In the three glassy systems $x_B = 0.1, 0.2$ and 0.3, the decrease of qA_8 as x_B increases can be linked to the increasing types of Voronoi cells formed when more B atoms are introduced into the system. As the fraction

of (0 2 8 0) Voronoi cell decreases, their qA_8 have a slight decrease. Significantly more types of Voronoi cells are found around B core atoms as x_B increase from 0.1 to 0.3 , and this is consistent with the increasing disorder parameter $< D >_6$ within a cluster shown in Fig. 2.17 and Fig. 2.22.

A decrease fraction of (0 2 8 0) Voronoi cell was observed when x_B increase from 0.1 to 0.3. We know the $x_B = 0.3$ is a better glass former with a comparatively high T_g shown in Fig. 2.38, the comparative large $< D >_6$ shown in Fig. 2.17, and the homogeneious glassy state in $x_B = 0.3$ nanocluster. However, the (0 2 8 0) Voronoi cell has been found to stabilize a glassy structure with the formation of cylindrical structure constructed by face connection of (0 2 8 0) Voronoi cell[59]. A question rises why the fraction of the (0 2 8 0) Voronoi cell is reduced in $x_B = 0.3$ cluster.

One possibility to explore is that the total number of atoms involved in the bicapped squared antiprism polyhedra actually increases or remains the same as x_B is varied because the total number of B atoms available for forming the structures increases. Alternatively, it is known that the (0 2 8 0) polyhedra can tile space, but only with the Al_2Cu structure, which occurs when the composition is $x_B = 0.33$. At lower compositions the B atoms will be surrounded by as many A atoms as possible to achieve a low energy, but these will be incompatible with the Al_2Cu structure and be unable to crystallize. As the B atom fraction increases the probability that the (0 2 8 0) polyhedra has the correct composition should increase, but the total number of other competing structures also increases. This increase in diversity of structures allows the system to form a glass before crystallization can occur.

2.4.4 Future work

This thesis clearly demonstrates that composition has a significant effect on the nature of the structure surrounding an atom in the liquid phase. In particular, the fraction of B atoms involved in the $(0, 2, 8, 0)$, the bicapped squared antiprism local strucuture decreases as x_B increases for the glass forming liquids. In the bulk KA model, with $x_B = 0.2$, aggregations of connected $(0, 2, 8, 0)$ polyhedra have been correlated with slow dynamics of the supercooled liquid[59]. It would then be useful to examine how the relationship between the presence of this local structure and dynamics in the liquid varies as the composition changes. The fraction of B atoms in the $(0, 2, 8, 0)$ is lowest for the $x_B = 0.3$ structure in the nanocluster system, yet it has the highest glass transition temperature. This may suggest factors other than this single local structure, become important for other compositions.

When compared to the ultra-stable glasses formed through vapour deposition, the nanocluster glasses exhibit much higher fractions of the low energy (0,2,8,0) polyhedra, which suggests that they are possibly reaching the deepest parts of the potential energy landscape. This suggests the nanoparticle systems might be useful for examining potential energy landscape descriptions of the glass transition, such as the possibility of an ideal glass. This would require calculating configurational entropy of the cluster as a function of temperature to see if this tends to zero at a finite temperature.

The current work also reveals a counter-intuitive feature in the temperature dependence of average

order/disorder parameters. Based on simple entropic arguments, one would expect structures to become more ordered, signified by a larger average order parameter, as the temperature decreases. However, the average order parameters for the nanoclusters, qA_4 and qA_6, decrease with decreasing temperature (see Fig. 2.18). The global order parameter, Q_6 shows increasing order in the liquid phase for $x_B = 0$ and $x_B = 0.1$, but decreasing order for the remaining compositions. This may be a feature associated with the nanocluster systems and caused by surface effects, where ordering around the surface atoms varies differently to that in the bulk, influencing the overall average. Examining the temperature dependence of the order parameters for the bulk liquids will be able to help identify which features are unique to the nanocluster systems and which are more universal.

References

[1] C. A. Angell. Formation of glasses from liquids and biopolymers. *Science*, 267(5206):1924–1935, 1995.

[2] W. Doster. The protein-solvent glass transition. *Biochimica et Biophysica Acta (BBA) - Proteins and Proteomics*, 1804(1):3 – 14, 2010.

[3] H. Nakagawa, H. Kamikubo, and M. Kataoka. Effect of conformational states on protein dynamical transition. *Biochimica et Biophysica Acta (BBA) - Proteins and Proteomics*, 1804(1):27 – 33, 2010.

[4] P. G. Debenedetti, T. M. Truskett, C. P. Lewis, and F. H. Stillinger. Theory of supercooled liquids and glasses: Energy landscape and statistical geometry perspectives. *Advances in Chemical Engineering*, 28:21 – 79, 2001.

[5] A. Inoue, T. Zhang, J. Saida, M. Matsushita, M. W. Chen, and T. Sakurai. High strength and good ductility of bulk quasicrystalline base alloy system. *Materials Transactions*, 40(10):1137–1143, 1999.

[6] T. Fukunaga, K. Itoh, T. Otomo, K. Mori, M. Sugiyama, H. Kato, M. Hasegawa, A. Hirata, Y. Hirotsu, and A. C. Hannon. Voronoi analysis of the structure of ni-zr-al ternary metallic glass. *Materials Transactions*, 48(7):1698–1702, 2007.

[7] A. S. Kivelson and G. Tarjus. In search of a theory of supercooled liquids. *Nature Materials*, 7(11):831–833, 2008.

[8] M. D. Ediger, C. A. Angell, and Sidney R. Nagel. Supercooled liquids and glasses. *The Journal of Physical Chemistry*, 100(31):13200–13212, 1996.

[9] R. Zhang, A. Khalizov, L. Wang, M. Hu, and W. Xu. Nucleation and growth of nanoparticles in the atmosphere. *Chemical Reviews*, 112(3):1957–2011, 2012.

[10] B. Shizgal and J. C. Barrett. Time dependent nucleation. *The Journal of Chemical Physics*, 91(10):6505–6518, 1989.

[11] P. G. Debenedetti and F. H. Stillinger. Supercooled liquids and the glass transition. *Nature*, 410(6825):259–267, 2001.

[12] L. Berthier and G. Biroli. Theoretical perspective on the glass transition and amorphous materials. *Review of Modern Physics*, 83:587–645, 2011.

[13] C. H. Yang and H. Qiu. Theory of homogeneous nucleation: A chemical kinetic view. *The Journal of Chemical Physics*, 84(1):416–423, 1986.

[14] F. F. Abraham. Chapter 1 - the nature of the nucleation process. In Farid Fadlow Abraham, editor, *Homogeneous Nucleation Theory*, pages 1 – 8. Academic Press, 1974.

[15] D. W. Oxtoby. Nucleation of first-order phase transitions. *Accounts of Chemical Research*, 31(2):91–97, 1998.

[16] Z. Lin, E. Leveugle, E. M. Bringa, and L. V. Zhigilei. Molecular dynamics simulation of laser melting of nanocrystalline au. *The Journal of Physical Chemistry C*, 114(12):5686–5699, 2010.

[17] W. Liu and L. Zhang. On the nano/micro-mechanics of metallic glass. *Critical Reviews in Solid State and Materials Sciences*, 40(3):137–163, 2015.

[18] A. Cavagna. Supercooled liquids for pedestrians. *The Journal of Physical Chemistry*, 476(51):14–68, 2009.

[19] L. M. Martinez and C. A. Angell. A thermodynamic connection to the fragility of glass-forming liquids. *Nature*, 410(6829):663–667, 2001.

[20] H. Sillescu. Heterogeneity at the glass transition: A review. j. non-cryst. solids 243, 81-108. *Non-Crystalline Solids*, 243:81–108, 1999.

[21] M. D. Ediger. Spatially heterogeneous dynamics in supercooled liquids. *Annual Review of Physical Chemistry*, 51(1):99–128, 2000.

[22] S. C Glotzer. Spatially heterogeneous dynamics in liquids: insights from simulation. *Journal of Non-Crystalline Solids*, 274(1):342 – 355, 2000.

[23] S. Golde, T. Palberg, and H. J. Schope. Correlation between dynamical and structural heterogeneities in colloidal hard-sphere suspensions. *Nature Physics*, 12(7):712–717, 2016.

[24] L. Yan, G. Düring, and M. Wyart. Why glass elasticity affects the thermodynamics and fragility of supercooled liquids. *Proceedings of the National Academy of Sciences*, 110(16):6307–6312, 2013.

[25] W. T. Laughlin and D. R. Uhlmann. Viscous flow in simple organic liquids. *The Journal of Physical Chemistry*, 76(16):2317–2325, 1972.

[26] C.A. Angell. Relaxation in liquids, polymers and plastic crystals — strong/fragile patterns and problems. *Journal of Non-Crystalline Solids*, 131:13 – 31, 1991.

[27] J. L. Green, K. Ito, K. Xu, and C. A. Angell. Fragility in liquids and polymers: new, simple quantifications and interpretations. *The Journal of Physical Chemistry B*, 103(20):3991–3996, 1999.

[28] M. Mehta, G. B. McKenna, and R. Suryanarayanan. Molecular mobility in glassy dispersions. *The Journal of Chemical Physics*, 144(20):204506, 2016.

[29] F. Civan. Temperature dependence of wettability related rock properties correlated by the arrhenius equation. *Petrophysics*, 45(4):350–362, 2004.

[30] J. Rault. The modified vft law of glass former materials under pressure: Part ii: Relation with the equation of state. *The European Physical Journal E*, 38(8):91, 2015.

[31] E. V. Russell and N. E. Israeloff. Direct observation of molecular cooperativity near the glass transition. *Nature*, 408(6813):695–698, 2000.

[32] V. N. Novikov, E. Rssler, V. K. Malinovsky, and N. V. Surovtsev. Strong and fragile liquids in percolation approach to the glass transition. *Europhysics Letters*, 35(4):289, 1996.

[33] H. Fujimori and M. Oguni. Correlation index and activation energy ratio as parameters characterizing the structure of liquid and glass. *Solid State Communications*, 94(2):157 – 162, 1995.

[34] H. Bässler. Viscous flow in supercooled liquids analyzed in terms of transport theory for random media with energetic disorder. *Physics Review Letter*, 58:767–770, 1987.

[35] Y. S. Elmatad, D. Chandler, and J. P. Garrahan. Corresponding states of structural glass formers. *The Journal of Physical Chemistry B*, 113(16):5563–5567, 2009.

[36] L. C. E. Struik. *Physical aging in amorphous polymers and other materials*. Elsevier Scientific Pub. Co. Distributors for the U.S. and Canada, Elsevier North-Holland, Amsterdam New York New York, 1978.

[37] D. R. Cassar, R. F. Lancelotti, R. Nuernberg, M. L. F. Nascimento, A. M. Rodrigues, L. T. Diz, and E. D. Zanotto. Elemental and cooperative diffusion in a liquid, supercooled liquid and glass resolved. *The Journal of Chemical Physics*, 147(1):014501, 2017.

[38] J. H. Gibbs and E. A. DiMarzio. Nature of the glass transition and the glassy state. *The Journal of Chemical Physics*, 28(3):373–383, 1958.

[39] R. Brüning and K. Samwer. Glass transition on long time scales. *Physics Review B*, 46:11318–11322, 1992.

[40] Hansen. *Theory of simple liquids : with applications to soft matter*. Academic Press, Cambridge, UK New York, 2013.

[41] K. Grzybowska. Role of entropy in the thermodynamic evolution of the time scale of molecular dynamics near the glass transition. *Physical Review E*, 91(6):062305, 2015.

[42] B. Wowk. Thermodynamic aspects of vitrification. *Cryobiology*, 60(1):11 – 22, 2010.

[43] V. Lubchenko and P. G. Wolynes. Theory of structural glasses and supercooled liquids. *Annual Review of Physical Chemistry*, 58(1):235–266, 2007.

[44] E. Masiewicz, A. Grzybowski, K. Grzybowska, S. Pawlus, J. Pionteck, and M. Paluch. Adam-gibbs model in the density scaling regime and its implications for the configurational entropy scaling. *Scientific Reports*, 5:13998, 2015.

[45] G. Adam and J. H. Gibbs. On the temperature dependence of cooperative relaxation properties in glassforming liquids. *The Journal of Chemical Physics*, 43(1):139–146, 1965.

[46] K. Chen and K. S. Schweizer. Theory of relaxation and elasticity in polymer glasses. *The Journal of Chemical Physics*, 126(1):014904, 2007.

[47] D. Wales. *Energy landscapes*. Cambridge University Press, Cambridge, UK New York, 2003.

[48] P. G. Debenedetti, T. M. Truskett, C. P. Lewis, and F. H. Stillinger. Theory of supercooled liquids and glasses: Energy landscape and statistical geometry perspectives. *Advances in Chemical Engineering*, 28:21 – 79, 2001.

[49] F. H. Stillinger. Hidden structure in liquids. *Physical Review A*, 25(2):978–989, 1982.

[50] F. H. Stillinger. A topographic view of supercooled liquids and glass formation. *Science*, 267(5206):1935 – 1939, 1995.

[51] A discussion on theory of liquids - supercooling of liquids. *Proceedings of the Royal Society of London A: Mathematical, Physical and Engineering Sciences*, 215(1120):43–46, 1952.

[52] Z. Evenson, I. Gallino, and R. Busch. The effect of cooling rates on the apparent fragility of zr-based bulk metallic glasses. *Journal of Applied Physics*, 107(12):123529, 2010.

[53] B. Frick, D. Richter, and C. Ritter. Structural changes near the glass transitionäìneutron diffraction on a simple polymer. *Europhysics Letters*, 9(6):557, 1989.

[54] M. D. Ediger. Spatially heterogeneous dynamics in supercooled liquids. *Annual Review of Physical Chemistry*, 51(1):99–128, 2000.

[55] A. Widmer-Cooper and P. Harrowell. On the relationship between structure and dynamics in a supercooled liquid. *Journal of Physics: Condensed Matter*, 17(49):S4025, 2005.

[56] A. Widmer-Cooper and P. Harrowell. Free volume cannot explain the spatial heterogeneity of debye–waller factors in a glass-forming binary alloy. *Journal of Non-Crystalline Solids*, 352(42):5098 – 5102, 2006.

[57] C. P. Royall, S. R. Williams, T. Ohtsuka, and H. Tanaka. Direct observation of a local structural mechanism for dynamic arrest. *Nature Materials*, 7(7):556–561, 2008.

[58] T. Egami and D. Srolovitz. Local structural fluctuations in amorphous and liquid metals: a simple theory of the glass transition. *Journal of Physics F: Metal Physics*, 12(10):2141, 1982.

[59] W. Qi and R. K. Bowles. Vapor condensed and supercooled glassy nanoclusters. *ACS Nano*, 10(3):3416–3423, 2016.

[60] H. Yu, Y. Luo, and K. Samwer. Ultrastable metallic glass. *Advanced Materials*, 25(41):5904–5908, 2013.

[61] I. Vincze, D. S. Boudreaux, and M. Tegze. Short-range order in fe-b metallic glass alloys. *Physics Review. B*, 19:4896–4900, 1979.

[62] G. Dlubek. Fluctuation approach for the estimation of the dynamic heterogeneity in glass-forming liquids from the dispersion in o-ps lifetimes: Free volume fluctuations in polymers. *Journal of Non-Crystalline Solids*, 352(26):2869 – 2879, 2006.

[63] B. Rijal, L. Delbreilh, and A. Saiter. Dynamic heterogeneity and cooperative length scale at dynamic glass transition in glass forming liquids. *Macromolecules*, 48(22):8219–8231, 2015.

[64] G. Dlubek, A. Sen Gupta, J. Pionteck, R. Krause-Rehberg, H. Kaspar, and K. H. Lochhaas. Temperature dependence of the free volume in fluoroelastomers from positron lifetime and pvt experiments. *Macromolecules*, 37(17):6606–6618, 2004.

[65] J. Wuttke, W. Petry, and S. Pouget. Structural relaxation in viscous glycerol: Coherent neutron scattering. *The Journal of Chemical Physics*, 105(12):5177–5182, 1996.

[66] L. C. Pardo, P. Lunkenheimer, and A. Loidl. Dielectric spectroscopy in benzophenone: The β relaxation and its relation to the mode-coupling cole-cole peak. *Physics Review E*, 76:030502, 2007.

[67] J. Horbach and W. Kob. Relaxation dynamics of a viscous silica melt: The intermediate scattering functions. *Physics Review E*, 64:041503, 2001.

[68] H. C. Andersen. Molecular dynamics studies of heterogeneous dynamics and dynamic crossover in supercooled atomic liquids. *Proceedings of the National Academy of Sciences*, 102(19):6686–6691, 2005.

[69] C. J. Ellison, M. K. Mundra, and J. M. Torkelson. Impacts of polystyrene molecular weight and modification to the repeat unit structure on the glass transitionnanoconfinement effect and the cooperativity length scale. *Macromolecules*, 38(5):1767–1778, 2005.

[70] D. Chandler and J. P. Garrahan. Dynamics on the way to forming glass: Bubbles in space-time. *Annual Review of Physical Chemistry*, 61(1):191–217, 2010.

[71] M. Sellitto, D. De Martino, F. Caccioli, and J. J. Arenzon. Dynamic facilitation picture of a higher-order glass singularity. *Physics Review Letter*, 105:265704, 2010.

[72] C. Hermann. *Statistical physics : including applications to condensed matter*. Springer, New York, N.Y, 2005.

[73] D. Frenkel and B. Smit. *Understanding molecular simulation : from algorithms to applications*. Academic Press, San Diego, 2002.

[74] D. Ornstein. *Ergodic theory, randomness, and dynamical systems*. Yale University Press, New Haven, 1974.

[75] D. C Rapaport. *The art of molecular dynamics simulation*. Cambridge University Press, Cambridge, UK New York, NY, 2004.

[76] D.J. Adams. Chemical potential of hard-sphere fluids by monte carlo methods. *Molecular Physics*, 28(5):1241–1252, 1974.

[77] Z. Zhang, P. Fenter, L. Cheng, N. C. Sturchio, M. J. Bedzyk, M. Předota, A. Bandura, J. D. Kubicki, S. N. Lvov, P. T. Cummings, A. A. Chialvo, M. K. Ridley, P. Bénézeth, L. Anovitz, D. A. Palmer, M. L. Machesky, and D. J. Wesolowski. Ion adsorption at the rutilewater interface: linking molecular and macroscopic properties. *Langmuir*, 20(12):4954–4969, 2004.

[78] J.S. Rowlinson. A test of the lennard-jones potential for nitrogen and methane. *Molecular Physics*, 3(3):265–269, 1960.

[79] N. B. Slater. Classical motion under a morse potential. *Nature*, 180(4598):1352–1353, 1957.

[80] A.P. Lima, A.S. Martins, and J.S. Martins. Lennard-jones binary fluids: A comparative study between the molecular dynamics and monte carlo descriptions of their structural properties. *Physica A: Statistical Mechanics and its Applications*, 391(18):4281 – 4289, 2012.

[81] R. Hockney. *Computer simulation using particles*. A. Hilger, Bristol England Philadelphia, 1988.

[82] M. P. Allen. *Computer simulation of liquids*. Clarendon Press Oxford University Press, Oxford England New York, 1989.

[83] R. Murty and D. Okunbor. Efficient parallel algorithms for molecular dynamics simulations. *Parallel Computing*, 25(3):217 – 230, 1999.

[84] D. Chandler. *Introduction to modern statistical mechanics*. Oxford University Press, New York, 1987.

[85] J. L. Yarnell. Structure factor and radial distribution function for liquid argon at 85 °k. *Physical Review A*, 7(6):2130–2144, 1973.

[86] N. Lmmen and T. Kraska. Common neighbour analysis for binary atomic systems. *Modelling and Simulation in Materials Science and Engineering*, 15(3):319, 2007.

[87] J. D. Honeycutt and H. C. Andersen. Molecular dynamics study of melting and freezing of small lennard-jones clusters. *The Journal of Physical Chemistry*, 91(19):4950–4963, 1987.

[88] A. Stukowski. Structure identification methods for atomistic simulations of crystalline materials. *Modelling and Simulation in Materials Science and Engineering*, 20(4):045021, 2012.

[89] D. R. Nelson and J. Toner. Bond-orientational order, dislocation loops, and melting of solids and smectic-*a* liquid crystals. *Physics Review B*, 24:363–387, 1981.

[90] I. Saika-Voivod, L. Poon, and R. K. Bowles. The role of fcc tetrahedral subunits in the phase behavior of medium sized lennard-jones clusters. *The Journal of Chemical Physics*, 133(7):074503, 2010.

[91] W. Lechner and C. Dellago. Accurate determination of crystal structures based on averaged local bond order parameters. *The Journal of Chemical Physics*, 129(11):114707, 2008.

[92] S. Papanikolaou, J. Schroers, M. D. Shattuck, and C. S. O'Hern. Computational studies of the glass-forming ability of model bulk metallic glasses. *The Journal of Chemical Physics*, 139(12):124503, 2013.

[93] D. R. Nelson. Bond-orientational order, dislocation loops, and melting of solids and smectic- a liquid crystals. *Physical Review B*, 24(1):363–387, 1981.

[94] C. Desgranges and J. Delhommelle. Crystallization mechanisms for supercooled liquid xe at high pressure and temperature: Hybrid monte carlo molecular simulations. *Physics Review B*, 77:054201, 2008.

[95] T. Kawasaki and A. Onuki. Construction of a disorder variable from steinhardt order parameters in binary mixtures at high densities in three dimensions. *The Journal of Chemical Physics*, 135(17):174109, 2011.

[96] J. Park and Y. Shibutani. Effects of atomic size for voronoi tessellation technique on binary and ternary systems of metallic glasses. *Materials Transactions*, 47(12):2904–2909, 2006.

[97] O. Gedeon and M. Liška. Voronoi polyhedra analysis of md simulated silicate glasses. *Journal of Non-Crystalline Solids*, 303(2):246 – 252, 2002.

[98] T. Fukunaga, K. Itoh, T. Otomo, K. Mori, M. Sugiyama, H. Kato, M. Hasegawa, A. Hirata, Y. Hirotsu, and A. C. Hannon. Voronoi analysis of the structure of ni-zr-al ternary metallic glass. *Materials Transactions*, 48(7):1698–1702, 2007.

[99] T. Fukunaga, K. Itoh, T. Otomo, K. Mori, M. Sugiyama, H. Kato, M. Hasegawa, A. Hirata, Y. Hirotsu, and A.C. Hannon. Voronoi analysis of the structure of cu–zr and ni–zr metallic glasses. *Intermetallics*, 14(8):893 – 897, 2006. Fourth International Conference on Bulk Metallic Glasses.

[100] K. H. Kuo. Mackay, anti-mackay, double-mackay, pseudo-mackay, and related icosahedral shell clusters. *Structural Chemistry*, 13(3):221–230, 2002.

[101] C. H. Rycroft. *Multiscale Modeling in Granular Flow*. PhD thesis, Massachusetts Institute Of Technology, 2007.

[102] L. C. Valdes, F. Affouard, M. Descamps, and J. Habasaki. Mixing effects in glass-forming lennard-jones mixtures. *The Journal of Chemical Physics*, 130(15):154505, 2009.

Appendix A

Figures

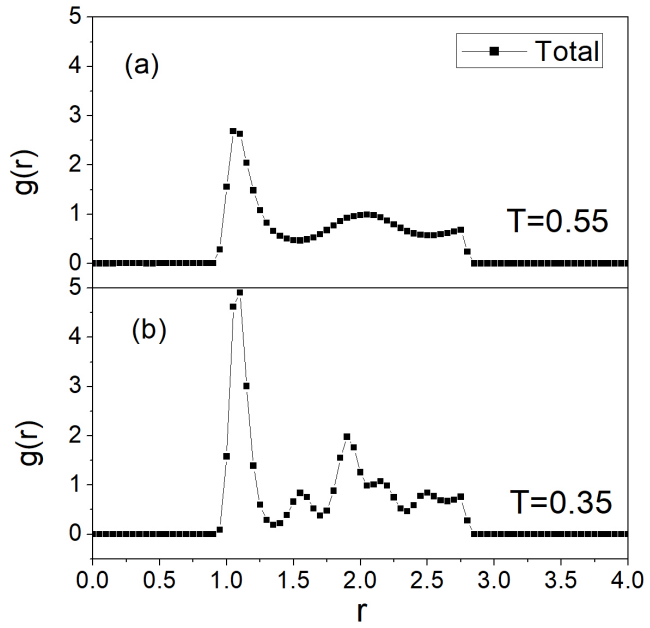

Figure A.1: Radial Distribution for pure A nanocluster. Figure(a) shows the $g(r)$ of liquid state at high temperature. Figure(b) shows the $g(r)$ of crystal state at low temperature.

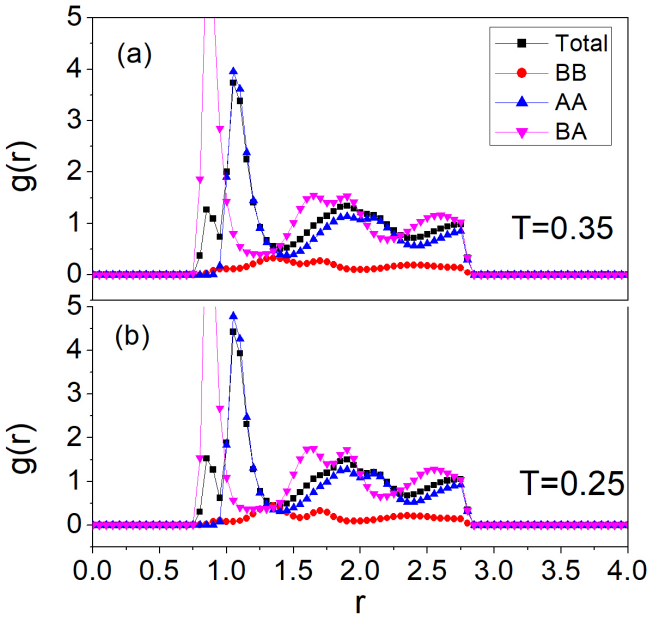

Figure A.2: Radial Distribution for $x_B = 0.1$ nanocluster. Figure(a) shows the $g(r)$ of liquid state at high temperature. Figure(b) shows the $g(r)$ of glassy state at low temperature.

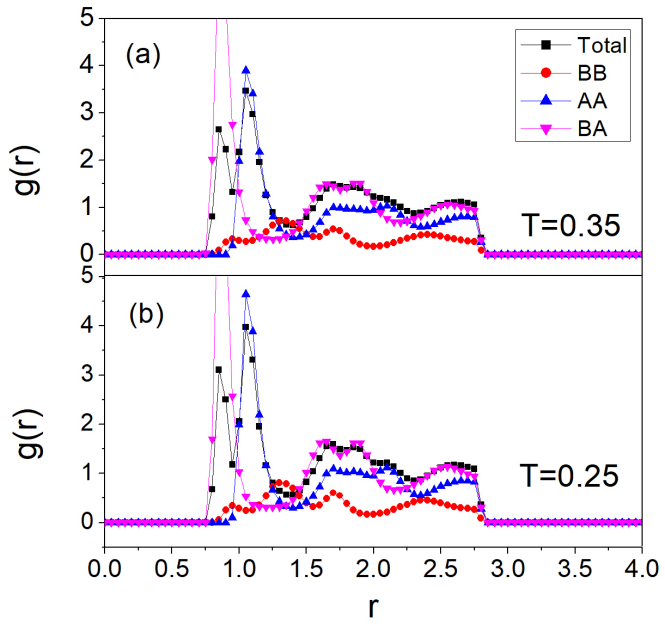

Figure A.3: Radial Distribution for $x_B = 0.2$ nanocluster. Figure(a) shows the $g(r)$ of liquid state at high temperature. Figure(b) shows the $g(r)$ of glassy state at low temperature.

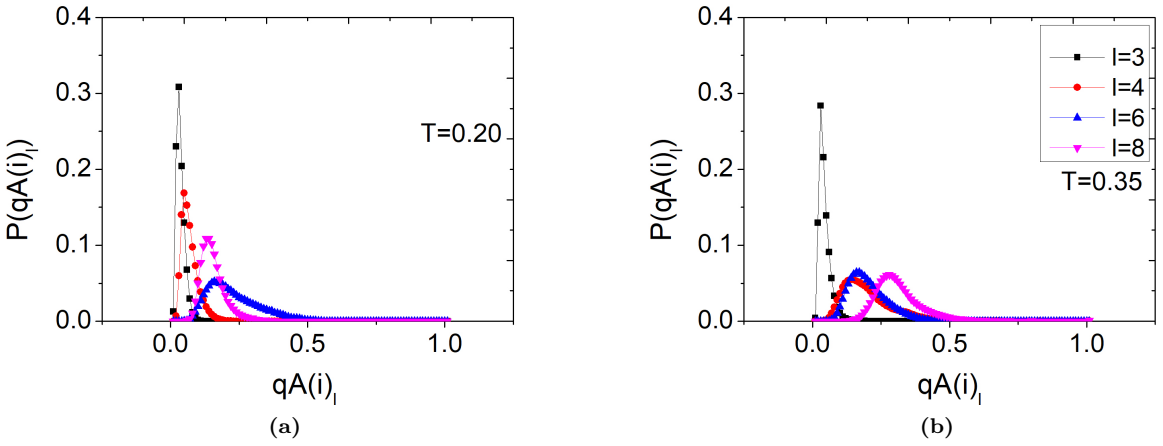

Figure A.4: Distribution of average local order parameters with different symmetry index l, for $x_B = 0.1$ nanocluster at high and low temperature.

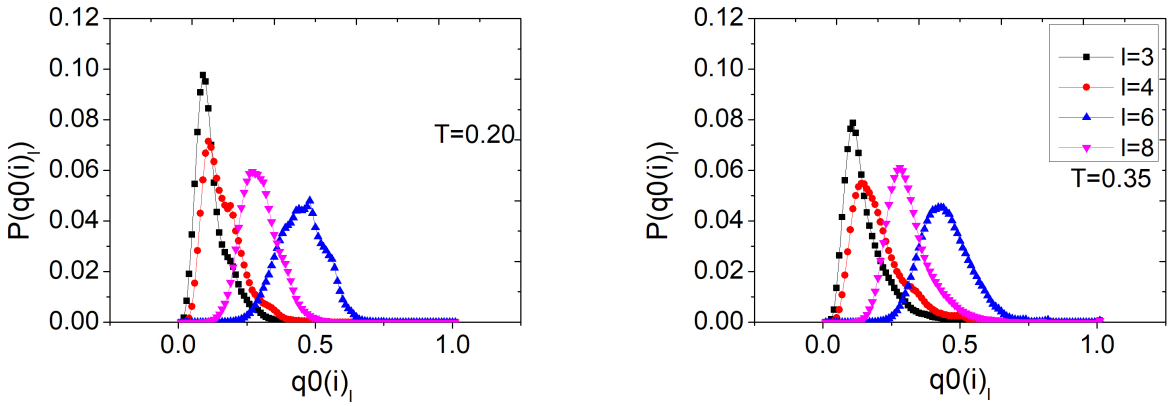

(a) (b)

Figure A.5: Distribution of local order parameters with different symmetry index l, for $x_B = 0.1$ nanocluster at high and low temperature.

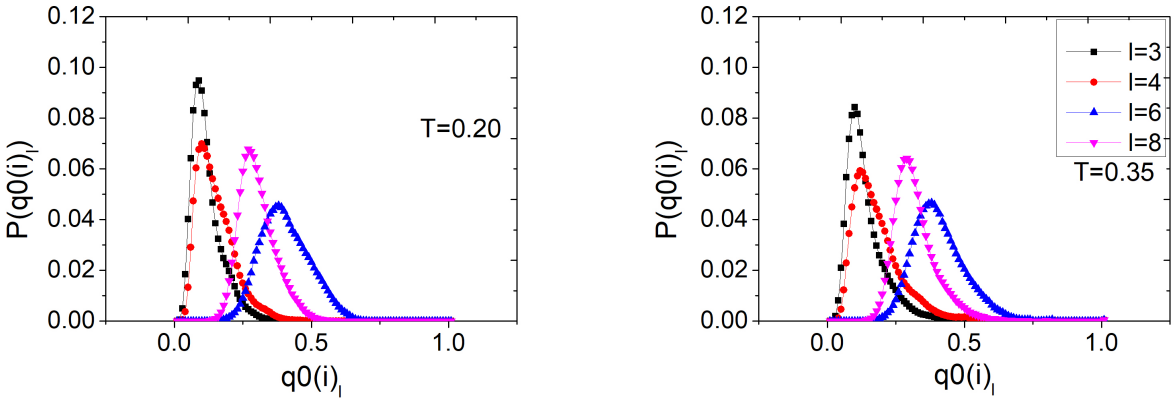

(a) (b)

Figure A.6: Distribution of local order parameters with different symmetry index l, for $x_B = 0.2$ nanocluster at high and low temperature.

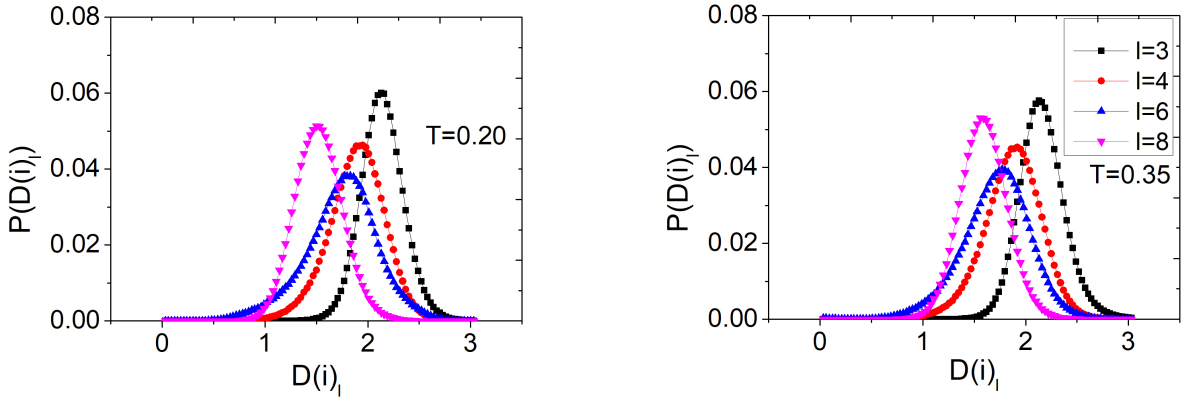

Figure A.7: Distribution of disorder parameters with different symmetry index l, for $x_B = 0.2$ nanocluster at high and low temperature.

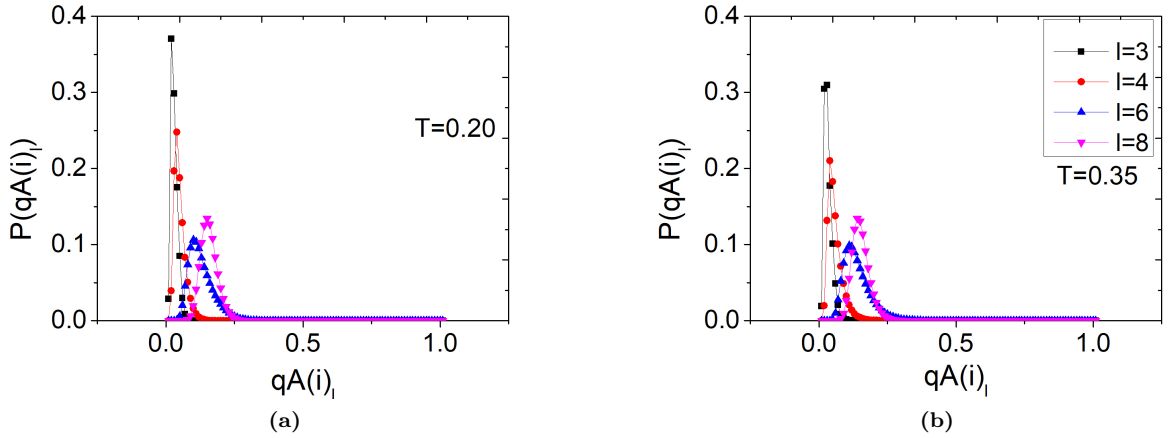

Figure A.8: Distribution of average local order parameters with different symmetry index l, for $x_B = 0.3$ nanocluster at high and low temperature.

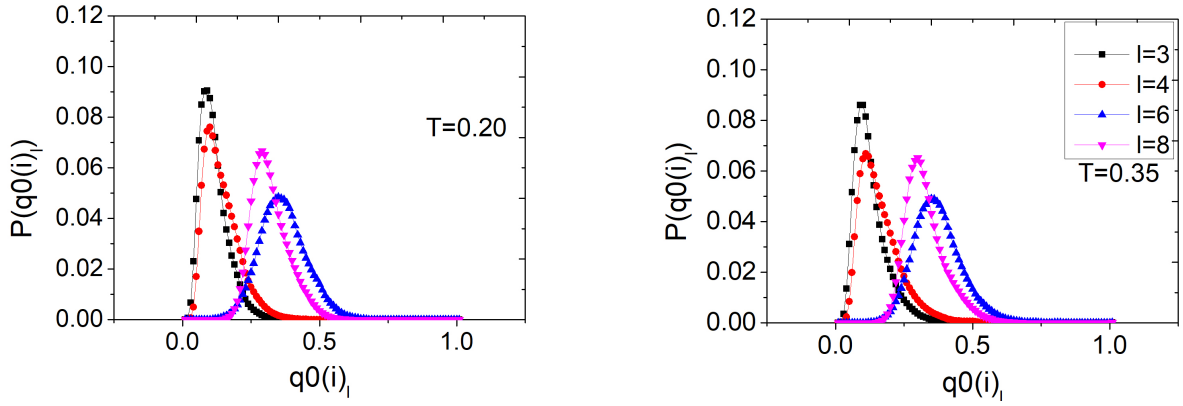

(a) (b)

Figure A.9: Distribution of local order parameters with different symmetry index l, for $x_B = 0.3$ nanocluster at high and low temperature.

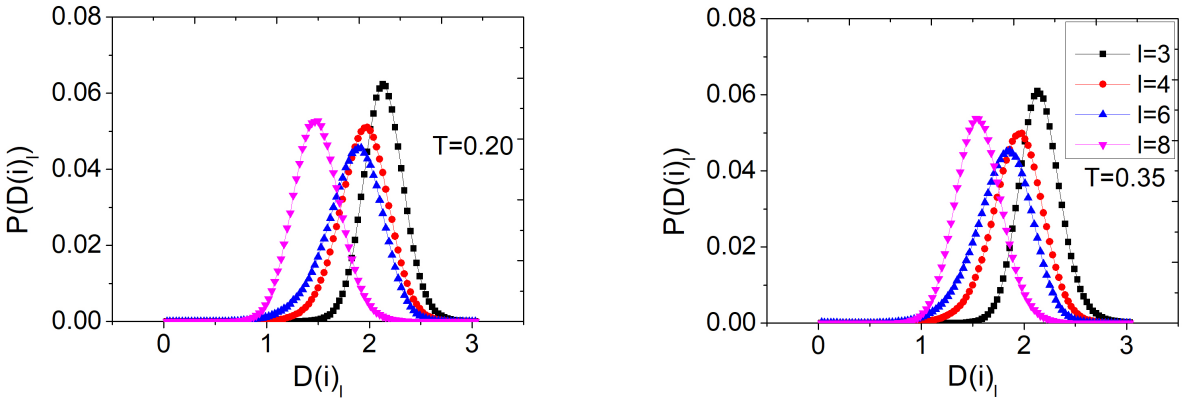

(a) (b)

Figure A.10: Distribution of disorder parameters with different symmetry index l, for $x_B = 0.3$ nanocluster at high and low temperature.

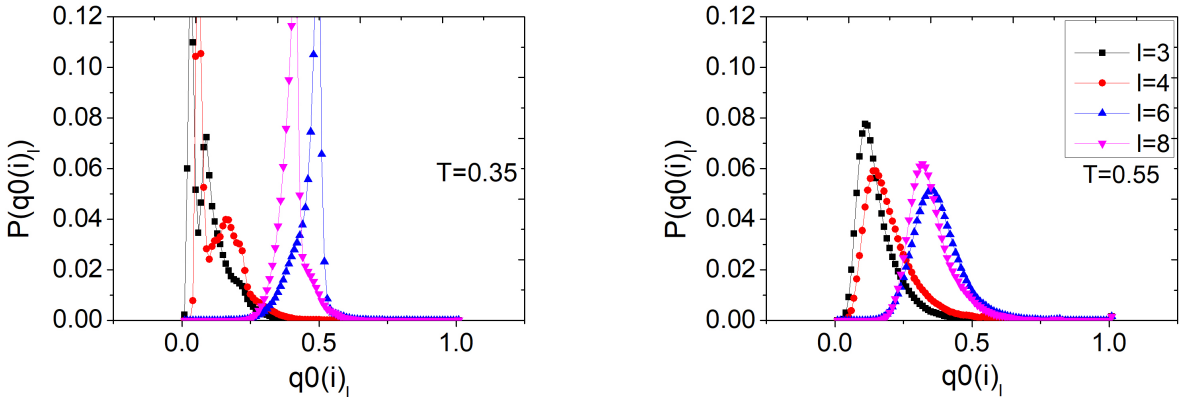

Figure A.11: Distribution of local order parameters with different symmetry index l, for $x_B = 0.4$ nanocluster at high and low temperature.

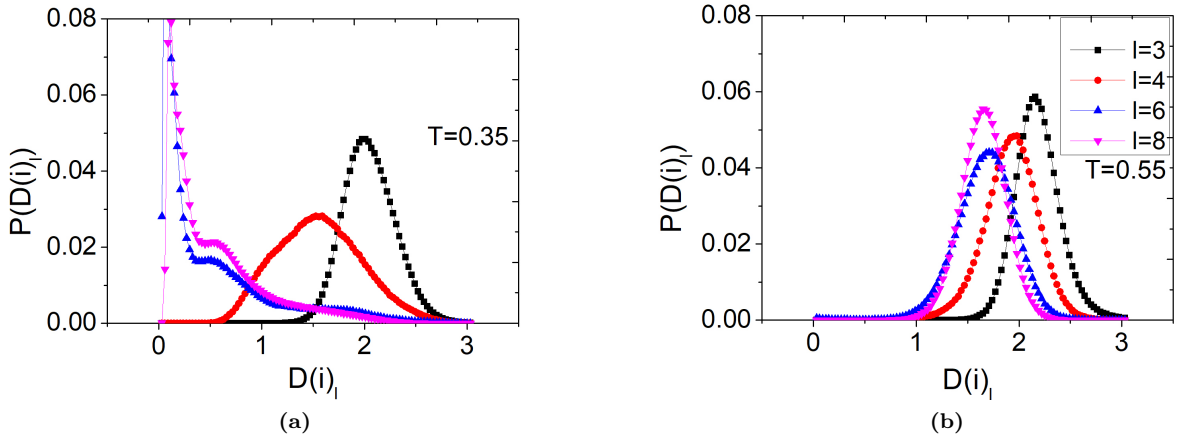

Figure A.12: Distribution of average disorder parameters with different symmetry index l, for $x_B = 0.4$ nanocluster at high and low temperature.

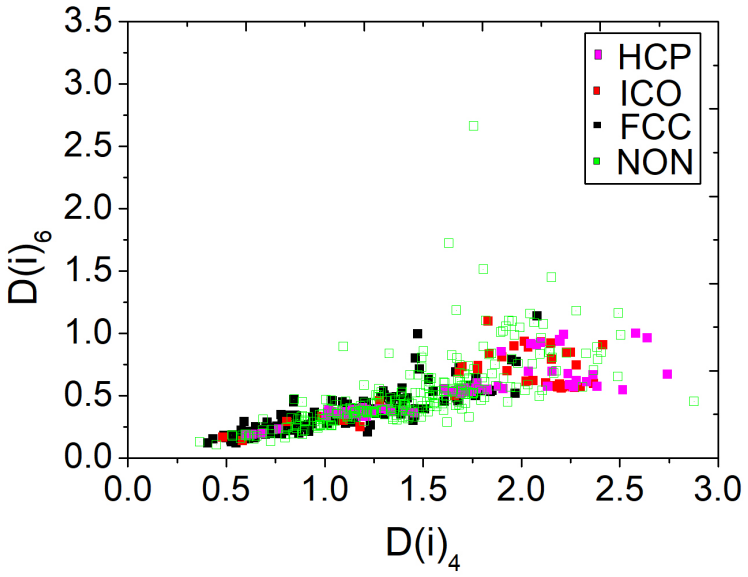

Figure A.13: $D(i)_4$-$D(i)_6$ distribution for 10 pure A nanoclusters at $T = 0.20$.

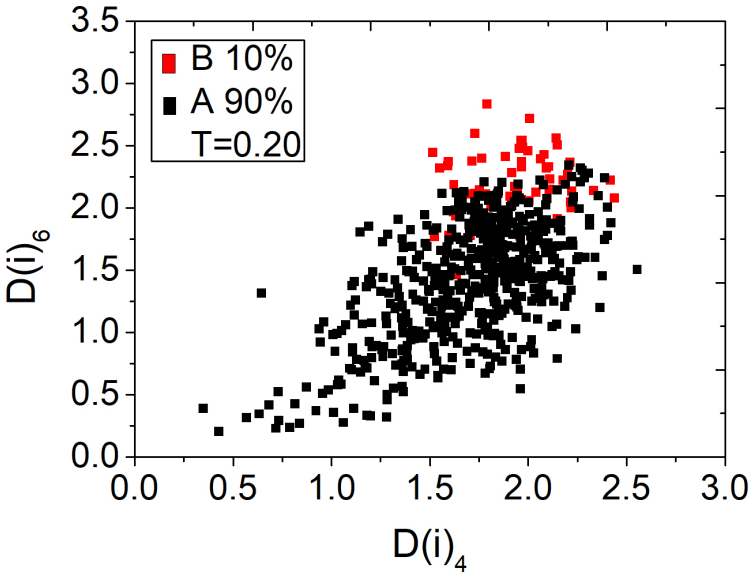

Figure A.14: $D(i)_4$-$D(i)_6$ distribution for $x_B = 0.1$ nanocluster at $T = 0.20$.

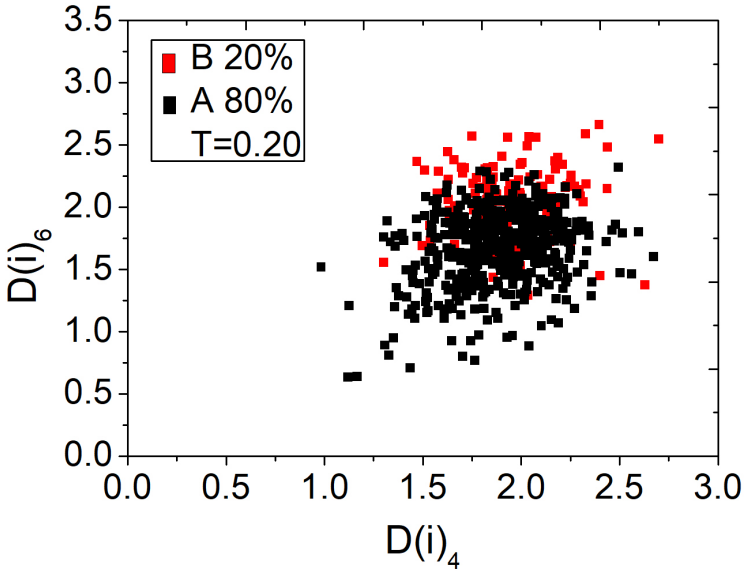

Figure A.15: $D(i)_4$-$D(i)_6$ distribution for $x_B = 0.2$ nanocluster at $T = 0.20$.

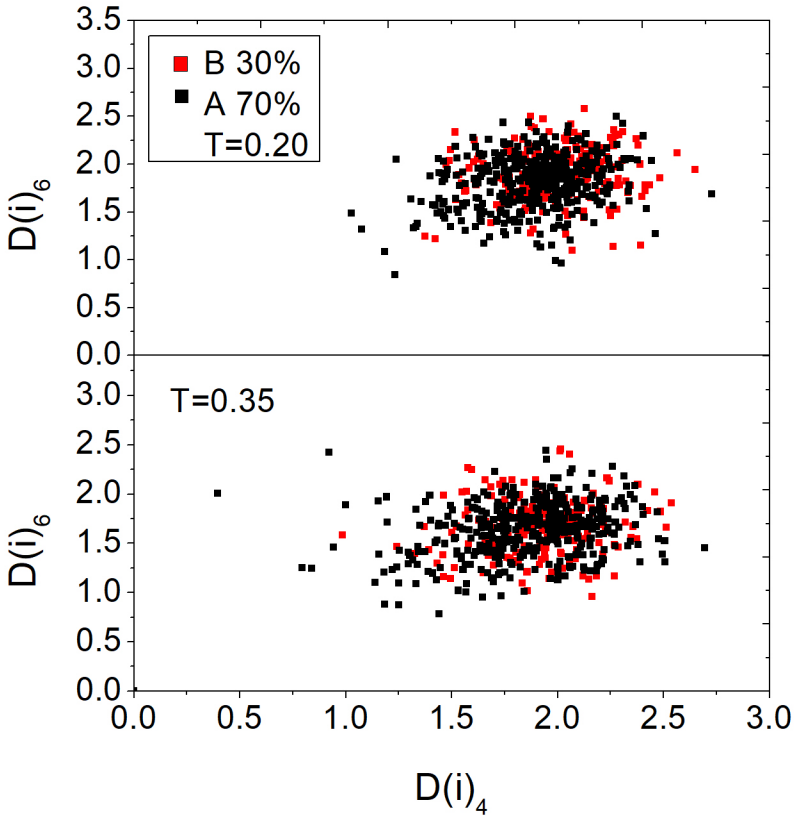

Figure A.16: $D(i)_4$-$D(i)_6$ distribution for $x_B = 0.3$ nanocluster at $T = 0.20$.